STRATEGIC INITIATIVE
Undergraduate Research Funding for STEM Majors at the University of Idaho

FINAL PROJECT REPORT

Submitted to:

Higher Education Research Council
Idaho State Board of Education
P.O. Box 83720
Boise, Idaho 83720-0037

Submitted by:

University of Idaho
Office of Undergraduate Research

875 Perimeter Drive
Moscow, ID 83844

August 31, 2018

Table of Contents

Executive Summary

Undergraduate research is recognized as a high-impact educational practice that increases the rates of student retention and engagement. At the University of Idaho, it is practiced throughout all units on campus and it is centrally placed in the institution's strategic plan. The Office of Undergraduate Research is taking the lead in enabling research opportunities for undergraduates at UI. It manages various competitive student grant programs that directly support student research.

During AY 2017-18, generous funding from the State Board of Education permitted UI to continue its Summer Undergraduate Research Fellowship (SURF) Program. This intensive multi-week summer research experience actively engages undergraduates in faculty- mentored, independent research. Over the course of 10 weeks, students are mentored toward increased independence on their projects. Each student is provided with a $4,000 stipend in the form of a fellowship which allows them to devote full time effort to their projects. Each student is also provided with $1,000 to help offset materials and supplies and other project-related expenses. Selection of student participants is a competitive process in which students submit research proposals to the Office of Undergraduate Research. State Board of Education funding supported 10 SURF awards during the summer of 2018.

Funding provided by the State Board of Education also allowed the Office of Undergraduate Research to support a number of undergraduate researchers during the academic year. This was accomplished through competitive Undergraduate Research Grants awarded to students during the spring semester of 2018. These grants supported semester-long research projects under the guidance of faculty mentors. These grants were in the amount of $1,000 each for materials and supplies and other project-related expenses. State Board of Education funding supported 5 Undergraduate Research Grants during the spring semester of 2018.

Almost all of UI students supported by State Board of Education funds attended and presented the results of their projects at the Idaho Conference on Undergraduate Research held in Boise in July of 2018. A few students were unable to attend the ICUR conference. In lieu of this, these students will instead be required to present their results at the UI Undergraduate Research Symposium in April 2019.

End of project feedback from students and their mentors was overwhelmingly positive. Significantly, none of the undergraduate research projects described here would have been possible without the support provided by the State Board of Education. We sincerely thank the Higher Education Research Council and the Idaho State Board of Education for making these experiences possible for our students.

Final Project Report: Office of Undergraduate Research (OUR) Undergraduate Research Grant – Spring 2018

Fellowship Recipient: Mason Anderson, Chemical Engineering, University of Idaho

Faculty Mentor: Dr. Mark Roll, Associate Professor, Dept. of Chemical & Materials Engineering

Project Title: Mechanistic Analysis of Borohydride Thermolysis

Abstract: Boron cluster chemistry has seen large strides in progress during the 20th century, but little has been investigated since for these robust hybrid compounds outside of a select number of research groups. Borohydride clusters are essential stepping stones in the path toward many phenomenal applications to areas such as nano-building blocks, super-ionic electrochemistry, and refractory precursors. However, the classical syntheses of these borohydride clusters are obscured by highly reactive and toxic neutral borane compounds and shrouded mechanisms. This project aims to analyze the mechanistic nature of these classical syntheses to employ less toxic precursory materials and afford "greener" side products.

Project Accomplishments:

1. Analyze theoretical oxidation-reduction mechanism of polarizable reactants: The initiation of cluster formation via reduction by borohydride has been proposed while some other work has shown the possibility of a radical based mechanism, determining which is correct (or both) was attempted here

Result: When the classical synthesis was modified slightly and run reacting iodine with $NaBH_4$ in diglyme, interesting results appeared. With the use of a stainless-steel needle for addition instead of a constant addition funnel (for more precise addition rates) the tip of the needle was destroyed and the broken down by the reaction slurry. This indicates a very reactive intermediate product possibly hydrogen iodide (HI), supporting our prediction.

2. Conduct continuous ^{11}B NMR to monitor transitional states: The use of time-dependent NMR allowed for minute by minute analysis of classical syntheses to help decode the inner workings of the reactions

Result: The time-dependent NMR confirmed the need for a $B_2H_7^-$ intermediate product, but the $B_3H_8^-$ was not observed in reactions at room temperature indicating the possibility of an activation energy barrier to the formation of $B_3H_8^-$.

3. Observe different borohydride product yields after varying reaction reactants: Alkyl halides and metal halides were also tested during this project for their viability as reactants with $NaBH_4$.

Result: The use of metal halides formed the target anionic cluster, but the solid metal was left after reduction by $NaBH_4$ leading to a difficult workup and extraction of the anionic clusters. The use of alkyl halides proved difficult in their higher concentration as neat liquids and their inherent ability to photoionized when exposed to sunlight, but with the dilution using the appropriate solvent and careful lighting measures lead to similar cluster formation under similar conditions.

4. Test different reaction solvents: Modifying the classical reaction solvent(s) allows for better analysis of the role played by the solvent in the reaction system

Result: The most interesting change to the system occurred using THP (tetrahydropyran), a cyclic ether only one carbon longer than a classical solvent THF (tetrahydrofuran). When THP was used the reaction only formed higher neutral borane clusters and little to no anionic borohydride clusters were observed, this could be because the neutral species borane and diborane remained in solution after formation and the borohydride (BH_4^-) was not in solution due to the low solubility of $NaBH_4$ in THP. This result could have potential benefits for in-situ generation of neutral borane clusters to avoid direct handling of the toxic neutral clusters

Summary of Budget Expenditures

Material	Price
Lithium Borohydride, 25g, 90%	$285.50
PTFE Needle, 2.11mm OD, 12" L (2)	$26.96 each
PTFE Needle, 1.57mm OD, 12" L (2)	$23.58 each
BROMINE LIQUID ACS 99.5% 100G	$46.08
Lithium Borohydride Solution in THF, 100mL, 2.0M	$107.50
5 mm Medium Wall Precision NMR Sample Tube 9" L, 400MHz (5)	$17.06 each
Adamantyl Amine, 25g, 97%	$153.00
Potassium Borohydride, 25g, 97%	$40.08
Iodomethane, 50mL, 95%	$57.25
Poster Printing	$75
Subtotal Supplies	$996.37
TOTAL	$996.37

Acknowledgment: This work was made possible by generous support from the Idaho State Board of Education which provided the funding for this Undergraduate Research Grant from the Office of Undergraduate Research. The experience this opportunity provided me was tremendous. I sincerely thank the SBOE and UI's Office of Undergraduate Research.

Final Project Report: Office of Undergraduate Research (OUR) Undergraduate Research Grant – Spring 2018

Recipient: Neale Ellyson

Faculty Mentor: Dr. David Drown, Department of Chemical and Materials Engineering

Project Title: Determining Electrical Conductivity of Battery Plate Materials

Abstract

The electrical conductivity of battery plate materials with GUITAR coated ceramic fiber additives and the cycled plates themselves was measured. University of Idaho patent-pending research on GUITAR has been shown to improve lead-acid battery performance. The measured data of varying coating process and materials were able to be compared against each other.
Additionally, the plates from finished cells were measured to provide further results.

Introduction

As a result of years of battery research done by the University of Idaho's Dr. Cheng and Edwards, further exploration of the nature GUITAR coated additives has been required. In response to that, a 4-point conductivity apparatus designed by Roper[###] yielded data on the electrical conductivity of a material providing an additional metric to weigh in considering a battery cell's performance. Using this apparatus, a methodology for determining the conductive property of battery plate materials can be formed for future research.

This 4-point conductivity apparatus, seen in Figure 1, consists of two copper rods, PVC pipe mounted on a base plate. The bottom copper rod is able to be removed from the base for easier clean up, then the PVC pipe is placed on top of the bottom rod, making a seal of the space inside with the O-rings on the bottom copper rod. The top copper rod is able to fit inside that PVC tube. The brass screws protruding from the top and bottom of the apparatus allow for a variety of clips to be applied for the measuring portion of the procedure.

The project was performed alongside the Lead Acid Battery Research And Testing, or LABRAT, senior design project, whose objective was to test the performance of batteries with 15, 20, 25% by volume additive in both the positive and active materials as well as a control, designated 0% by volume additive.

Method

In establishing a set procedure to measure battery plate materials, the battery plate paste was the main objective to measure. Battery plate paste consists of lead oxide, deionized water, sulfuric acid at 1.4 specific gravity, and in the case of the majority of the research a carbon-coated additive. In the scope of this project, the only additive used was GUITAR coated ceramic fibers produced in the tube furnace. The original intent was to have molds for the paste to be cured and dried in, similar to the fabrication of a battery plate on a lead grid. This required the resulting chip to be completely smooth and flat so the copper rods could make complete contact with the material. Initial trials proved that the curing process adhered the paste to the mold too much to retrieve an intact chip. The next course of action was to crush these chips into a fine powder and

measure the powder. The various preparations done for the variety of materials measured is detailed in Appendix A.1. The measurement procedure is as follows:

1) Portion out a consistent mass of the material being measured, approximately 2-3 grams is satisfactory.
2) Insert into the PVC tube placed on top of the bottom copper rod.
3) Place top copper rod inside and compress material with a weight, approximately 32 lbs.
4) Calculate the volume of the material using the known cross-sectional area of the PVC and using the reference pin to measure the length with a digital caliper.
5) Either:
   a. Using an Arbin Battery Tester, apply a uniform current for approximately ten seconds and record measured voltage
   b. Using a digital multimeter, record resistance.
6) Calculate sample conductivity per unit length

This procedure was adapted for the use of other battery plate materials, as well. For example, when measuring the GUITAR coated ceramic fibers, Step 3 required a heavier weight, yielding a more accurate measurement, due to the fibers needing more compression. Step 4 requires the knowledge of the inner diameter of the PVC tube to yield a cross-sectional area of $3.46 \cdot 10^{-4}\ m^2$. Additionally, Step 6 requires elaboration. In order to calculate conductivity, σ (S/m), resistance, R (Ω), must first be calculated using Equation 1:

$$R = \frac{\Delta V}{I} \qquad \textbf{Equation 1}$$

Where ΔV is the difference in voltage, mV, and I is the current in mA. Using this calculation, conductivity can be found using Equation 2:

$$\sigma = \frac{L \cdot R \cdot A}{1000} \qquad \textbf{Equation 2}$$

Where L is the measured length, m, from the reference pin, yielding the volume of the substance inside the PVC.

Results

In conjunction with the LABRAT design team, the conductivities of the ceramic fibers were continuously measured prior to the pasting process. These results can be seen in Figure 2.

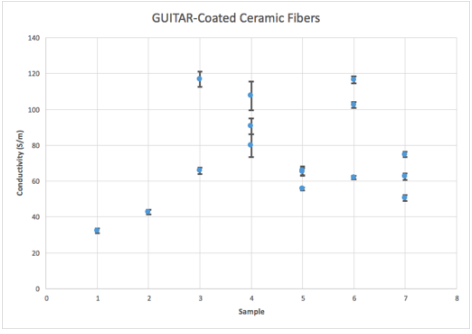

***Figure 2**: Conductivity measurements of GUITAR coated ceramic fiber*

It is noticeable that there are multiple measurements for a given sample. As the amount of volume required per battery plate pasting batch increased throughout the semester, multiple batches were produced for a single pasting session. In adapting the procedure to these variations, the batches would first be measured individually and then combined and measured once more. Once combined the fibers would be integrated at varying volume percentages to the battery paste where samples 1-4 were used in 15, 20, 25 and 25% again in the positive material battery paste and samples 5-7 were used in the 15, 20, 25% negative active material battery paste. These results were used alongside the battery cell's performance to compare which cells performed best at a given conductivity.

Finally, the conductivities of the powdered paste samples were also measured, seen in Figure 3.

***Figure 3**: Conductivity measurements of powdered battery paste materials*

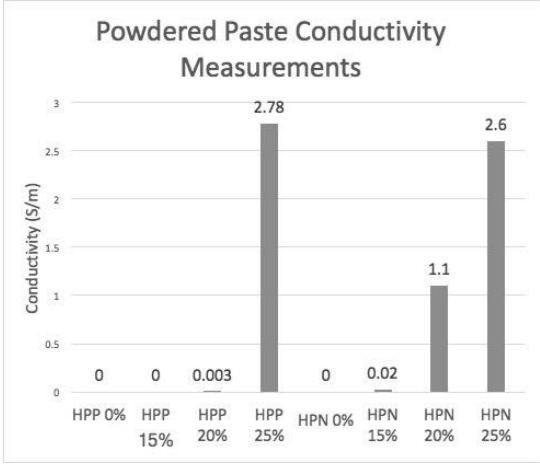

Here, data reflects the understanding that adding more conductive materials to a nonconductive material yields an increase in overall conductivity. To be clear, the notation HPP stands for hand-pasted positive, and HPN, for hand-pasted negative. The 0, 15, 20, and 25 percentages represent the amount of volume added of a specific additive, in this case the GUITAR coated ceramic fibers.
Additionally, preliminary data was recorded from battery plates that had been formed and completed their cycling routine. This data can be seen in Figure 4.

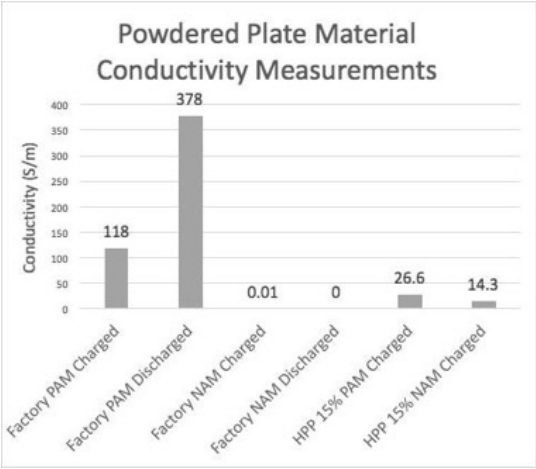

***Figure 4**: Conductivity measurements of powdered, formed battery plate materials*

To clarify notation, 'Factory PAM Charged' refers to the positive active material (PAM) plate, fabricated by the Concorde Battery Corporation, retrieved from a charged battery cell. Therefore, the 'Factory NAM Discharged' similarly refers to the negative active material (NAM) plate, also fabricated by the Concorde Battery Corporation, retrieved from a discharged battery cell. Additionally, the HPP 15% PAM/NAM Charged refer to the material retrieved from a charged positive limiting battery cell. In this case the positive active material is the only sample that contains the additive and the negative active material has no additive inside it though it was noted that it certainly seemed affected by the presence of the additive. Further details of the results are presented in Appendix A.2.

These data are only preliminary as a procedure to retrieve these plates requires additional modifications. Recovering these materials proved difficult due to the degradation of the battery plate at the end of its cycling routine. Many plates had bits of the lead grid being removed with the lead or lead dioxide 'biscuits'. Having those remnants of grid in the material seemed to drastically effect the conductivity results, as seen in the two positive active material samples.

The promising piece of data from these trials were the measurements of the 15% by volume additive in the charged state illustrates that the battery plates are still conductive after the duration of a cycling routine. Continuing these trials could corroborate or refute that the additive continues to contribute to the plate's overall conductivity.

Conclusion

Measuring the conductivities of battery plate materials has proven to be further aid in exploring the properties of a given carbon-coated additive, as well as some insight into the performance of a battery with these additives. Additionally, the battery paste materials showed measurable conductivity increase with the volume percentage increase within a paste.
Preliminary results showed that the battery plates maintain a measure of conductivity after begin formed and processed through a cycling routine.

Recommendations

To continue this research, it is advisable to explore designing a metallic lead conductivity mold to apply the paste with additive to. This scaled-down version of a battery plate then has the potential to be formed and sent through cycling routines. Furthermore, replicate measurements for fully charged and discharged battery plates should be performed and compared to the preliminary data, additionally providing a consistent and effective method of retrieval for these materials.

Appendix

A.1: Detailed preparation procedure for battery plate materials

Battery plate 'chips':

1. Starting with a standard battery plate paste composed of lead oxide, deionized water, sulfuric acid, and ligand expander in the negative paste, take approximately 10g worth of paste and apply to the PVC pipe molds of varying thicknesses using a plastic putty knife.
2. Pack the paste into the mold and flip over, ensuring to flatten both sides as much as

possible.

3. Once packed and flattened, continue the battery plate fabrication process and cure the paste inside an industrial pressure cooker, using wooden popsicle sticks as dividers between the pasted materials to ensure access for the water to properly cure them.
4. After curing for 24 hours, move the materials to an oven to be dried for as long as necessary. Due to the varying thicknesses of the chips some may require longer time in the oven. When first placed in the oven, the materials look clearly saturated with water as the paste still seems wet, but as it dries the saturation is lost and the materials begin to look lighter. When this is seen throughout the plate, it is ready to be removed from the oven, typically three to four days.
5. Once fully dried the chips are ready to be crushed using a mortar and pestle, making sure to create a fine consistency. At this point the conductivity of the battery plate paste is ready to be measured.

Used battery plate materials:

1. Starting with a cell that's completed its cycling routine, remove the desired battery plates and rinse thoroughly with deionized water to remove any sulfuric acid from it.
2. Once rinsed, transfer the used plates to an oven to dry. Similarly to drying paste, identify a fully dried plate by its entire lightness in color from loss of saturation.
3. Once dried, carefully remove the 'biscuits' of the plate, specifically the portion of lead or lead dioxide that fill the holes of the lead grid. It is important to not mix any remnants of the lead grid in with the sample as that can greatly skew the results of the conductivity measurement.
4. Once the biscuits have been retrieved, they may be placed in a mortar and pestle to be pulverized to a fine consistency and then proceed to measurement.

GUITAR-coated ceramic fibers:

1. Starting with a batch of carbon-coated fibers produced from the tube furnace, typically the fibers arrive in a clumped fashion. This requires the separation of the fibers, achieving approximately portioned sizes of a gram.
2. Once the sample is fully de-clumped it is important to thoroughly mix the sample. Coated fibers produced in the tube furnace yields varying conductivities depending on where the fibers were placed in the tube furnace, therefore mixing yields a more accurate measurement.
3. Once entirely mixed the conductivity of the sample is ready to be measured.

A.2: Detailed results of GUITAR-coated ceramic fibers

Date	Sample	Additive %Vol	Material	Conductivity (S/m)	± (95% Confidence)	Average Resistance (Ω)
1/19/18	1	15%	GUITAR Coated Ceramic Fibers from 1/17 Pasting (+ 15%)	32.28752	1.43528	1.09719
1/24/18	2	20%	GUITAR Coated Ceramic Fibers from 1/24 Pasting (+ 20%)	42.72056	1.18364	0.78396
1/28/18	3	25%	GUITAR Coated Ceramic Fibers from 1/27 Batch 1	116.73870	4.29406	0.28063
1/28/18	3	25%	GUITAR Coated Ceramic Fibers from 1/27 Batch 2	65.74906	1.82229	0.63746
1/31/18	4	25%	GUITAR coated ceramic fibers from 1/27 Batch 1 (Redo)	107.62359	8.00954	0.40553
1/31/18	4	25%	GUITAR coated ceramic fibers from 1/27 Batch 2 (Redo)	90.56589	4.45080	0.26524
1/31/18	4	25%	GUITAR coated ceramic fibers mix of Batch 1&2	79.86605	6.35907	0.87664
2/5/18	5	15%	GUITAR coated ceramic fibers from 2/3 Batch 1	55.65801	0.70664	1.35078
2/5/18	5	15%	GUITAR coated ceramic fibers from 2/3 Batch 2	65.87138	2.42920	0.83906
2/5/18	5	15%	GUITAR coated ceramic fibers from 2/3 Mix of 1&2	65.22990	2.12672	1.06700
2/13/18	6	20%	GUITAR Coated Ceramic Fibers from 2/11 Batch 1	61.88446	0.931066	0.758131
2/13/18	6	20%	GUITAR Coated Ceramic Fibers from 2/11 Batch 2	116.5937	1.948212	0.486503
2/13/18	6	20%	GUITAR Coated Ceramic Fibers Present Mix	102.4777	1.753561	0.447022
2/21/18	7	25%	GUITAR Coated Ceramic Fibers from 2/17 Batch 1	74.76046	1.498315	0.697715
2/21/18	7	25%	GUITAR Coated Ceramic Fibers from 2/17 Batch 2	50.55383	1.534483	0.952798
2/21/18	7	25%	GUITAR Coated Ceramic Fibers Present Mix	62.54501	1.879595	0.773358

A.3: Scanning Electron Microscope Results

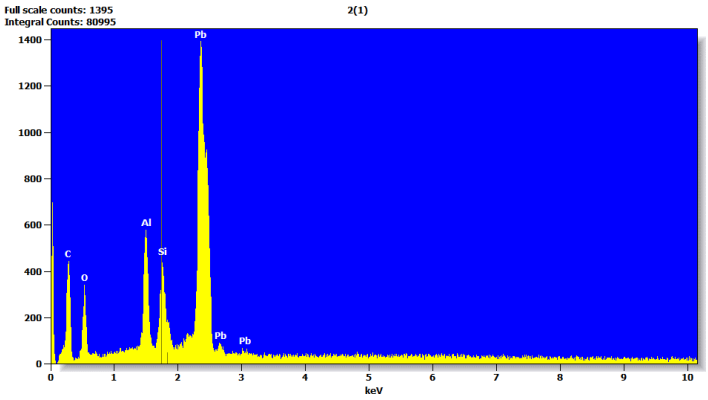

Figure5. This graph is a general EDS survey of the region of the 20% fiber loading positive plate shown in Fig. 6. This shows the presence of primarily Pb, as would be expected, Al and Si from the fibers, O from the positive active material as well as the fibers.

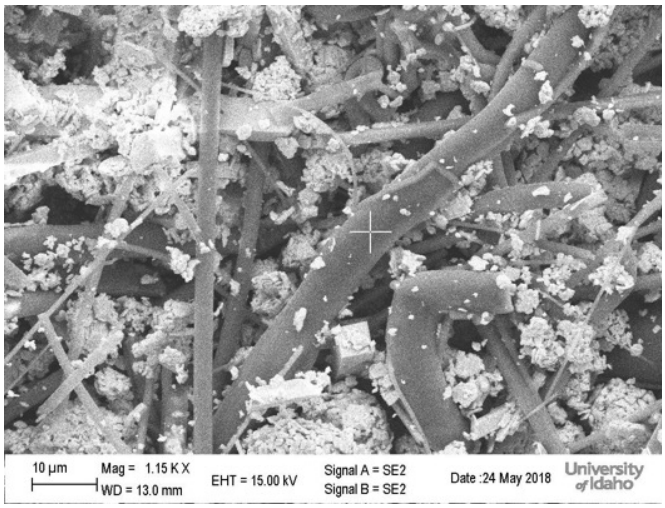

Figure 6. 1.15K X view of the 20% fiber loaded positive plate. The crosshair marks the spot sampled using EDS shown in Fig. 7.

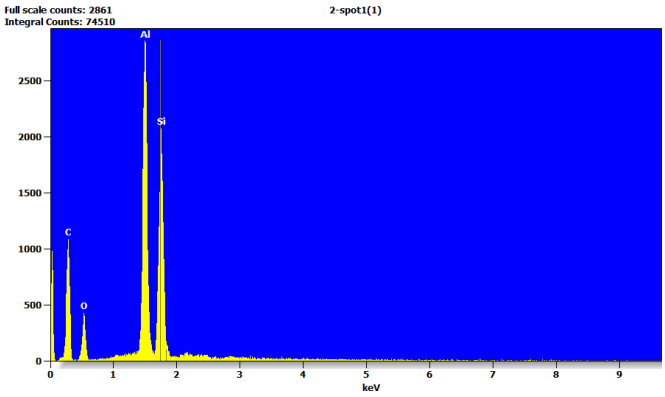

Figure7. EDS analysis of the spot marked in Fig. 6. This indicates the strong presence of Al, Si, and O in the fiber as would be expected. It also shows a strong presence of C which indicates that the GUITAR coating is intact on the fiber.

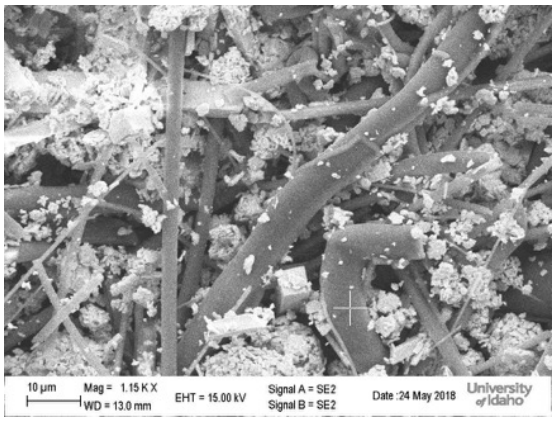

Figure 8. The same view of the plate shown in Fig. 6 except the spot sampled for EDS is moved to a different fiber. Analysis shown in Fig. 9.

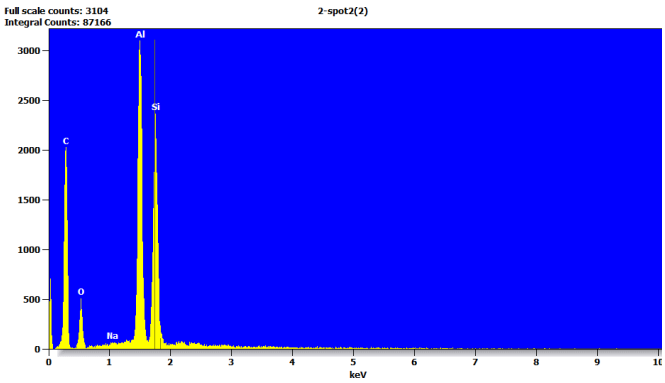

Figure 9. EDS analysis of the spot marked in Fig. 8. This indicates the strong presence of Al, Si, and O in the fiber as would be expected. It also shows a strong presence of C which indicates that the GUITAR coating is intact on the fiber. The indicated presence of sodium is likely indicates that the fibers contain some level of NaO.

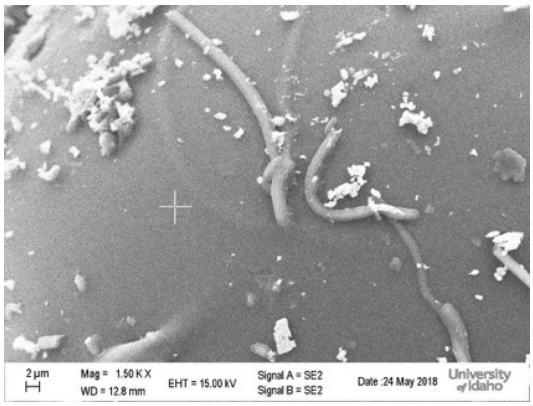

Figure 10. Location of EDS spot scan on a portion of a fiber in the 25% loading positive active plate

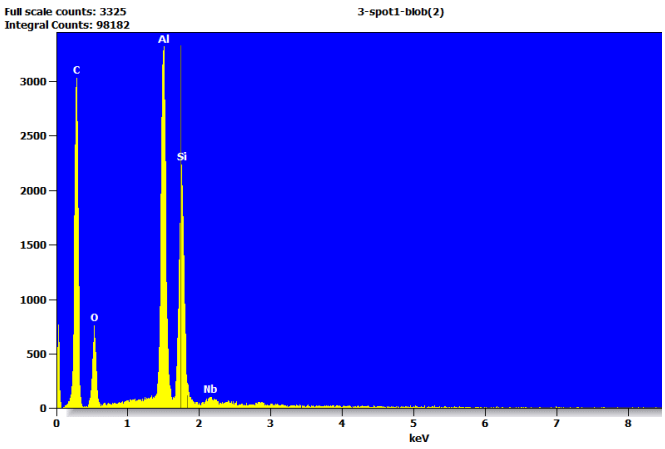

Figure 11. EDS analysis of the spot marked in Fig. 10. As in Fig. 9, the presence of GUITAR on the fiber is strongly indicated. It is unclear as to the source of the Nb peak as there are no elements with x-ray emission energy levels easily confusable with Nb.

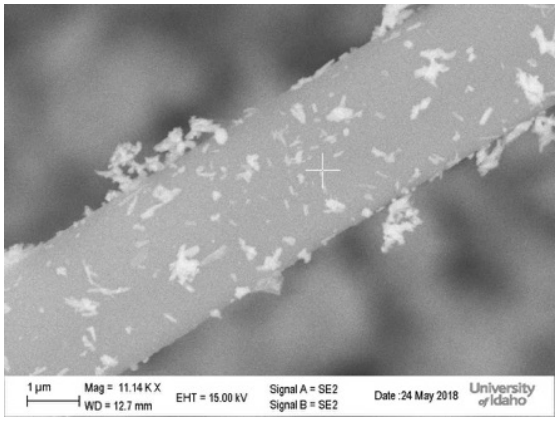

Figure 12. Location of EDS analysis of a fiber found in a sample taken from a 15% fiber loaded positive plate identified as 'charged'. Analysis results shown in Fig. 13

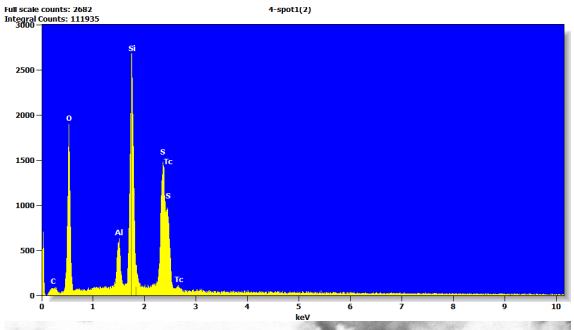

Figure 13. EDS analysis associated with Fig. 12. Only a small amount of C is detected on the sample. This indicates that little if any GUITAR remains on the fiber. S and Tc peak results from an energy level confusion with Pb and indicates a strong presence of Pb on the sample. This is observable on Fig. 12 in the form of the white flakes.

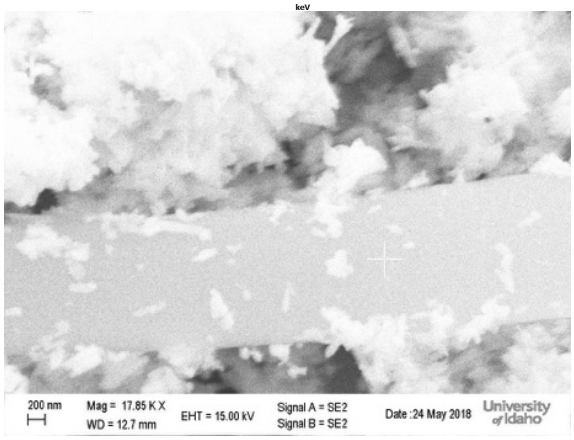

Figure 14. Location of EDS analysis of a fiber found in a sample taken from a 15% fiber loaded positive plate identified as 'charged'. Analysis results shown in Fig. 15

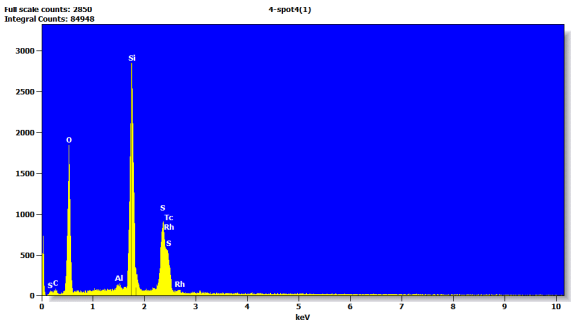

Figure 15. EDS analysis associated with Fig. 14. Only a small amount of C is detected on the sample. This indicates that little if any GUITAR remains on the fiber.
S, Rh, and Tc peak results from an energy level confusion with Pb and indicates a strong presence of Pb on the sample

.

Final Project Report: Office of Undergraduate Research (OUR) – Spring 2018

Grant Recipient: Jacquelin Martinez-Alvarez, Chemical & Materials Engineering, University of Idaho

Faculty Mentor: Dr. Matthew Bernards, Assistant Professor, Department of Chemical & Materials Engineering

Project Title: Air-brushed nonfouling drug delivery patches

Abstract: A significant challenge in the field of biomaterials is the nonspecific adsorption of proteins to implants. Upon implantation, this nonspecific protein adsorption triggers the natural foreign body response leading to encapsulation and failure of the device. Zwitterionic materials are excellent at resisting protein adsorption. For this reason, we are investigating the zwitterionic polymer poly(sulfobetaine methacrylate) (polySBMA). Using polySBMA, our goal is to produce nonfouling-polymer-microfibers by airbrush-spraying. Airbrush-spraying is a novel and innovative technique. To date we have explored the influence of spraying pressure, nozzle diameter, distance to collector, polymer molecular weight, and solvent. We have also optimized the use of a photo-polymerization reaction to reduce the water solubility of the resulting microfibers. The long term goal is to use these microfibers to create a high-surface-area drug delivery platform.

Project Accomplishments

1. Perfected polymerization technique
   Description: Free-radical polymerization was used to produce polySBMA. The reaction took place under nitrogen protection. In the reaction, varying concentrations of potassium chloride (KCl) were used to vary the molecular weight of the polymer.
   Results: "Mega-batches" of polySBMA, at different molecular weights, were successfully produced. Varying the molecular weight proved to be important in microfiber production. As the concentration of KCl increased, molecular weight decreased, which also decreased fiber diameter. We found KCl to be optimal at a concentration of 2.5 M.

2. Optimal spraying solvent
   Description: The polySBMA was viscous enough to need a solvent for spraying. The following solvents were tested: acetone, ethanol, and aqueous sodium chloride (NaCl(aq)). When testing NaCl(aq), the concentration of NaCl was varied to have an insight as to how fiber diameter changes. KCl concentration was kept constant at 2.5 M.
   Results: PolySBMA was unable to dissolve in acetone nor ethanol, however, it did dissolve in NaCl(aq). As the concentration of NaCl increased, fiber diameter decreased. We found NaCl to be optimal at a concentration of 0.30 M.
   *****Note: It is optimal to have smaller fiber diameter, to allow for high-surface-area.

3. Varied spraying conditions
   Description: To produce uniform microfibers, a variety of spraying conditions were tested: spraying pressure, spraying nozzle diameter, and distance to collector. KCl and

solvent NaCl concentration were kept constant at 2.5 M and 0.30 M, respectively.
Results: Uniform microfibers were produced when pressure was at 30 psi, nozzle diameter was at "2-rotation wide", and the distance from collector to air-brush sprayer was at 10 cm away.

4. Examined the use of a UV-photo-polymerization reaction to reduce water solubility
Description: After a successful production of uniform microfibers, water solubility was tested by soaking the resulting microfibers in water. They instantly dissolved upon exposure to water, thus came the idea of introducing a UV-photo-polymerization reaction to help reduce water solubility of the resulting microfibers.
Results: Water solubility reduced significantly with the use of a UV-photo-polymerization reaction. After exposure to water, the microfibers kept their structure and uniformity.

5. Optimal photo-initiator concentration
Description: Although water solubility was reduced, at the initial tested photo-initiator concentration (introduced in the photo-polymerization reaction), the resulting microfibers had some noticeably large chunks of undissolved photo-initiator within them. For this reason, photo-initiator concentration was examined.
Results: By reducing the photo-initiator concentration from 0.089 M to 0.009 M, mixing was optimized and the photo-initiator chunks were no longer present.

Summary of Budget Expenditures

Supplies	**Cost**
Air-brush sprayer (3x)	$45.06
Photo-initiator (1x)	$112.09
Frame for system (1x)	$403.20
Monomers (2x)	$257.38
Petri dish 100X15mm (1x)	$110.64
Ethanol 1 gal (1x)	$23.63
Poster printing	$48
Total spent	**$1,000**

Conference Presentation: This research was presented at the 2018 UI Undergraduate Research Symposium and at the 2018 Idaho Conference on Undergraduate Research in Boise, ID.

Acknowledgment: This research could not have been as successful as it has been without the generous support of the Idaho State Board of Education. I truly appreciate the support given to me in the form of an Office of Undergraduate Research Grant.

Final Project Report: Office of Undergraduate Research (OUT) Summer Undergraduate Research Grant – Spring 2018

Grant Recipient: Cheyanne Myers, Animal Sciences, University of Idaho

Faculty Mentor: Dr. Gwinyai Chibisa, Department of Animal and Veterinary Sciences

Project Title: Determining what causes differences in feed efficiency in cattle raised on rangeland

Abstract: Currently the global population continues to grow at a fast rate, which is increasing the demand for food. However, given the finite amount of resources, such as land and water, meeting this demand is becoming harder. Therefore, improving production/feed efficiency in animal agriculture could be the solution. In Idaho, the cattle industry is a major part of the economy and most cattle are raised on rangeland. Determining whether feed efficiency for rangeland cattle could be improved will help Idaho producers produce more meat with less cattle and reduce their feed costs. Although there is information on what accounts for differences in feed efficiency in animals raised in intensive management systems (feedlots), not much is known about animals raised on rangeland. Therefore, the objective of my study was to determine whether there are differences in protein metabolism in animals that are classified as efficient and inefficient in converting feed to meat when raised on rangeland. I conducted gene expression analysis for markers of protein synthesis and degradation, and also measured amino acid concentration in blood. Having this information is critical as it will add to the body of knowledge that will enable genetic selection of cattle with high feed efficiency.

Project Accomplishments

1. My first goal was to determine the differences in protein metabolism in efficient vs. inefficient cattle that are raised on irrigated pasture compared to rangeland.

   We know that cattle raised on rangeland have to work harder (traveling to graze and drink water), and deal with a number of stressors, environmental conditions. All of these factors can affect the rates of protein synthesis and breakdown. We know that proteins build up a majority of the body. Proteins function as enzymes, nutrient transporters, and to help the body grow and repair.

   Result: We used q-PCR to determine transcript abundance of markers of protein synthesis and degradation in skeletal muscle samples. Unfortunately, during our runs we noted that we had low RNA abundance. Therefore, we have no numbers to report for gene expression. However, we are currently troubleshooting and trying to determine if we can salvage the situation. I sent 6 samples to the on-campus Genomics Resources Core lab to determine the profile and concentration of RNA in our samples. I am also planning to run RNA integrity gels to determine if our samples can be used for q-PCR. We ordered the supplies that are needed and are waiting for them to be delivered. We will report back to you once we have all that information, and I am continuing to work on the project.

2. My second goal was to determine the plasma amino acid concentration in animals that are efficient vs. inefficient

Determining plasma 3-methylhistidine, urea-N and amino acid concentration can be useful in studying protein metabolism. Amino acids are the building blocks for protein. However, body protein can be broken down to provide amino acids in times of need, which can cause muscle wasting. Muscle wasting can cause an increase in the concentration of 3-methylhistidine in blood. Amino acids in excess of requirements cannot be stored and are further broken down to a carbon skeleton and ammonia. Ammonia ends up converted to urea-N, which is then excreted in urine.

Result: There were no differences (P = 0.214) in the plasma concentration of 3-methyhisitidine, an indirect indicator of muscle protein breakdown. We observed no differences (P = 0.750) in the blood urea-N (BUN) concentration. Blood urea-N concentration can be used as a measure of amino acid breakdown. Based on the 3-methylhistidine and BUN data, it is possible that there were no differences in body protein breakdown between efficient and inefficient cattle. Plasma Cit concentration was higher (P = 0.025) whereas plasma Try concentration tended (P = 0.088) to be higher in inefficient than efficient cattle. We also noted that the concentrations of Ser ended (P = 0.088) to be higher in efficient compared to inefficient cattle. However, the plasma concentrations of Asp, Thr, Asp, Glu, Gln, Pro, Gly, Ala, Val, Met, Cys, Iso, Leu, Tyr, Phe, Lys, Arg, His and Orn did not differ ($P \geq 0.139$) across treatments.

Summary of Budget Expenditures

Supplies	**Cost**
TF 5X-TAQMAN FAST UNIVERSAL ($1,000 from this award, remaining $42.85 provided by mentor)	1,042.85
TOTAL	$1,042.85

Conference presentations: The poster submitted with this project was presented at both the UI university-wide Undergraduate Research Symposium in Moscow, ID, as well as at the ASAS convention in Vancouver, BC, Canada, in July 2018.

Acknowledgement: I would like to acknowledge the University of Idaho and the Idaho State Board of Education for providing funding in the form of an Undergraduate Research Grant. This project has been a huge and very positive learning experience for me. Without the funding provided to me through this program, I would not have been to conduct this research. Thank you!

Final Project Report: Office of Undergraduate Research (OUR) Undergraduate Research Grant – Spring 2018

Grant Recipient: Frankie Scholz, Biological Sciences, University of Idaho
Faculty Mentor: Dr. Tanya Miura, Department of Biological Sciences

Abstract: Respiratory syncytial virus (RSV) is an intracellular pathogen that infects people of all ages. RSV is responsible many deaths each year and currently, there is no licensed vaccine. In an alternate form of therapy, monoclonal antibodies can be used to treat infection by neutralizing the virus. We want to investigate the ability of RSV to mutate under stress of a human monoclonal antibody, D25. We hypothesized that RSV will mutate under stress of a sub-inhibitory dose of D25 resulting in escape from neutralization. Molecular modeling done by our collaborators will also accurately predict these mutations. To test this, we introduced RSV to rounds of selection in the presence of D25 and allowed time for mutations to arise. After ten rounds of selection in HEp-2 cells, viral mutants required significantly more antibody for neutralization. The mutants were sequenced for specific amino acid changes and compared to the modeled predictions done by our collaborators. These results will help us better understand how RSV evolves to escape neutralization.

Project Description: The antibody response is crucial for prevention and treatment of RSV. Many antibodies are in development, including D25. The development of a vaccine based on the F protein found on RSV is currently a high priority in the field. RSV is capable of mutating and evolving to escape antibody recognition to avoid neutralization. In this study, we want to select for antibody escape mutations with antibody D25 in the F protein of RSV. Our findings will aid in the work of our collaborators in the physics department who are modeling the F protein to predict possible escape mutations the virus may develop to evade the antibody recognition.

We hypothesize that RSV will mutate under stress of a sub-inhibitory dose of antibody D25 resulting in escape from neutralization. We also predict that molecular modeling done by our collaborators will accurately predict these mutations. To test this, we exposed the virus to antibody D25 in a dilution that hinders the virus but, does not completely neutralize it. This was done in a low dose of D25 (0.16 µg/mL) for five passages. The mutant populations from the five passages were then hit with a higher dose of D25 (2.5 µg/mL) and pressured for another five passages of selection. In this way, the virus will adapt and form mutations to escape the antibody (*See Figure 1.1)*.

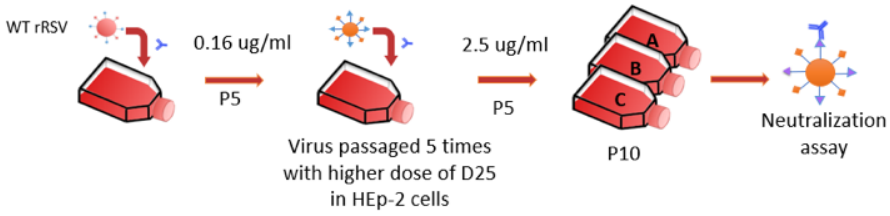

Figure 1.1 *Selection of Antibody Escape Mutants*
HEp-2 cells were incubated with wild-type virus infection. Neutralizing antibody D25 was introduced in a low dose then a higher dose to select for natural mutations in the F protein that allow virus to grow in the presence of D25.

We used genetic sequencing to identify the antibody escape mutations. Further experiments will confirm that these mutations lead to antibody escape and determine how the mutations affect the growth of RSV in the absence of antibodies. This study will not only lead to an understanding of how RSV changes to avoid antibody neutralization but, will also provide data to test the predictions made by molecular modeling.

Project Accomplishments: Thus far, data illustrates that a significantly higher dose of antibody D25 is required to completely neutralize the passaged RSV compared to that of the wild-type RSV. The wild-type RSV that was used to begin the passage experiments was completely neutralized at 1.3 µg/ml, and populations passaged 10 times in the presence of D25 now require >80 µg/ml of antibody to completely neutralize the virus *(See Figure 1.2).*

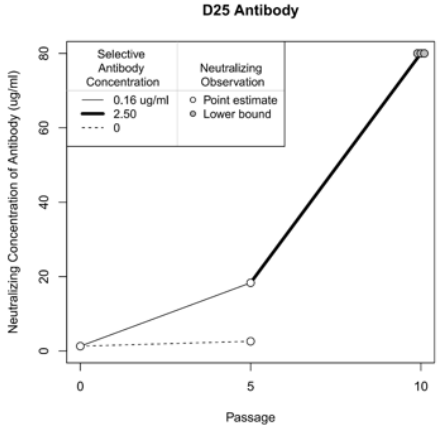

Figure 1.2 *Neutralizing Antibody Concentration of Mutants Across Passages*
Neutralizing Concentrations were obtained through neutralization assays. HEp-2 cells were incubated in a 96-well plate with 1:2-fold dilutions of D25. Cells were monitored for viral infection for 7 days.

The virus populations passaged five times in 0.16µg/ml of D25 and those passaged an additional five in 2.5µg/ml for a total of ten passages were isolated for their RNA, reverse transcribed to cDNA, and then further amplified by PCR. The PCR products were sent to Elim BioPharm for sequencing of the F gene.
Data received from the sequencing shows a single point mutation in the F protein in mutants evolved from the first five passages of selection: N208Y. In this mutation, an asparagine residue was mutated to a tyrosine and this change alone prevents the access of D25 to a small hydrophobic pocket on the F-protein by steric hindrance. A second point mutation arose in addition to the first in the mutant populations that were passaged ten times in the presence of D25: Q202R. This mutation of a glutamine to an arginine abolishes three hydrogen bond interactions with D25 originally present in the wild-type. Both mutations affect the ability of D25 to bind and interact with the F-protein. These data suggest that RSV successfully evolved to escape neutralization by D25.

Budget Expenditures:

Materials	**Cost**
Plasmid Preparation Kit	$250
Mutagenesis Reagents	$300
Chemicals to make buffers	$50
Plastic ware	$225
Cell culture media	$100
Poster	$75
Total	$1,000

I presented a poster of my work at the UI Undergraduate Symposium in April of 2018 and at the 2018 Idaho Conference of Undergraduate Research (ICUR) in Boise.
Acknowledgement: I would like to thank the State Board of Education for providing me the opportunity to conduct my research. I am very proud of the research I did this and I learned a tremendous amount that will have a large impact on the rest of my future endeavors. Without the support from SBoE, I would not have been able to participate in this research.

Final Report: Office of Undergraduate Research, Summer Undergraduate Research Fellowship, summer 2018

Fellowship Recipient: David Behrens, Department of Geological Sciences
Mentor: Dr. Jeff Langman, Department of Geological Sciences
Project title: Evolution of Carbonate Weathering and Nanoparticle Release

The purpose of this experiment was to evaluate detection methods of a new mechanism for carbonate weathering—ejection of nanoparticles from the mineral surface by unidentified repulsive force(s). This new mechanism of carbonate weathering has recently been detected (Levenson and Emmanuel, 2017a) and heavily debated (Le Merrer and Colombani, 2017; Levenson and Emmanuel, 2017b). Such a mechanism could explain why geochemists have struggled to quantify the dissolution rate of carbonates. For this study, it was hypothesized that the use of a dynamic light scattering (DLS) analyzer could detect solution nanoparticles ejected from the surface of the carbonate mineral that would allow for quantification of the nanoparticle distribution and stability (zeta potential). The original proposal was to use smithsonite [$ZnCO_3$], but sufficient quantities for a reasonable price could not be located; therefore, the subject mineral was changed to calcite, which was used by Levenson and Emmanuel.

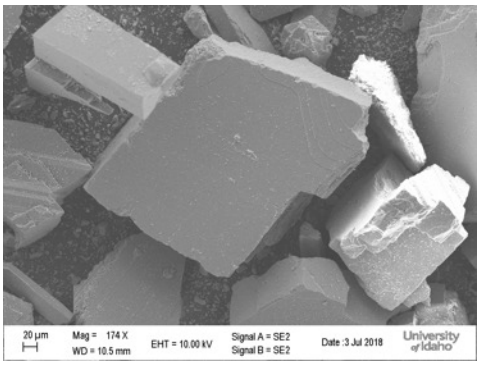

Figure 1. Scanning electron microscope image of calcite grains used in the weathering experiments.

To facilitate the weathering of the calcite and produce a solution for analysis, four weathering chambers were constructed (Fig. 2). A non-traditional design was chosen to enhance the rate of weathering and allow for a more rapid production of potential ejected nanoparticles. The chambers were comprised of 20-cm long, clear plastic tubing with a 5-cm diameter. A black rubber cap and air valve was installed on one end, while the other end contained a layered construction consisting of protective mesh, 23-µm filter, 11-µm filter, protective mesh, snap in drain, and rubber cap with drain spigot. The filter end allowed for draining of each chamber after each experiment. A small hand pump could be attached to the top valve, which allowed for air to be pumped into the tube to force water through the filters. Each weathering chamber was filled with an aqueous solution of a variable volume, typically one circumneutral and the other slightly acidic at each temperature condition. While the weathering chambers were in use, they were placed on shaker tables set to 80 rpm, which was believed to be sufficient to minimize boundary layer issue but not fast enough to inadvertently cause physical weathering processes (collision). In order to test Arrhenius behavior of the weathering processes, two of the chambers were placed in a walk-in refrigerator at 5ºC and two chambers in the lab at 21ºC.

Each of weathering chamber contained 100 g of ground calcite. The calcite was ground to a diameter range of 125 to 300 µm to maximize available surface area for weathering. It was hypothesized that any particles that passed the 11-µm filter would have been produced by the particle-ejection mechanism. The drain water was collected after each

experiment for analysis as raw water (unfiltered) and 450-nm filtered water to examine a potential large range of micro- to nano-particles (raw) and nanoparticle-only range (<450 nm). All samples were analyzed for particle size distribution and zeta potential (stability) with the DLS analyzer.

Figure 2. Images of the weathering chambers on the shaker tables and in the drain stand setup.

Initial experiments did not produce the expected range of particles or the particle concentration was below detection limits. Believing the initial results were due to low concentrations of the particles in solution, the amount of water in the tubes was reduced, the pH of the solution was adjusted, and the length of time that the tubes were agitated was increased. During the course of the experiments, the water from the weathering chambers underwent several other tests to obtain relevant environmental data. For each drain solution pH, Eh, and electrical conductivity were measured, which allowed fro the determination of the amount of buffering and dissolution to be quantified. Initial data indicated that the conductivity of the water remained relatively low until the acidity was substantially increased. A Hach spectrophotometer was used to measure water hardness, to determine the mass of calcite that was being lost during each experiment. Unfortunately, these experiments did not detect particles of the predicted size.

In order to compensate for the unsuccessful weathering chamber experiments, small scale experiments were instituted alongside the chamber experiments. The DLS can be set up to allow for water to flow through the detector, but the equipment necessary is expensive and would require a larger experiment. To replicate this “flow through” design, 100 mg of calcite was added directly to DLS cuvettes with 4 mL of water at neutral, slightly acidic and very acidic conditions. These cuvettes were placed on the shaker table with the larger weathering chambers and analyzed with the chamber samples. While these did yield particles in solution in the water, results were inconsistent between trials.

It is difficult to draw specific conclusions since the nanoparticles were never consistently detected. It is possible that the original study that examined the ejection process solely by examining changes to the mineral surface was not detecting nanoparticle ejection but area-specific (lattice point) dissolution of the carbonate mineral surface at specific locations. If the ejection weathering mechanism does occur, a few possibilities exist for why they were not detected under these experimental conditions. First, it is possible that the ejected nanoparticles are not stable and quickly dissociate into their constituent ions in solution. Additionally, it is possible that the nanoparticles are produced, but they are produced at such low concentrations as to not be detected by the DLS. This possibility also offers a potential reason that these particles have not previously been identified; they are not a major component of the weathering of calcite.

References

Le Merrer, M., Colombani, J., 2017. Comment on “Repulsion between calcite crystals and grain detachment during water-rock interaction” by Levenson and Emmanuel, 2017. Geochem. Perspect. Lett. 1–2. https://doi.org/10.7185/geochemlet.1747

Levenson, Y., Emmanuel, S., 2017a. Repulsion between calcite crystals and grain detachment during water–rock interaction. Geochem. Perspect. Lett. 133–141. https://doi.org/10.7185/geochemlet.1714

Levenson, Y., Emmanuel, S., 2017b. Reply to comment on “Repulsion between calcite crystals and grain detachment during water-rock interaction” by Le Merrer and Colombani, 2017. Geochem. Perspect. Lett. 3–4. https://doi.org/10.7185/geochemlet.1748

Budget

Material	Supplier	Unit Cost	Units	Subtotal	Total
Hach hardness kit	Hach	$74.05	2	$148.10	$165.89
Shaker table	Sonic Supply	$325.00	1	$325.00	$337.44
Calcite (Bulk pack 1 kg)	VWR	$31.00	2.5	$77.50	$84.54
Mortar and pestle	Amazon	$206.00	1	$206.00	$219.35
Filters	Cole Palmer	$20.71	1	$20.71	$30.63
Caps + drains	Amazon	$3.30	8	$26.40	$46.12
Plugs and felt	Spence’s			$15.00	$46.23
2” tubing	Grainger	$41.40	2	$82.80	$82.80
				Total:	$1,013.00

*The SURF award provided $1,000 in project-related supplies and a $4,000 student fellowship. The remaining funds ($13) were provided by Dr. Langman.

Acknowledgement: The support provided by the State Board of Education in the form of a Summer Undergraduate Research Fellowship was greatly appreciated. I would not have been able to participate in this research project or gain the experience I did. Thank you very much.

Final Project Report: Office of Undergraduate Research (OUR) Summer Undergraduate Research Fellowship (SURF) – Summer 2018

Fellowship Recipient**:** Zachary Blume, Department of Biological Sciences

Faculty Mentor**:** Dr. Diana Mitchell, Department of Biological Sciences

Project Title: Modulation of the Retinal Immune Environment in a Zebrafish System of Rod Photoreceptor-Specific Degeneration

Abstract: Activated and pro-inflammatory microglia, along with accompanying local inflammation, are associated with human retinal degenerative disease. However, it remains unclear if these aspects of the immune response are symptomatic or directly initiate and/or contribute to disease pathology, such as the death of additional retinal neurons. One hypothesis for continued loss of neurons in retinal degenerative disease is that microglia may engulf, or possibly initiate cell death of, otherwise healthy neurons. Our project attempts to test this hypothesis using a zebrafish system in which rod photoreceptors die due to a toxic transgene (XOPS:mCFP), but cone photoreceptors survive. We first characterized microglial characteristics in XOPS:mCFP retinas compared to wildtype and found that microglia localize to the photoreceptor layer and engulf dying rods, but total numbers of microglia are similar. Next, we successfully induced a pro-inflammatory retinal immune environment by intraocular injection of zymosan (a pro-inflammatory compound), as indicated by infiltration and division of immune cells in the retina and gene expression of selected transcripts. Our next goal is to determine if this induction of a pro-inflammatory retinal environment may result in subsequent cone death or disappearance in XOPS:mCFP retinas, thus directly probing contributions of a dysregulated immune environment to retinal degenerative disease.

Project Accomplishments:

1. Our first goal was to show that we could induce an inflammatory immune response in the zebrafish retina. More specifically, in the retina of a zebrafish transgenic line with rod-photoreceptor specific degeneration.
    a. The retina contains two distinct types of photoreceptors responsible for vision: rods and cones. Rods are responsible for dark/light distinction and visibility in dimmer light, while cones are responsible for brighter, color vision. In humans (and mice), when rod photoreceptors degenerate due to a genetic mutation, cones inexplicably die as well. One hypothesis for this subsequent cone death is microglia activation – activation of the resident immune cells of the retina. It is thought that by responding to the programmed rod death the microglia may inadvertently consume or kill cones via proinflammatory mechanisms. However, in a zebrafish system in which rods die due to a rod-specific transgene, the cones survive. Our goal was to show that we could activate the microglia in that zebrafish system.

Results: We used the compound zymosan, which is a fungal carbohydrate molecule that mimics infection (by binding TLR 2). Zymosan triggers an immune response without the resulting pathology of a real infection. We found that we were able to induce

an inflammatory response in the retina shown by increased immune cell infiltration and up regulation of selected proinflammatory genes in zymosan injected eyes.

2. Our second goal was to determine if the induced proinflammatory state resulted in subsequent cone death.

Results: We found that cell death slightly increased in zymosan injected eyes when compared to saline injected control eyes. Interestingly, we found (using the fluorescent cyan reporter for rods) that the increase in cell death appears to be attributed to cell population other than rods in zymosan injected eyes.

3. Our third goal was to determine if the induced proinflammatory state resulted in subsequent increase in cell proliferation
    a. Zebrafish have the incredible ability to regenerate their retinal tissue in response to damage. An increase in cell proliferation following a proinflammatory induced state may indicate an attempt at regeneration in response to damage caused by immune activation.

Results: We found that cellular proliferation showed a trend of increasing in zymosan injected eyes when compared to saline injected controls eyes, although it was not statistically significant.

Future Directions: From this experiment we have proved we can induce inflammation in the zebrafish retina. The future of this project will be to determine if sustained inflammation (for longer periods) in the retinal microenvironment may result in subsequent cone death or other signs of pathology in the rod-specific degeneration line of zebrafish. This will be more akin to simulating a chronic degenerative disease that we observe in humans. Moving forward we hope to directly probe the contributions of a dysregulated immune environment to retinal degenerative diseases.

Summary of Budget Expenditures:

Integrated DNA Technologies (IDT) qPCR primers	$285.24
LifeTechnologies Superscript IV cDNA synthesis kit and Power SYBR Green qPCR mix	$714.55
Subtotal for supplies	$999.79
Stipend (before tax)	$4,000.00
Total	$4,999.79

Conference Presentation: I presented a poster of my work at the 2018 Idaho Conference on Undergraduate Research (ICUR) at Boise State University and I will be presenting my research again at the UI Undergraduate Research Symposium in April 2019 as well.

Acknowledgement: The support provided by the State Board of Education in the form of a Summer Undergraduate Research Fellowship was genuinely appreciated. The experience is one that I feel was inexplicably valuable. It opened new opportunities for a career path I had never considered before, and further invigorated my curiosity towards my field of study. Only with this support from the SBOE was I able to participate in this research, for which I am extremely grateful.

Final Project Report: Office of Undergraduate Research (OUR) Summer Undergraduate Research Fellowship (SURF) - Summer 2018

Fellowship Recipient: Beau Horenberger, Mathematics, University of Idaho

Faculty Mentor: Dr. Jennifer Johnson-Leung, Department of Mathematics, University of Idaho

Project Title: Calculating Siegel Modular Forms

Abstract: The aim of this research project was to build a code base for calculating Siegel modular forms of paramodular level N. Siegel modular forms have Fourier expansions indexed by binary quadratic forms. Thus, the first step in representing Siegel modular forms is to identify and calculate good representatives for appropriate equivalence classes of these binary quadratic forms. This is the essential problem that was solved in the course of this research. This code base will have practical use for further research in Number Theory, specifically in verifying examples of the paramodular conjecture. The resultant objects also have applications to hyperelliptic curve cryptography. The project will be mentored by Jennifer Johnson-Leung, who will use this computational procedure for further research.

Project Accomplishments

1. The first goal was to show that the index of $\Gamma_0(N)$ in $SL_2(\mathbb{Z})$ was finite so that we could generate finite cosets of binary quadratic forms.

This was achieved in a series of proofs calculating the cardinalities and indexes of related sets. It was shown first that $|SL_2(\mathbb{Z}/p^e\mathbb{Z})| = p^{3e}(1-1/p^2)$, then $|SL_2(\mathbb{Z}/N\mathbb{Z})| = N^3\prod_{p|N}(1-1/p^2)$, so this is the index $[SL_2(\mathbb{Z}) : \Gamma(N)]$. Next, we found that the map $\Gamma_1(N) \to (\mathbb{Z}/N\mathbb{Z})$ given by $\left(\begin{smallmatrix} a & b \\ c & d \end{smallmatrix}\right) \to b \bmod N$ surjects and has kernel $\Gamma(N)$ and that the map $\Gamma_0(N) \to (\mathbb{Z}/N\mathbb{Z})^*$ given by $\left(\begin{smallmatrix} a & b \\ c & d \end{smallmatrix}\right) \to d \bmod N$ surjects and has kernel $\Gamma_1(N)$. From these, we derived that $[SL_2(\mathbb{Z}) : \Gamma_0(N)] = N\prod_{p|N}(1+1/p)$, as desired.

2. Next, we aimed to prove that the cosets of $\Gamma_0(N)$ in $SL_2(\mathbb{Z})$ had a method for determining distinguished representatives.

This was achieved by proving there is a bijection between the cosets of $\Gamma/\Gamma_0(N)$ and the projective space $\mathbb{P}^1(\mathbb{Z}/N\mathbb{Z})$. Once this was done, we proved one could generate representatives for the cosets by showing all members of the projective line $\mathbb{P}^1(\mathbb{Z}/p^n\mathbb{Z})$, with p a prime and n a natural number, of the form $(1:u)$ where $u = 0, 1, .., p^n - 1$ and $pu, 1$ where $u = 0, 1, p^{n-1} - 1$ represent different equivalence classes. Thus, we could compute representatives using this as the basis for an algorithm.

3. The next goal was to implement these proofs in a program which could calculate

representatives for binary quadratic forms.

The program was written in C++ to efficiently calculate these representative binary quadratic forms in their matrix form. Additional functions and classes were written to handle math- ematical operations involving matrices, primes, and moduli.

4. Finally, we intend to use this program to calculate the Fourier coefficients for twists of Siegel paramodular forms.

Work has begun on this end, and the program is still under development. Although more work remains to generate and twist coefficients, the analysis of the coefficients already has a code base from the previous goal, making the remaining work minimal. This work will be continued to completion in approximately the next month.

Summary of Budget Expenditures:

1. Stipend: $4000

2. Cost for UI Undergraduate Research Symposium Presentation: $75

3. Travel expenses for presenting research at AMS National Meeting in Batimore, MD:

(a) Flight to Baltimore, round trip: $450 (b) Hotel for 3 nights: $225

4. Misc. Project expenses: $250

Total expenses (sans stipend): $1,000 + $4,000 stipend

Acknowledgement:

I would like to sincerely thank the State Board of Education for the wonderful oppor- tunity I was provided through the Summer Undergraduate Research Fellowship. The support provided by the SBOE made this a truly rewarding eye-opening experience for me.

Final Project Report: Office of Undergraduate Research (OUR) Summer Undergraduate Research Fellowship (SURF) - Summer 2018.

Fellowship Recipient: Hannah Jaeger, Biological Sciences, University of Idaho
Faculty Mentor: Elizabeth Fortunato, Professor, Department of Biological Sciences

Project Title: Determining the Benefit Human Cytomegalovirus Gains by Down Regulating the Basement Membrane Protein Nidogen-1

Abstract:
Human Cytomegalovirus (HCMV) is the most prevalent cause of neurological birth defects, ranging from microcephaly to sensorineural hearing loss. This study aims to elucidate the benefit HCMV derives from modifying a particular cellular process to more efficiently disperse infected cells. Within 6-8 h post infection, HCMV begins to downregulate Nidogen-1 (NID1), an important component of the extracellular matrix (ECM) secreted by endothelial cells, by both protein stability and decreased mRNA transcription. To determine if the absence of NID1 increases dispersal of HCMV, we have designed a series of transmigration assays that utilize human umbilical vein endothelial cells (HUVECs) seeded onto a polycarbonate membrane. THP-1 monocytes are seeded on top of the HUVEC monolayer and total transmigration of the monocytes is measured after 24 and 48 hours. Infection of HUVECS has been shown to increase this transmigration rate, presumably via ECM modifications. Five different treatments of HUVECs, ranging from full HCMV infection to just NID1 knockdown, were used to test our hypothesis that downregulation of NID1 increases transmigration. Preliminary results with uninfected monolayers yield an average of 24% transmigration. Ultimately, we believe the targeting of NID1 provides HCMV a selective advantage, which exacts a negative toll on the developing fetus.

Project Accomplishments:

1. Development of CRISPR knock out cells for NID and control CRISPR

A. Lentivirus transduction and initial verification.
HUVECs have been successfully transduced with a previously verified NID1 KO CRISPR and control CRISPR encoding lentiviruses, followed by selection with puromycin to ensure delivery of the lentivirus genome (encoding both Cas9 and NID1 targeting guide RNA). After a short selection in puromycin, NID1 KO and control resistant cells were seeded at an equal density and harvested 72 h post plating for supernatant and cell lysate analysis for NID1 via Western blot. Initial analysis showed strong NID1 knockdown. However, after several passages of pooled cell populations, NID1 levels returned to control levels, indicating single cell cloning was necessary to obtain populations with strong/continuous NID1 knock out before preforming the transmigration assays.
B. Single Cloning
We seeded approximately 50-100 HUVEC CRISPR NID1 Knock out and CRISPR control cells onto 10cm plates. Single clones that were large enough to be visible to the eye were circled and then evaluated to make sure no other clones were touching or too close. Colonies were carefully removed and placed into separate wells until cell counts were high enough to analyze via Western blots. We were are currently analyzing NID1 levels in these single clones. A population will be selected that have NID1 knocked out and then transmigration assays will be performed.

2. Infection of HUVECs with HCMV and Adenovirus

A. Monitoring infection of HUVECs

HUVECs were infected with HCMV at an MOI of 15 or mock infected for four hours after which time fresh media was added. HUVECs were also infected with either a backbone Adenovirus or one encoding HCMV tegument protein pp71 for 30 mins at room temperature, then fresh media was added. After 24 hours, all wells were washed and fresh media was added. We were able to successfully monitor the infection by staining coverslips and counting the percentage of infected cells using antibodies against viral proteins. Between 80-90% of cells were successfully infected.

B. Infection of transwell monolayers.

Once a confluent monolayer was formed the same method of infection was used. After 24 hpi monolayers were rinsed and transmigration assays were performed.

Results: More migration of THP1s (about 8%) was seen in infected monolayers as compared to the uninfected controls. Adenovirus infections (using a multiplicity of infection of 10) were too harsh and killed most of the monolayer. Further testing has shown that adenovirus infections at an MOI=1 are sufficient to deliver pp71 to all cells. A second round of infections is currently underway.

3. Transmigration Assays

The main goal of this project was to determine if knock down of NID1 plays an important role in disseminating HCMV. To test this we used transmigration assays of parental HUVECs, CRISPR KO cells, HCMV infected monolayers, and adenovirus carrying pp71 infected monolayers. We were able to test several different monolayers of the parental HUVECs as well as just the transwell insert to determine a baseline for the other cells.

Results: Migration of THP1s was approximately 27% per 24 hours in just the transwell compared to transwells that had a confluent monolayer of HUVECs which was about 12% per 24 hours. The CRISPR cells were initially tested, however, results matched the parental cells due to the high amounts of NID1 within the population of cells. Migration of THP1s through HCMV-infected HUVEC monolayers was higher than the mock, but further testing will need to be done to repeat these results. The adenovirus infection was initially tested, but the infection will need to be adjusted to see the affects that pp71 has on migration.

Budget (not including research stipend- $4000)

DESCRIPTION	UNIT COST	TOTAL COST	DESCRIPTION	UNIT COST	TOTAL COST
Human Endothelial Cell Growth Medium	105.47	316.41	INSERT,24W PLT,PET,8UM CS48	137.01	137.01
Shipping	64.25	64.25	VWR PASTEUR PIPET 9IN CS1000	49.12	49.12
Nidogen-1/Entactin Mouse anti-Human, Clone: 302117, R&D Systems™	279	279	FLASK TC PLG CP 550ML CS50	80.38	$80.38
Fisherbrand™ Easy Reader™ Conical Polypropylene Centrifuge Tubes	56.96	56.96	S&H	3.98	3.98
Oligoes x 2 ea	6.08	6.08	Liquid Nitrogen	2.61	2.61
S&H	4.2	4.2	**Total**		1000

Final Project Report: Office of Undergraduate Research (OUR) Summer Undergraduate Research Fellowship (SURF) – Summer 2018

Fellowship Recipient: Jared Lambert, Biological Sciences, University of Idaho

Faculty Mentor: Diana Mitchell, Professor, Biological Sciences, University of Idaho

Project Title: Live Imaging to Probe the Role of Microglia in Developmental Apoptosis in the Zebrafish Retina

Abstract: During mammalian retinal development, programmed cell death (apoptosis) occurs in large waves in a spatio-temporal fashion to generate functional retinas. In zebrafish comparably smaller waves have been observed and are thought to represent fine-tuning of developing retinal tissue (Biehlmaier 2001). It is appreciated that tissue resident macrophages clear apoptotic cells, however, specific roles for microglia in cell survival/death and clearance during retinal development in zebrafish have not been documented (Petrie 2015). We used an inducible system to specifically deplete macrophages/microglia during retinal development and found an increased number of apoptotic cells in the retina compared to controls. This finding suggests that microglia clear larger numbers of apoptotic cells than is currently appreciated, or alternatively, that microglia provide survival signals to developing retinal cells. To address clearance of apoptotic cells during zebrafish retinal development in real-time, we live imaged fluorescently labeled retinal microglia together with apoptotic cells using acridine orange (AO). We observed that microglia sense and engulf cells prior to AO incorporation, and that engulfed apoptotic cells undergo dynamic movements as microglia continue active migration. This suggests that apoptotic cells visualized in fixed tissues using AO may not represent true levels of apoptosis and their retinal locations may differ from where apoptosis was initiated.

Project Outcomes

1. Our first goal was to determine the optimal live imaging conditions to visualize the retina of embryonic zebrafish.

We needed to visualize developing retinas for a period of 8 hours. To do this, we used a transgenic zebrafish that expresses a fluorescent marker on macrophages, and acridine orange to visualize the apoptotic cells in the retina. Zebrafish are sensitive to environmental conditions, and so we used a climate control box on a Nikon Spinning Disk Confocal microscope to maintain environmental conditions during the imaging process, and limited the exposure to lasers in order to keep the fish alive while trying.

2. Our Second goal was to determine the role of microglia in developmental apoptosis within the zebrafish retina.

Microglia are the macrophages of the Central Nervous System (CNS), and are known for their immune functions. Preliminary data showed an increase in developmental apoptotic cells in retina that had been depleted of microglia. Using live imaging, we sought to determine if they were actively involved in clearing out apoptotic cells, or if they were sending survival signals to keep cells from apoptosis.

Result: Microglia were visualized actively engulfing apoptotic cells.

3. Quantifying the rate of clearance of apoptotic cells by microglia, and duration of acridine orange signal.

After visualizing the retinas, we determined the rate of clearance of apoptotic cells by microglia over the 8 hour period. We found that microglia clear out apoptotic cells at a rate of about 1.2 hours During this quantification, we also noticed that microglia would phagocytize apoptotic cells before the acridine orange marker would appear, which means that they were sensing the cells before they reached DNA fragmentation. The signal would last anywhere from 10-80 min. This means that the microglia probably sense the apoptotic cells long before the marker appears, and that the time for them to digest the apoptotic cells differs.

4. Quantifying displacement and speed of apoptotic cells.

We noticed that apoptotic cells would be moved about by the microglia once they were phagocytized. We quantified the displacement and the speed of apoptotic cells, and found that the displacement varied between cells, but that the speed of the cells was consistent. The average speed for was around 1.5μm/min, which is similar to other experiments done on microglia outside the retina.

Jackson Immuno fluorescently conjugated secondary antibody $307.63
Biovision CaspGLOW caspase staining kit $223.50
Fisher Scientific superfrost slides $468.85

Budget

Supplies	Cost
Jackson Immuno Fluorescently Conjugated 2° Antibody	$307.63
Biovision CaspGLOW caspase staining kit	$223.50
Fisher Scientific superfrost slides	$468.85
Subtotal Supplies	$999.98
Stipend (Before Tax)	$4000.00
Total	$4999.98

Conference Presentation: The poster was presented at the 2018 Idaho Conference of Undergraduate Research (ICUR) in Boise, Idaho. It will also be presented at the 2019 University of Idaho Undergraduate Research Symposium.

Acknowledgements: I appreciate this research opportunity that was made possible by the Idaho State Board of Education, and plan to continue the research that was started this summer during the course of the next year. Without these funds I would not have been able to carry out the research.

Final Project Report: Office of Undergraduate Research (OUR) Summer Undergraduate Research Fellowship (SURF) – Summer 2018

Fellowship Recipient: Garrett E. Larson, Biological Sciences, University of Idaho

Faculty Mentor: Kristopher V. Waynant, Assistant Professor, Chemistry Dept

Project Title: Ionic and Biomolecular Movement through Functionalized Thin Filmed Polymers

Abstract: Ions and biomolecules are essential for many functions of the human body such as bone strength and development, muscle contractions, and cell functions like membrane transport and membrane potentials. This experiment will use post-polymerization functionalization to bind to Calcium ions (Ca^{2+}), using ion selective electrode polymers; this binding could be a way of monitoring calcium levels in the body. The polymer scaffolding will be made from Poly-(3-sulfopropyl methacrylate). This sulfonic acid polymer will capture Ca^{2+} through negatively charged terminal ends, in acidic environments, that can ionically bond to the Ca^{2+}. These polymers will be grown on carbon nanotubes. We will characterize these polymers with transmission electron microscopy (TEM) and RAMAN spectroscopy. The transport of Ca^{2+} through the polymer surfaces will be monitored by measuring the voltage change on the polymer electrode as a Calcium solution is passed over it. A device was designed to hold the polymer in a closed system to allow the solution to pass over it and out, which allows us to monitor the concentration of the calcium solution after polymer interaction.

Project Accomplishments

1. The main goal of this project was to grow 3-sulfopropyl methacrylate (SPMA) onto carbon nanotubes.

   The carbon nanotubes first needed a surface on them that would be able to be polymerized onto, the surface we used was poly dopamine. The terminal hydroxyl groups on the ends of the dopamine molecules work as a good starting point for polymerization. Next we attached 2-bromoisobutyryl bromide (BiBB) to terminal hydroxyl groups of the dopamine to act as our initiator. Finally we polymerize SPMA onto the terminal hydroxyl groups of the dopamine with atomic transfer radical polymerization (ATRP).
   Results: The polymerized carbon nanotubes (CNT-PDA-SPMA) have a terminal sulfonic acid that has a negative charge that has the potential to bind to Ca^{2+} ions.

2. The next goal was to design a device that can work as an electrode to monitor Ca^{2+} binding to the polymer surface.

   The device needed to be able to show a change in voltage as more of the sulfonic acid charges are filled with Ca^{2+}. In order to do this the device needed a reference electrode made from conductive Silver ink and the other electrode is a line of conductive Silver ink with a break in the middle where we drop cast our CNT solution to complete the circuit. Connecting these two electrodes is a microfluidic channel

made from an elastomer (PDMS). We are able to push $CaCl_2$ solutions through the channel over the electrodes and monitor the voltage with various concentrations of $CaCl_2$. We used a syringe pump to obtain a constant flow rate of solution over the electrodes. We are still working on perfecting the setup of the device but it has been used to run preliminary tests with a Calcium ionophore instead of CNT-PDA-SPMA.

3. Lastly Characterization of the CNT's in their different stages of polymerization.

   Thanks to Abdulakeem Osumah we have transmission electron microscopy (TEM) images of the CNT's, CNT-PDA, and CNT-PDA-BiBB. We will soon have images of CNT-PDA-SPMA as well. We have taken infrared spectra of the CNT's at the different stages of polymerization and they are comparable to the spectra presented in the literature.

Summary of Budget Expenditures

Supplies	**Cost**
Syringe Pump	$290.00
Autoclave Bomb	$114.00
Lab Supplies	$252.69
Biopsy Punches	$103.79
PDMS Kit	$106.65
Tubing	$107.87
Student Fellowship	$4,000
Total	$5,000.00

Conference Presentation: I presented a poster on this project at the 2018 Idaho Conference of Undergraduate Research (ICUR) in Boise and am ready to present it at this year's UIdaho Undergraduate Research Symposium.

Acknowledgement: I appreciate the generous support provided by the State Board of Education in the form of a Summer Undergraduate Research Fellowship. This was an amazing experience for me and without the support from the SBOE, I would not have been able to participate in this research.

*The information contained below is confidential, and an invention entitled, “NueroFlux Robotics” will be disclosed shortly with the Office of Technology Transfer at University of Idaho.

Final Project Report: Office of Undergraduate Research (OUR) Summer Undergraduate Research Fellowship (SURF)- Summer 2018

Fellowship Recipient: Elliott Marsden, Biological Engineering, University of Idaho

Faculty Mentor: Dr. Bryn Martin, Assistant Professor, Department of Biological Engineering

Project Title: In Vitro Magnetic Nanoparticle Drug Delivery to the Central Nervous System

Abstract:
The aim of this research was to conduct preliminary experiments demonstrating the targeted delivery of fluorescently tagged magnetic nanoparticles (F-MNP) in a 3D-printed model of the cerebrospinal fluid system. CNS diseases can be difficult to treat because of the blood brain barrier (BBB). Due to the physical size of available drug molecules, the BBB prevents or severely impedes passage of necessary drug concentration to the CNS. There many central nervous system (CNS) diseases that are difficult to treat effectively with current drug delivery methods. The advantages of CSF drug delivery could be further exploited by combining chemical targeting strategies. One of these strategies utilizes magnetic nanoparticles bound to the biologic agent and a focused magnetic field to selectively target specific regions. Visualization of the spread of the F-NMPs was visualized in a poly-carbonate tube to gather data on their movement and the influence of a magnetic field on their delivery efficiency and targeting capabilities. It was discovered that a concentrated magnetic field heavily influenced the dispersion rate of the F-NMPs, and a stationary magnet was able to collect the majority of the injected particles.

Project Accomplishments and Goals

1. **Synthesize fluorescently tagged Iron(III) Oxide Magnetic Nanoparticles**

   A fluorescently tagged nanoparticle gives the ability to collect high quality imagery showing accurate particle spread and concentration throughout the spinal model. By synthesizing nanoparticles in the lab, consistent size and geometries could be replicated and held constant over all experiments.

   Result: The IONPs were successfully synthesized in the lab and employed in multiple preliminary experiments. Due to the particles small size and concentration of particles in solution, almost all UV light was absorbed, and fluorescence was only visualized with the aid of a fluorescent microscope. Transmission Electron Microscope imaging revealed that the particles that were synthesized in the lab were indeed within 10nm of the desired 50nm diameter.

2. **To develop and construct a prototype targeting system**

   A secondary model of the CNS was developed to provide increased particle visualization and the ability to completely remove all residual particles

between experimental trials. A clear polycarbonate tube with an internal acrylic rod was used as an optimized model of the human CNS. A method for transporting the particles along the spinal model was developed using a 5-axis robotic arm in conjunction with a linear stage. This provided the most precise and constant movement of the magnet along the spinal column. It was discovered that slight variations in the robotic arm pathway had a great effect on the spread of particles to the target area. Multiple movement patterns were developed to optimize spread.

3. **Optimize particle spread and deliver high concentrations of IONPs to target area**

   Using an optimal robotic arm pathway, the particles were efficiently moved, and collected in various target areas along the spinal column. The support structures for the spinal cord proved to be an interesting case of CSF mixing, and acted as an effective barrier for particle spread. Further work will need to be done on the spinal model to prevent particle clumping around any support structures.

Summary of Budget Expenditures:

Supplies*	**Cost ($)**
Robotic Arm	1,500.00
Iron(III) Oxide Nanoparticles	311.00
Magnets (N52 Disc Magnet)	29.98
LED Light STrip	51.96
Student Fellowship	4,000
TOTAL	**5,000**
***$1,000 from SURF award, remaining covered my mentor**	

Conference Presentation: I will be presenting a poster of my work at the UI Undergraduate Research symposium in the Spring of 2019. I have also participated and presented my work at the Idaho Conference on Undergraduate Research in July of 2018.

Acknowledgement: I truly appreciate the generous support provided by the State Board of Education in the form of the Summer Undergraduate Research Fellowship. This was a tremendous learning experience for me. Without the support from the SBoE, I would not have been able to participate in this summer research project.

Final Project Report: Office of Undergraduate Research (OUR) Summer undergraduate research fellowship (SURF) – Summer 2018

Recipient: Jessica Nicholson, Biology, University of Idaho

Mentor: Dr. Onesmo Balemba, Biological Sciences, University of Idaho

Project Title: Why your gut may be working against you: gut derived molecules cause dysmotility and neuropathy in high fat fed mice

Abstract:

Type 2 diabetes (T2D) is a prevalent disease in the United States, affecting 21.9 million people. Patients often suffer from gastrointestinal (GI) issues like stomach cramps and constipation. This is caused by a reduction in inhibitory motor neurons in the intestinal tract. Recent studies have shown the development of gastrointestinal dysmotility and neuropathy before the onset of T2D, and ileocecal supernatants from high fat (HF) fed mice caused dysmotility and neuropathy ex vivo. However, the specific cause of dysmotility and neuropathy are still not known. We hypothesized that fractions from HF ileocecal supernatants would cause dysmotility and neuropathy. High Performance Liquid Chromatography (HPLC) was used to separate supernatants into aqueous (water) and methanolic fractions which were tested on mice intestinal muscularis tissue. Contractions of the tissue samples were counted, and immunohistochemistry and imaging used to determine if these fractions caused neuropathy. Water fractions from HF mice caused a significant decrease in muscularis contractions after 24 hours; water fractions of standard chow fed (SC) mice and methanolic fractions of HF and SC mice did not significantly induce dysmotility. It was also found that HF water fractions caused a reduction in neuronal nitric oxide synthase (nNOS) staining, indicating that the inhibitory motor neurons were damaged. These results suggest a molecule(s) in the HF water fractions are causing dysmotility and neuropathy. Sub-fractionation and chemical analysis of these fractions will narrow down on gut derived molecules that may be causing these symptoms; and lead to treatment options before the start of T2D.

Project goals and accomplishments:

1. Test the effects of the fractions on longitudinal muscle myenteric plexus contractions at 0, 24, and 48 hours

I was able to culture my preparations in each fraction, along with a control, and record videos of the contraction of the tissue samples at all time points. I recorded the number of contractions for analysis and was able to determine that the HF water fractions were causing a significant decrease in muscular contractions, telling us that they may be causing dysmotility.

2. Determine what fractions, if any, cause neuropathy; specifically, a reduction in inhibitory motor (nNOS) neurons.

After staining the samples mentioned above and analyzing the images and data, we determined that the HF water fractions caused a significant reduction in nNOS staining, as

well as lowering the overall percentage of nNOS neurons. This shows that the HF water fraction may be causing neuropathy and a decrease in inhibitory motor neurons.

3. Identify molecules that may be causing dysmotility and neuropathy in mice fed a HF diet

This was the first step towards accomplishing this overall goal. We have successfully narrowed down on the fractions causing these symptoms, although further research must be done to identify certain culprits.

Result:
These data suggest that molecules present in the supernatant of high fat fed mice ileocecal content causes dysmotility and neuropathy in mice.

Summary of budget expenditures:

Supplies	Cost
Sigma Aldrich purchase	$263.48
Sigma Aldrich purchase	$161.07
Sigma Aldrich purchase	$84.38
Sigma Aldrich purchase	$401.10
Sigma Aldrich purchase	$41.45
Poster	$48.30
Subtotal supplies	$999.78
Stipend	$4,000
Total	**$4,999.78**

Presentation of work:
This project was presented at the Idaho Conference of Undergraduate Research at Boise State University in July 2018. Also, I will be presenting at the UI Undergraduate Research Symposium in April 2019.

Funding acknowledgement:
I truly appreciate the generous support provided by the State Board of Education in the form of a Summer Undergraduate Research fellowship. This was a tremendous experience for me. Without support from the SBOE I would not have been able to participate in this research, thank you!

Final Project Report: Office of Undergraduate Research (OUR), Summer Undergraduate Research Fellowship – Summer 20118

Fellowship Recipient: Joelle Stephens

Faculty Mentor: Dr. Ann F. Brown, Dept. Movement Sciences, University of Idaho

Project Title: Body Image, Body Composition & Energy Intake of Adolescent Aesthetic Athletes

Background: Adolescent athletes in aesthetic sports such as gymnastics and dance are often evaluated based on appearance and weight. Many of these athletes' experience heightened attention on appearance and it is common to observe unhealthy behaviors in attempt to achieve a particular physique. Purpose: The purpose of this study was to assess adolescent aesthetic athletes' body image, body composition and energy intake. Methods: Gymnasts and dancers (n=24; age 10.54±2.99) completed questionnaires regarding medical history, body image perception and food consumption. Additionally, body composition was assessed using a dual energy x-ray absorptiometer (DXA). Results: 92% (n=22) of the participants felt pretty and were happy with the way their body looked. When asked about being perfect, 79% (n=19) of the participants "didn't worry about it" while 17% (n=4) of the participants put "a lot of pressure on themselves to be perfect". Only 4% (n=1) reported feeling "bad about themselves" whereas 46% (n=11) felt "good about themselves". Body composition results showed healthy weight (37.86 ± 14.02kg), height (55.78 ±6.23in), lean mass (27.04 ±9.57kg), and bone mineral density (BMD) (0 .771 ±0.19). Total dietary intake averaged 1,984±538.7 calories, 86.70 ±11.92g/d protein,
286.60 ±53.55g/d carbohydrate and 995.65 ±414.19mg/d calcium. Conclusion: Most participants had high self-esteem and body image perception. Three gymnasts recorded at risk for low BMD and one gymnast recorded low BMD for their chronological age. Calcium was recorded below the recommended daily value (1000mg/d), while the macronutrients were above the recommended daily value (19-46g/d protein and 130g/d carbohydrates.

Project Description

Aesthetic sports are considered weight-sensitive since the artistic movements that occur during performance are most optimal when the athlete is lean and graceful (6). Aesthetic athletes become aware of the emphasis placed on achieving a lean physique at a young age often beginning as early as 3 years old (24). It has been previously established that peak performance occurs well before puberty in aesthetic sports and excess fat mass (FM) is seen as a disadvantage (33). Therefore, these athletes are subjected to heightened risk for body image dissatisfaction and eating disorders at a much earlier age than other non-aesthetic sports (9, 10, 33).

Since many aesthetic athletes are concerned about appearance, they often consume a low energy diet to maintain a lean physique (9, 34). Low energy intake can place athletes at risk for inadequate nutrient consumption resulting in inadequate recovery, fatigue, and loss of lean body mass (LBM) (34). In addition, low energy intake is often combined with heavy training loads which places aesthetic athletes at a higher risk for injury, stress, and immune system problems (34). If aesthetic athletes chronically diet, it

can impair overall health and physical function, while also causing more serious medical complications that involve the cardiovascular, endocrine, gastrointestinal, and central nervous systems (34). Additionally, delayed menarche, bone growth retardation, reduced height, weight, and FM, and increased rate of injuries can occur at an early age because of inadequate energy intake and heavy training loads in adolescent aesthetic athletes (17, 23, 31, 34).

Gymnasts have been reported to perform exercise training at higher intensities when compared to dancers which may be related to a greater chance of growth stagnation, slowed development of secondary characteristics, and delayed menstrual cycle onset (21). Although gymnasts and dancers have similar overall energy intake, as well as body image dissatisfaction and eating disorder concerns, gymnasts often have a greater overall bone mineral density (BMD) than dancers (10, 21). This may be due to gymnasts performing higher-load activity on the upper and lower body, while dancers lack the weight bearing activity in the upper body. As a result, dancers are often reported as having lower total BMD when compared to gymnasts (8, 21). Low BMD is related to factors such as energy intake and weight bearing activity, both of which increase the risk for injuries and future health problems.

Previous research has used a variety of methods to assess body image dissatisfaction, body composition, energy intake and eating disorders among aesthetic athletes (5, 7, 9, 22, 34). Understanding the relationship between body image dissatisfaction, body composition, and energy intake in adolescent aesthetic athletes can help to prevent and reduce the prevalence of eating disorders and medical complications often observed in this population. Gaps in the current literature stress the need to continue to explore possible explanations for body image dissatisfaction, eating disorders, and injury occurrence in adolescent gymnasts and dancers (1, 7, 9). Therefore, this project will investigate body image, body composition, and energy intake in an adolescent aesthetic athlete population. The project's overall objective is to evaluate the differences between early aged gymnasts and dancers' body image perception, body composition, specifically BMD and LBM, and energy intake in order to identify and develop methodology to improve overall health and performance in the future.

Accomplishments

The initial plan for the research project was to recruit fifteen gymnasts and fifteen dancers to participate to compare and contrast their body image, body composition, and energy intake. Although we are still in the process of recruiting the rest of the participants, it has been much easier to recruit the gymnasts than the dancers. As of now, 18 gymnasts have participated and only 6 dancers. The remaining 6 participants that we recruit will be dancers with the hope that we are better able to find similarities and differences in the two aesthetic athlete populations.

Though some of the participants were as young as five, all of the participants were able to complete the DXA scan with no issues. In addition, if the participant was too young to be able to read the body image/self-esteem questions, the researcher would read the questions aloud to the participant so they could choose the best option for themselves. In the end, every participant completed the DXA scan and was able to answer all of the questions to the body image/self-esteem questions, providing us with enough data to analyze and come up with results and conclusions.

Budget Expenditures

Dual-Energy X-Ray Absorptimetry (DEXA) Scans: in order to assess bone mineral density in dancers and gymnasts DEXA scans will be conducted in the HPL. Scan cost is $5.80/participant and contributes towards maintenance of the equipment. 30 participants x $5.80 =$175	$175
Participation Compensation: incentive to participate, compensation for travel to HPL and time invested in the study. 30 participants x $25 = $750	$750
Poster Printing For presentation at the Undergraduate Research Symposium	$75
Student Stipend	$4,000
Total	$5,000

Since we still have six participants coming into the lab later this month, there is $34.80 that has not yet been spent for DXA scans and $150 dollars that has not been given out to the participants for participation compensation. In addition, since this research project was not presented at the ICUR due to not having enough data recorded yet, the $75 for the poster printing will be spent by the end of this month when the poster is printed. By August 31st, all $1,000 in project funding will be spent. Results will be presented at the UI Undergraduate Research Symposium in April, 2019.

Acknowledgment: This work was made possible by generous support from the Idaho State Board of Education which provided the funding for this Undergraduate Research Grant from the Office of Undergraduate Research. I benefited greatly from this experience and I sincerely thank the SBOE and UI's Office of Undergraduate Research for making this possible.

Final Project Report: Office of Undergraduate Research (OUR) Summer Undergraduate Research Fellowship (SURF) – Summer 2018

Fellowship Recipient: McKenzie Walquist, Biological Engineering, University of Idaho

Faculty Mentor: Sarah Wu, PhD. Assistant Professor, Biological Engineering

Project Title: Non-thermal Liquid Plasma Treatment for Antibiotic Removal in Aqueous Solution

Abstract: Traditional wastewater treatment processes are not able to degrade pharmaceuticals which find their way into the water system; one solution currently being explored to prevent these emerging contaminants from being released into the environment is advanced oxidation processes (AOPs), including non-thermal liquid plasma (NTLP) treatment. The NTLP process produces high energy mobile electrons and oxidizing radicals which degrade large organic molecules. In this proposed project, a novel reactor design will be used which includes a circulating treatment and discharge occurring in the liquid phase to remove three types of beta-lactam penicillins. The conclusion of this study will give results of the amount of degradation achieved, the effects of different reactor parameters on removal rates and efficiency, energy yield (mass removed per kWh), and the influence of -OH and H2O2 radicals on removal. Finally, this new reactor design can be compared to other non-thermal plasma reactors' results in order to make suggestions for its applicability in industry.

Project Accomplishments:

Objective 1: Treated solution physical properties

The H_2O_2 and COD concentrations are indicators for the chemical processes occurring during treatment. If Chemical Oxygen Demand of the samples decreased during treatment with the NTLP reactor for all three antibiotics, this would suggest that the molecules were oxidized and degraded. A hydrogen peroxide concentration increase would assist in oxidizing these compounds. A 1-hour treatment of tap water was analyzed for the hydrogen peroxide generation.

> Result: The COD levels of ampicillin and amoxicillin decreased by 18% and 17% respectively. Oxacillin decreased less than 10%. This lower change may indicate that there is a larger organic part left over after degradation. H_2O_2 concentrations consistently increased during treatment reaching around 200ppm after 1 hour, which would provide additional oxidizing potential of this treatment. pH also increased after treatment, which means there is a higher [-OH] concentration. The exact antibiotic concentrations were not able to be calculated with the proposed spectrophotometric method, but further tests will be conducted to find these removal values.

Objective 2: Effect of reactor parameters

Parameters of the reactor such as liquid flow rate, applied power, air flow rate, and starting concentrations were tested to find the most efficient operating conditions for the reactor.

> Result: In all experiments, applied power increases degradation of organic molecules. The highest energy yield, which was calculated as mass removed per kWhr, was around 300 Watts. Conversely, the lower the flow rate, the better the discharge was able to treat the solution.

Objective 3: Effect of $FeCl_2$ as a catalyst
Addition of $FeCl_2$ into a NTLP treatment has been shown to increase the production of hydroxyl, a powerful oxidizer.

Result: No consistent trend was obtained from using $FeCl_2$ as a catalyst in production of oxidizing radicals at 10 mg/L concentration.

Budget Expenditures:

Supplies	Cost
Chemical reagents and antibiotics	$89.84
Ampicillin (5g)	$35.01
Oxacillin sodium salt (2g)	$28.28
Amoxicillin trihydrate (5g)	$24.07
Passive high voltage probe	$827.80
Student Fellowship	$4,000
Total	**$5,005**

Conference Presentation: This research was presented at the poster presentation session during the Idaho Conference on Undergraduate Research (ICUR) in Boise, ID, July 25-26, 2018.

Acknowledgement: I truly appreciate the generous support provided by the State Board of Education in the form of a Summer Undergraduate Research Fellowship. This was a tremendous experience for me. Without this support from the SBOE, I would not have been

MECHANISTIC ANALYSIS OF BOROHYDRIDE THERMOLYSIS

Mason Anderson, Dr. Mark Roll: University of Idaho Chemical and Materials Engineering Department

Introduction

- Borohydride clusters are synthesized with reactive/toxic neutral borane compounds such as diborane
- Oligomerization into larger clusters is dictated by heat and cluster concentration
- Little research has been done towards the synthesis of borohydride clusters utilizing shelf-stable $NaBH_4$
- Borohydride clusters show novel nano-building block characteristics, extensive electrochemical functionality of the closo-ionic borohydride clusters ($B_{12}H_{12}^{2-}$)

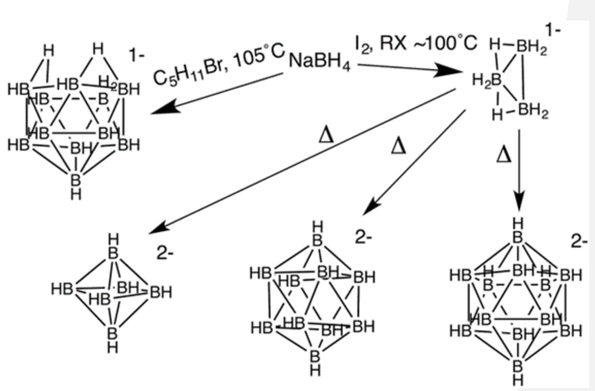

Cluster Synthesis Map

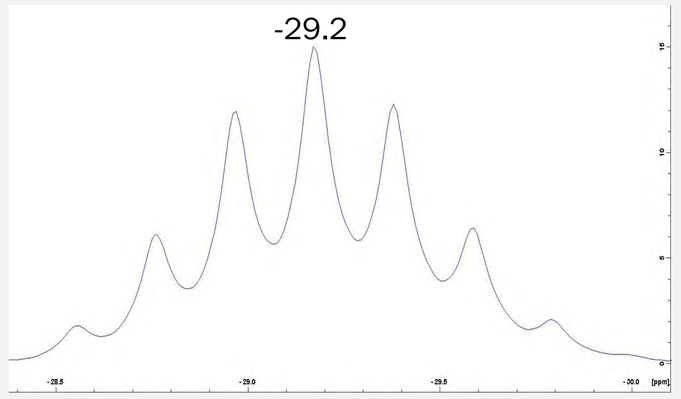

B^{11} NMR of $B_3H_8^-$ Product

Borohydride Clusters

- Incorporation of icosahedral borohydride clusters and closo-carboranes into refractory thin-films exhibit high temperature and radiation resistance
- Reaction solvent is critical for the dissolution of $NaBH_4$ and in-situ capture of BH_3
- The ability to selectively synthesize the $B_3H_8^-$ anion is crucial for non-toxic synthesis, but current work does not propagate beyond laboratory scale

Acknowledgments

- University of Idaho Summer Undergraduate Research Fellowship
- University of Idaho Department of Chemical and Materials Engineering

Results

Kinetics

- Reactant concentration and addition rate are critical factors
- Rapid addition can deplete local BH_4^- concentration, leading to side products
- Rate of reaction is extremely different, even for similar reactants

Solvent Decomposition

- Results show decomposition of diglyme in as little as 3hrs at 95°C during reaction
- THP (tetrahydropyran) shows no decomposition after 24hrs during reaction at reflux (88°C)
- THP does not dissolve BH_4^- well and causes drastically different product observation

Reactant	Solvent	Reactant Concentration (M)	Time (hr)	Temperature (°C)	Results
Iodine	Diglyme	1.8	2	95	$B_3H_8^-$ cluster selective
	Diglyme	Solid	Rapid	95	Higher clusters, heavy side-products evident
	THP	Solid	Rapid	88	Higher clusters, few side products
Methyl Iodide	Diglyme	Neat	3-70	RT	No clusters formed, photodissociation of MeI
Pentyl Bromide	Diglyme	Neat	2	95	No $B_3H_8^-$ formation, excess formation of $B_2H_7^-$
	Diglyme	1.8	2	95	Small $B_3H_8^-$ formation
Copper (I) Chloride	Diglyme	Solid	Rapid	100	$B_3H_8^-$ formation, difficult workup due to metal deposition
	THP	Solid	Rapid	85	Higher borane clusters, no $B_3H_8^-$ formation
Copper (II) Sulfate	Water	Solid	1	95	Reduced metal deposition, no clusters, only borate product

Conclusions

- $B_3H_8^-$ can be synthesized in good yields from non-toxic precursory materials
- Kinetic issues need to be addressed
- Investigation into a new solvent with high BH_4^- solubility and low reactant solubility
- Better understanding of B^{11} NMR identification is needed for intermediate products

Modulation of the Retinal Immune Environment in a Zebrafish System of Rod Photoreceptor-Specific Degeneration

Zachary Blume and Diana Mitchell
Department of Biological Sciences, University of Idaho, Moscow, ID

Abstract

Activated and pro-inflammatory microglia, along with accompanying local inflammation, are associated with human retinal degenerative disease. However, it remains unclear if these aspects of the immune response are symptomatic or directly initiate and/or contribute to disease pathology, such as the death of additional retinal neurons. One hypothesis for continued loss of neurons in retinal degenerative disease is that microglia may engulf, or possibly initiate cell death of, otherwise healthy neurons (1,2).

Our project attempts to test this hypothesis using a zebrafish system in which rod photoreceptors die due to a toxic transgene (XOPS:mCFP), but cone photoreceptors survive (3). We first characterized microglial characteristics in XOPS:mCFP retinas compared to wildtype and found that microglia localize to the photoreceptor layer and engulf dying rods, but total numbers of microglia are similar. Next, we successfully induced a pro-inflammatory retinal immune environment by intraocular injection of zymosan (a pro-inflammatory compound) (4), as indicated by our results showing infiltration and accumulation of immune cells in the retina and gene expression of selected transcripts.

Our next goal is to determine if this induction of a pro-inflammatory retinal environment may result in subsequent cone death or disappearance in XOPS:mCFP retinas, thus directly probing contributions of a dysregulated immune environment to retinal degenerative disease.

Figure 1: Perpetual Rod Death and Regeneration in XOPS:mCFP Zebrafish Retinas

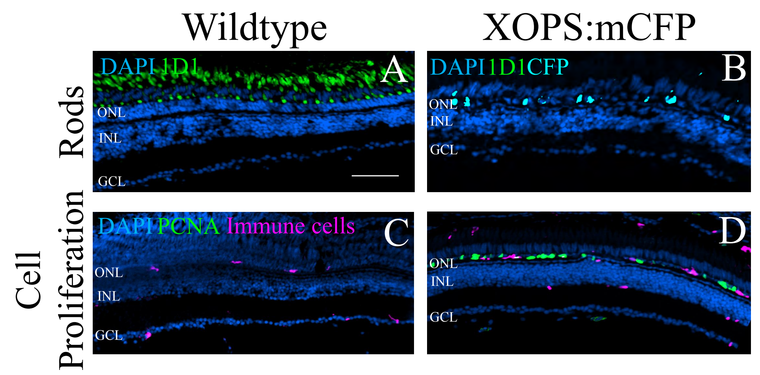

Images show a 5µm section of zebrafish retina from wildtype and XOPS:mCFP transgenic fish. Wildtype retinas (A,C) show healthy rods (A, labeled by 1D1) and lack of cell proliferation in the outer nuclear layer (ONL) (C, labeled by PCNA). XOPS:mCFP retinas (B,D) show far fewer rod photoceptors (B, labeled by CFP). 1D1 is not observed in XOPS:mCFP retinas because they do not express the protein rhodopsin (3), which is the 1D1 antibody target. We also observe a constant attempt to regenerate dying rods by proliferative rod precursors (D, labeled by PCNA). In XOPS:mCFP retinas, we also see that microglia localize to the ONL (similar to C) around the PCNA+ cells, but do not express PCNA themselves (D). This tells us that immune cells are not dividing in response to ongoing rod death, but instead the PCNA+ cells likely represent only rod precursors. Scale bar = 50µm and applies to all images. INL = inner nuclear layer, GCL = ganglion cell layer, PCNA = proliferating cell nuclear antigen.

Methods: Modulation of the Retinal Immune Environment

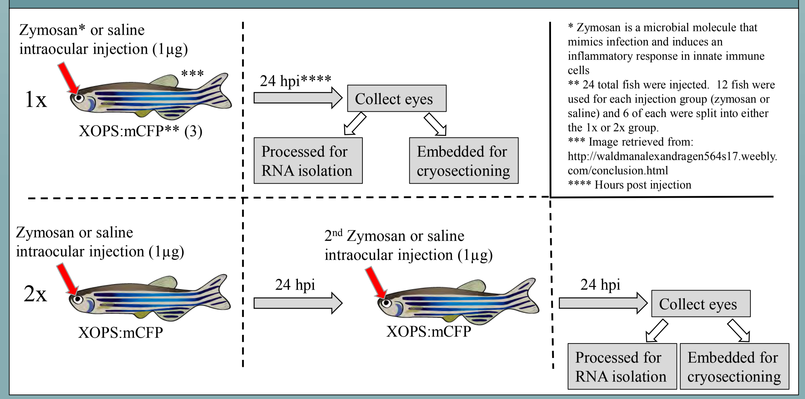

Figure 2: Zymosan Treated Retinas Show Infiltrating Immune Cell Response

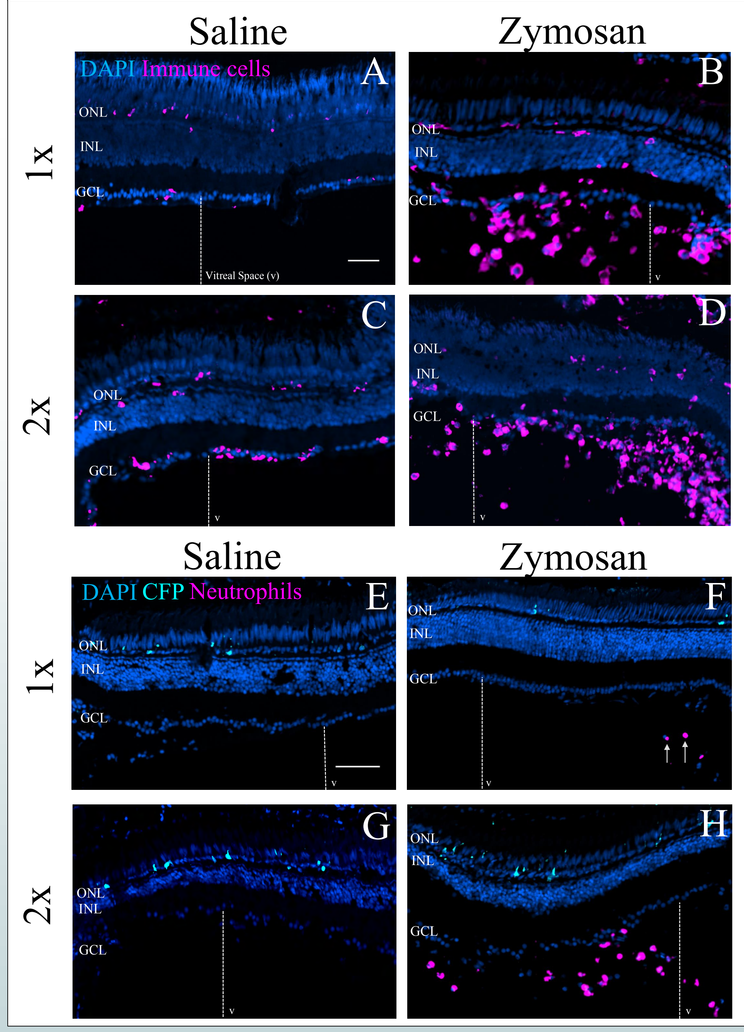

Images show 5µm section of XOPS:mCFP retinas with 1x and 2x zymosan or saline (control) injections stained for L-plastin (immune cells, A-D) and MPX (neutrophils, E-H). After 1 injection of zymosan, immune cells infiltrate the retina which is shown by an accumulation of immune cells in the vitreal space (B) and redistribution of immune cells towards the GCL and vitreal interface. After 2 injections of zymosan, the immune cell population continued to increase (D). The immune cells that accumulate following zymosan injection include neutrophils, which is a characteristic of a pro-inflammatory response (arrows, F and H). However, the recruited neutrophils do not account for the entirety of the infiltrating immune cell population.

Scale bar = 50µm, A applies to B,C, and D. Scale bar in E applies to F,G, and H.

Figure 3: Increase in Pro-Inflammatory Gene Expression Following Zymosan Injection

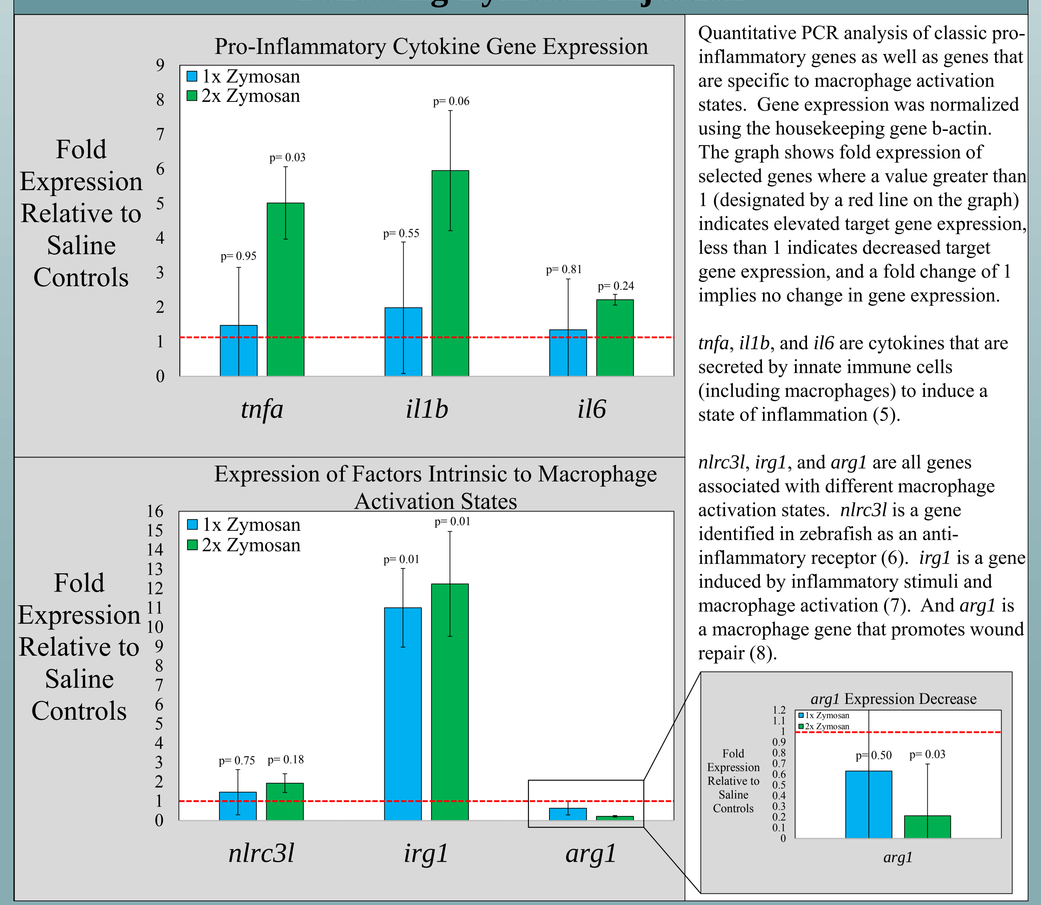

Quantitative PCR analysis of classic pro-inflammatory genes as well as genes that are specific to macrophage activation states. Gene expression was normalized using the housekeeping gene b-actin. The graph shows fold expression of selected genes where a value greater than 1 (designated by a red line on the graph) indicates elevated target gene expression, less than 1 indicates decreased target gene expression, and a fold change of 1 implies no change in gene expression.

tnfa, *il1b*, and *il6* are cytokines that are secreted by innate immune cells (including macrophages) to induce a state of inflammation (5).

nlrc3l, *irg1*, and *arg1* are all genes associated with different macrophage activation states. *nlrc3l* is a gene identified in zebrafish as an anti-inflammatory receptor (6). *irg1* is a gene induced by inflammatory stimuli and macrophage activation (7). And *arg1* is a macrophage gene that promotes wound repair (8).

Figure 4: Cell Death 24 and 48 Hours Following Pro-Inflammatory Induced State

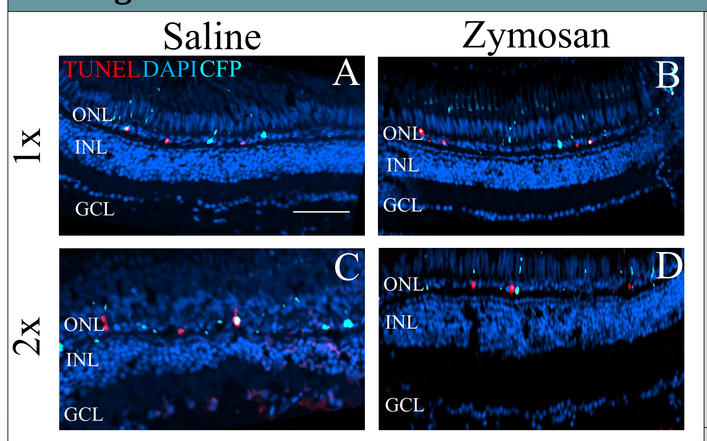

Here, we quantified cell death following injection of zymosan. We used a TUNEL* stain to mark cells that were in late stage apoptosis. TUNEL+ cells were quantified in the ONL exclusively and TUNEL+ cells that were CFP+ rods were accounted for as their death is programmed by the transgenic line. We found that the 1x and 2x zymosan injection groups showed an increase in cell death per 100µm of retina in relation to their corresponding saline control (E, although not statistically significant). Additionally, this increased number of TUNEL+ cells did not represent CFP+ rods (F). This could be evidence for increased cell death in a population other than rods following an inflammatory response.
Scale bar = 50µm and applies to all images.

**Terminal deoxynucleotidyl transferase dUTP nick end labeling*

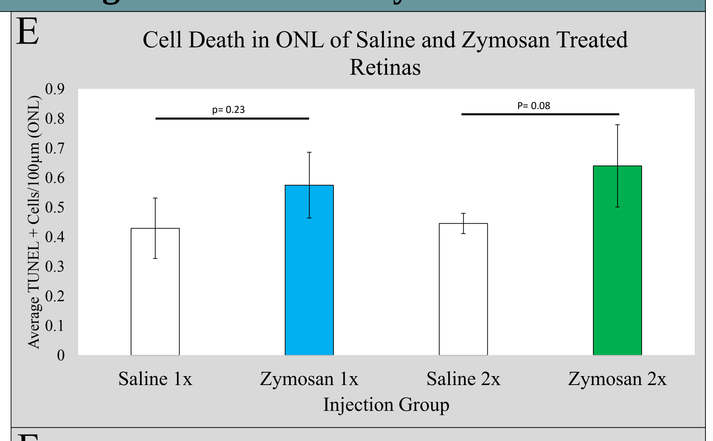

Figure 5: Cell Proliferation 24 and 48 Hours Following Pro-Inflammatory Induced State

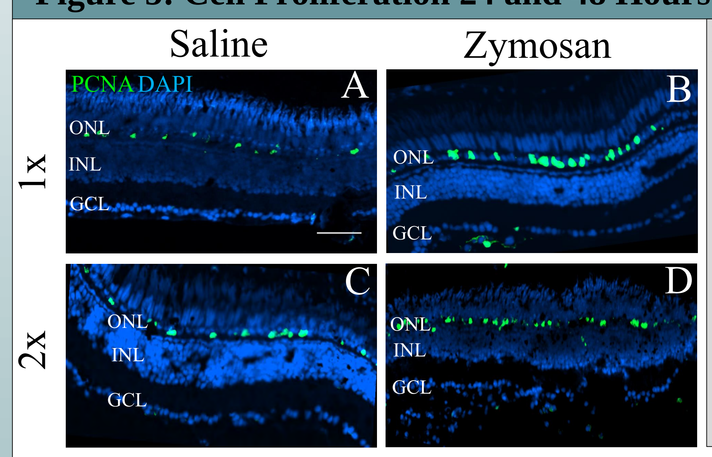

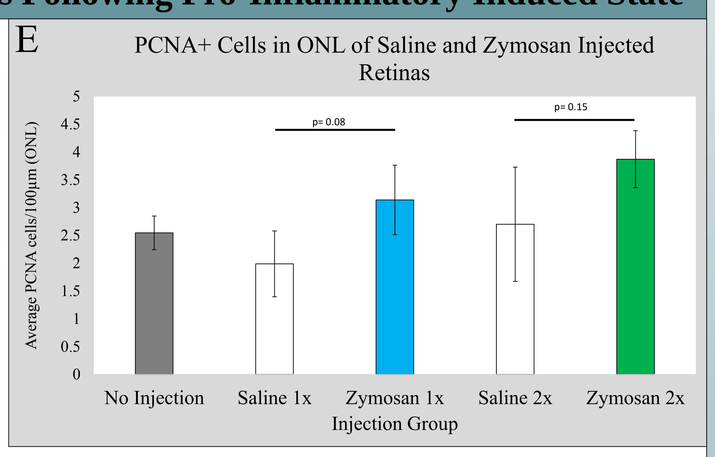

Images show 5µm section of XOPS:mCFP retinas with 1x and 2x zymosan or saline (control) injections stained for PCNA to indicate cell proliferation. PCNA+ cells were quantified in the ONL exclusively. We found that the1x and 2x zymosan injection groups had more PCNA+ cells per 100µm of retina when compared to their corresponding saline control (E). XOPS:mCFP eyes that did not receive an injection were also quantified as a control. We found that the zymosan treated eyes had an increased number of PCNA+ cells when compared to eyes receiving no injection, but was not statistically significant (p= 0.70, 1x) (p= 0.18, 2x). Both groups of saline injected controls showed no significant change when compared to eyes receiving no injection (p= 0.03, 1x) (p= 0.38, 2x). We observed that only rarely were L-plastin+ cells also PCNA+ (not shown) indicating that immune cells in the ONL did not represent significant numbers of the PCNA+ cells quantified. Scale bar = 50µm and applies to all images.

Conclusions and Future Directions

- We have shown that we can induce an inflammatory response in the zebrafish retina by using the microbial compound zymosan to mimic infection. Resident and infiltrating immune cells mount an inflammatory response as early as 24 hpi and continue to infiltrate up to 48 hpi. Along with infiltrating immune cells characteristic of an inflammatory response, we observed an increase in gene expression for target genes that are indicative of a pro-inflammatory state of macrophage activation.
- In 1x and 2x zymosan injected XOPS:mCFP retinas, TUNEL+ and PCNA+ cells were slightly more numerous than in saline injected controls (although differences were not statistically significant). Also, less cell death appeared to be attributed to CFP+ rods in the zymosan injected retinas.
- The future of this project will be to determine if sustained inflammation (for longer periods) in the retinal microenvironment may result in subsequent cone death, other other signs of pathology, in XOPS:mCFP retinas, more akin to simulating a chronic degenerative disease. Moving forward we hope to directly probe the contributions of a dysregulated immune environment to retinal degenerative disease.

Acknowledgements

Funding: The research for this project was supported by a University of Idaho Summer Undergraduate Research Fellowship made possible by a 2017-2018 Undergraduate Research Grant from the Higher Education Research Council/Idaho State Board of Education and Mitchell lab start-up funds from The University of Idaho.
I would like to thank all members of the Mitchell and Stenkamp lab for their technical assistance, discussion, and guidance; Ann Norton, IBEST OIC; Dr. Ann Morris (University of Kentucky) for providing the XOPS:mCFP zebrafish line; Dr. Michael Redd (University of Utah) for providing the L-plastin antibody; and Dr. James Fadool (Florida State University) for providing the 1D1 antibody.

References

1. Narayan DS, Wood JP, Chidlow G, Casson RJ. A review of the mechanisms of cone degeneration in retinitis pigmentosa. Acta Ophthalmol. 2016; 94: 748-754. doi:10.1111/aos.13141
2. Wong WT, Zhao L, Zabel MK, Wang X, et al. Microglial phagocytosis of living photoreceptors contributes to inherited retinal degeneration. EMBO Molecular Medicine. 2015; 7(9): 1179-1197. doi:10.15252.emmm.201505298.
3. Morris A, Schroeter HE, Bilotta J, Wong ROL, Fadool JM. Cone Survival Despite Rod Degeneration in XOPS-mCFP Transgenic Zebrafish. Invest. Ophthalmol. Vis. Sci., 2005; 46(12): 4762-4771. doi: 10.1167/iovs.05-0797
4. Brand M, Kyritsis N, Kizil C, et al. Acute inflammation initiates the regenerative response in the adult zebrafish brain. Science. 2012; 338(6112): 1353-1356. doi:10.1126/science.1228773
5. Parham P. The immune system (fourth edition). 2015. The immune system (fourth edition). New York (NY): Garland Science.
6. Shiau CE, Monk KR, Joo W, Talbot WS. An anti-inflammatory NOD-like receptor is required for microglia development. Cell Reports. 2013; 5(5):10.1016/j.celrep.2013.11.004. doi:10.1016/j.celrep.2013.11.004.
7. Basler T, Jeckstadt S, Valentin-Weigand P, Goethe R. Mycobacterium paratuberculosis, Mycobacterium smegmatis, and lipopolysaccharide induce different transcriptional and post-transcriptional regulation of the IRG1 gene in murine macrophages. Journal of Leukocyte Biology. 2006; 79(3): 628-638. doi: 10.1189/jlb.0905520
8. Pesce JT, Ramalingam TR, Mentink-Kane MM, Wilson MS, El Kasmi KC, et al. (2009) Arginase-1-expressing macrophages suppress Th2 cytokine-driven inflammation and fibrosis. PLOS Pathogens 5(4): e1000371. https://doi.org/10.1371/journal.ppat.1000371

Computing Fourier Coefficients of Siegel Modular Forms

Beau Horenberger

Fourier Expansions

Fourier expansions are a method of writing a periodic function, s(x), as a sum of other, simpler functions: sin and cosine waves. One way to write this representation is

$$f(x)=\sum_{n=0}^{\infty}A_n\cos\left(\frac{n\pi x}{L}\right)+\sum_{n=1}^{\infty}B_n\sin\left(\frac{n\pi x}{L}\right)$$

Though this can be condensed as

$$f(x)=\sum_{n=1}^{\infty}c_n e^{i\frac{2\pi nx}{P}}$$

The following is a set of approximations using the first k terms of a Fourier expansion:

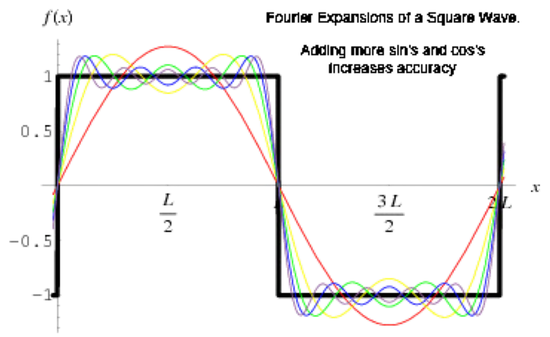

Fourier expansions are a valuable method for analyzing the behavior of functions. The coefficients c_n are determined via

$$c_n=\frac{1}{P}\int_{x_0}^{x_0+P}s(x)\cdot e^{-i\frac{2\pi nx}{P}}\,dx,$$

Where s(x) is the original function. These coefficients contain information about the original function and are relevant in the analysis of modular and Siegel modular forms.

What Are Modular Forms?

Modular forms are complex-valued forms with a kind of periodicity, because of which they can be approximated via Fourier series or polynomials.
Traditional periodicity is illustrated below:

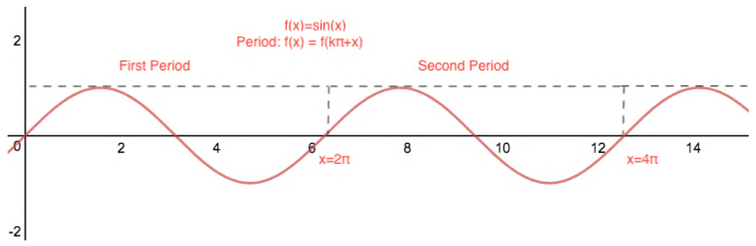

Rather than a period P and the relation *f*(x)=*f*(kP+x), a modular form of weight k has the following relation:

$f\left(\frac{az+b}{cz+d}\right)=(cz+d)^k f(z)$ for all matrices $\det\begin{pmatrix}a & b\\ c & d\end{pmatrix}=1$

With *a,b,c,d* being integers.

Notice that if we have the matrix $\begin{pmatrix}1 & 1\\ 0 & 1\end{pmatrix}$, our equation becomes

$$f(z+1)=f(z)$$

And if we have the matrix $\begin{pmatrix}0 & 1\\ -1 & 0\end{pmatrix}$, it becomes

$$f\left(\frac{-1}{z}\right)=z^k f(z)$$

In fact, these two matrices are sufficient to generate all matrices of determinant 1 and describe the underlying actions at work in the set of matrices.
The theory of modular forms has been relevant in many Number Theory proofs as well as in the theory of elliptic curves. An example is Jacobi's 4-Square Theorem, which describes the number of ways an integer can be written as the sum of four squares:

$$\left(\sum_{n=-\infty}^{\infty}q^{n^2}\right)^4=\sum_{a,b,c,d\in\mathbf{Z}}q^{a^2+b^2+c^2+d^2}=1+8\sum_{m=1}^{\infty}\sum_{\substack{d\mid m\\ 4\nmid d}}dq^m.$$

Binary Quadratic Forms

Binary quadratic forms with discriminant *N* are expressions of the form

$$f(x,y)=ax^2+bxy+cy^2, where\ b^2-4ac=N$$

Two binary quadratic forms, *f(x,y)* and *g(x,y),* are properly equivalent if there exists a transformation $\begin{pmatrix}a & b\\ c & d\end{pmatrix}$ with determinant 1 such that

$$f(ax+by,cx+dy)=g(x,y)$$

This means properly equivalent binary quadratic forms represent the same values.
Binary quadratic forms of negative discriminant *N* are always equivalent to exactly one reduced form, where

$$b\le a\le c, where\ b\ge 0\ if\ |b|=a$$

And a similar circumstance applies to positive discriminants.
There are a finite number of reduced forms, and thus, it can be shown that binary quadratic forms of a discriminant *N* can be broken into a finite number of equivalence classes.
The set of reduced forms can be used to reach all other forms via transformation, and thus are valuable for representation purposes. We consider this the "fundamental domain" of binary quadratic forms. The fundamental domain for transformations of the form $\begin{pmatrix}a & b\\ c & d\end{pmatrix}$ with $\det\begin{pmatrix}a & b\\ c & d\end{pmatrix}=1$ is shown here to give a visual representation of the concept.

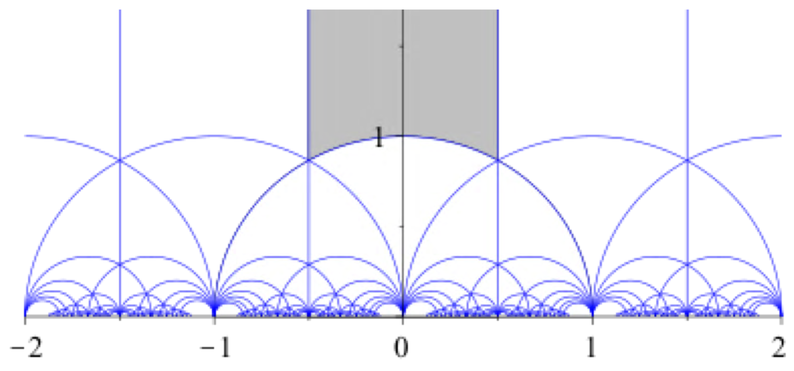

Siegel Modular Forms

Siegel modular forms are similar to modular forms, but instead use complex matrices. Siegel modular forms have a level, *N,* weight, ρ, and degree (or genus), g.
They can be generated through the use of a series, such as the Eisentein series.
As an example, we consider the Siegel modular form of weight 24, level 4, and degree 1 which has an explicit formula:

$$78*A^2*B*C-67*A^3*D-274492800*A*C^2+25*B^2*D+71539200*D^2$$

Where $\begin{pmatrix}A & B\\ C & D\end{pmatrix}$ is in $\Gamma_g(N)$, the symplectic group of level *N*, defined as

$$\Gamma_g(N)=\left\{\gamma\in GL_{2g}(\mathbb{Z})\mid \gamma^{\mathrm{T}}\begin{pmatrix}0 & I_g\\ -I_g & 0\end{pmatrix}\gamma=\begin{pmatrix}0 & I_g\\ -I_g & 0\end{pmatrix},\ \gamma\equiv I_{2g}\mod N\right\}$$

Sample coefficients of the Fourier expansion include: -576, -72864, and -722304
One kind of modular form, the Siegel paramodular form, uses only an arithmetic subgroup of the symplectic group. These Siegel paramodular forms have a Fourier expansion:

$$f(Z)=\sum_{T\epsilon A(N)^+}a(T)e^{2\pi itr(TZ)}$$

However, notice the index set of the sum is not in the integers. Instead, they are binary quadratic forms *S* such that:

$$S=\begin{bmatrix}\alpha & \beta\\ \beta & \gamma\end{bmatrix},\quad \alpha\in N\mathbb{Z},\quad \gamma\in\mathbb{Z},\quad \beta\in\frac{1}{2}\mathbb{Z},\quad \alpha>0,\quad \det\begin{bmatrix}\alpha & \beta\\ \beta & \gamma\end{bmatrix}=\alpha\gamma-\beta^2>0$$

This is a matrix representation of the binary quadratic forms $\alpha x^2+2\beta xy+\gamma y^2$ meeting the described conditions.
Thus, analyzing the Siegel paramodular form's Fourier coefficients requires an understanding of binary quadratic forms and the values they can represent

Computing New Siegel Modular Forms

It has been proven that given a Siegel paramodular form (particularly a Siegel cusp form of paramodular level *N*, weight *k*, and degree 2) can be twisted to create a new Siegel modular form of level Np^4 with a Fourier expansion:

$$\mathcal{T}_\chi(f)(Z)=\sum_{T\epsilon A(N)^+}W(\chi)a_\chi(T)e^{2\pi itr(TZ)}$$

Where $W(\chi)$ and $\alpha_\chi(T)$ are described in *Fourier Coefficients For Twists Of Siegel Paramodular Forms (Expanded Version)* , and χ is the Dirichlet character mod *p*.
The definition of $W(\chi)$ and $\alpha_\chi(T)$ involves many computations with binary quadratic forms, necessitating theory of binary quadratic forms for analysis of the Fourier coefficients, such as what values they can represent.

Goals of Research

The goal of this research is to create a code base which can compute equivalence classes and properties of represented values for binary quadratic in order to generate and analyze new Siegel modular forms and their Fourier coefficients. For example, once sufficient conditions were proven, the following code was created to generate representatives of the equivalence classes of binary quadratic forms in the simplest case:

```
int main(){

  //Gets the discriminant from the user
  cout << "Input discriminant (negative numbers only):\n";
  int d;
  cin >> d;

  //This first loop identifies possible a values
  for(long int a = 1; a <= sqrt(float(-1*d)/3.0); a++)
    {
      //Identifies possible b values
      for(long int b = -a; b <= a; b++)
        {
          //Solves for c, then checks whether a,b,c work
          long int c = (d-(b*b))/(-4*a);
          //Checks they sum to D, checks gcd, and then ensures they meet the definiti\
on of reduced
          if(b*b-(4*a*c) == d && gcd(a,gcd(b,c))==1)
            {
              if(((abs(b)!=a && a!=c) || b>=0) && (abs(b)<=a && a<=c))
                {
                  addForm(a, b, c);
                }
            }
        }
    }
  //counts and prints the forms (not in that order)
  printForms();
  cout << "h(D)=" << countForms() << endl;

}
```

Additionally, further partitions of binary quadratic forms have been identified and computed based on stricter definitions of equivalence.
This code base will be able to twist Siegel paramodular forms using the described $W(\chi)$ and $\alpha_\chi(T)$ and analyze the resulting form's Fourier coefficients. Any new forms will then be added to databases of Siegel modular forms, such as LFMDB.

References

- Johnson-Leung, J., Dr., & Roberts, B., Dr. (2015, May 20). FOURIER COEFFICIENTS FOR TWISTS OF SIEGEL PARAMODULAR FORMS (EXPANDED VERSION). Retrieved July 19, 2018, from https://arxiv.org/pdf/1505.05463.pdf
- Kilford, L. J. (2008). *Modular forms a classical and computational introduction*. London: Imperial College Press.

Image Sources

- Desmos.com
- http://tutorial.math.lamar.edu/Classes/DE/FourierSeries.aspx
- https://en.wikipedia.org/wiki/Siegel_modular_form
- http://mathworld.wolfram.com/images/eps-gif/FourierSeriesSquareWave_800.gif
- https://en.wikipedia.org/wiki/Fundamental_domain#/media/File:ModularGroup-FundamentalDomain.svg

Acknowledgements

Thanks to my mentor, Dr. Jennifer Johnson-Leung for keeping me on track and optimistic, Daniel Reiss for his insightful advice, and the University of Idaho and the SURF program for making this possible.

Determining the Benefit Human Cytomegalovirus Gains by Down Regulating the Basement Membrane Protein Nidogen-1

Hannah Jaeger, Elizabeth Fortunato, John O'Dowd
Department of Biological Sciences

Introduction

- Human cytomegalovirus (HCMV) infects one percent of newborns annually
- 10% of these infants show CNS/PNS defects at birth and another 10% develop problems in the first 5 years of life
- Mother–child transmission of HCMV is mainly the result of primary (first exposure) maternal HCMV infection
- HCMV is able to pass through the human umbilical vein endothelial cells (HUVEC) and infect the fetus during an infection, which is uncommon for other viral infections
- HCMV uses tegument proteins to target the downregulation of nidogen 1 (NID1)
- Multiple resources are used by the virus to downregulate NID1 indicating some benefit is derived

Background

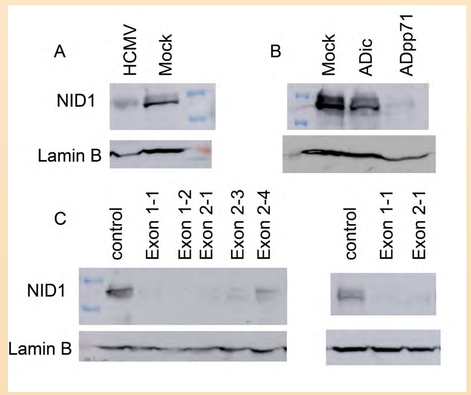

Figure 1: (A) HUVECs were mock- or virus infected at an MOI=20 and harvested 96 hpi for Western blot analysis. (B) HUVECs were infected with ADic or ADpp71 at MOI=10 and harvested at 48 hpi for Western blot analysis. (C) HFFs (left) or HUVECs (right) were transduced with 1 of 5 NID1 KO CRISPR lentiviruses, then pools were selected with puromycin, seeded at an equal density and harvested 72 hp plating for Western blot analysis for NID1.

Objective and Hypothesis

Our overall objective is to elucidate the benefit that HCMV derives from targeting NID1. A series of experiments listed below will test the hypothesis that HCMV uses NID1 downregulation to promote dispersal of infected cells via remodeling of the ECM in infected blood vessels.

Methods

We will test five different treatments of the HUVEC monolayers in order to determine the benefit of targeting NID1: 1) HPV immortalized HUVECs (control/baseline migration), 2) CRISPR NID1 KO HUVECs (to determine the effect of just NID1 knockdown), 3) control CRISPR-treated HUVECs, 4) HCMV-pp71 expressing HUVECs (AD-pp71) (which should knockdown NID1 but may change other additional aspects) and 5) HUVECs infected with full infection of HCMV as well as a mock infection for comparison. HUVECs stably infected with HPV were used for all treatments.

Transmigration Assay

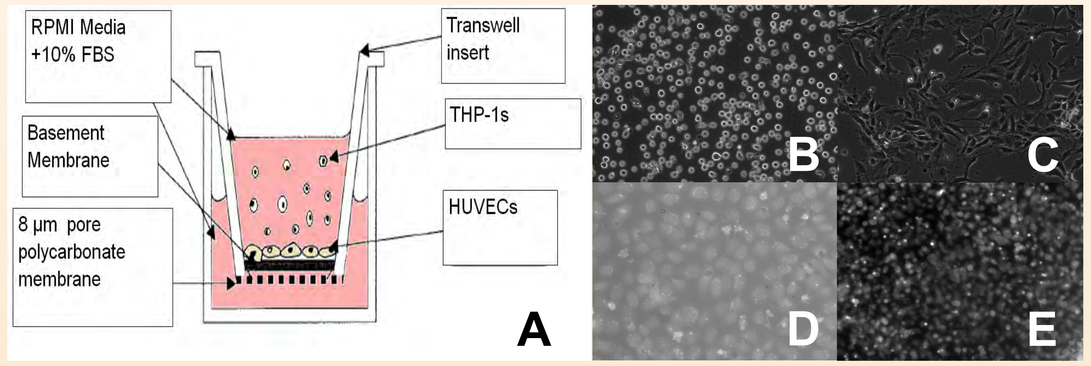

Figure 2. Schematic Diagram of Transmigration Assay and developed Monolayers. *A,* THP-1 monocytic cells were utilized due to their ability to migrate well through the transwell membrane. HUVECs from all four treatments were seeded in triplicate at a density of 1.5 x 10^4 cells in 200 µl of endothelial media onto transwell filters (8 µm pore size) with 600 µl of media in the bottom and allowed to grow to confluence for 8 days. Once confluent, 5 x 10^5 THP-1 cells will be seeded onto the transwell inserts on top of the HUVEC monolayer in 200 µl of RPMI media +FBS. Migration counts were recorded using a hemocytometer at 24 and 48 hours. *B,* THP1 cells, *c,* HUVECs, *d,* HUVEC monolayer in 96 well plate, and *e,* HUVEC monolayer on transwell insert stained with Calcein. All images were taken using a 10X objective.

Development of CRISPR HUVECs

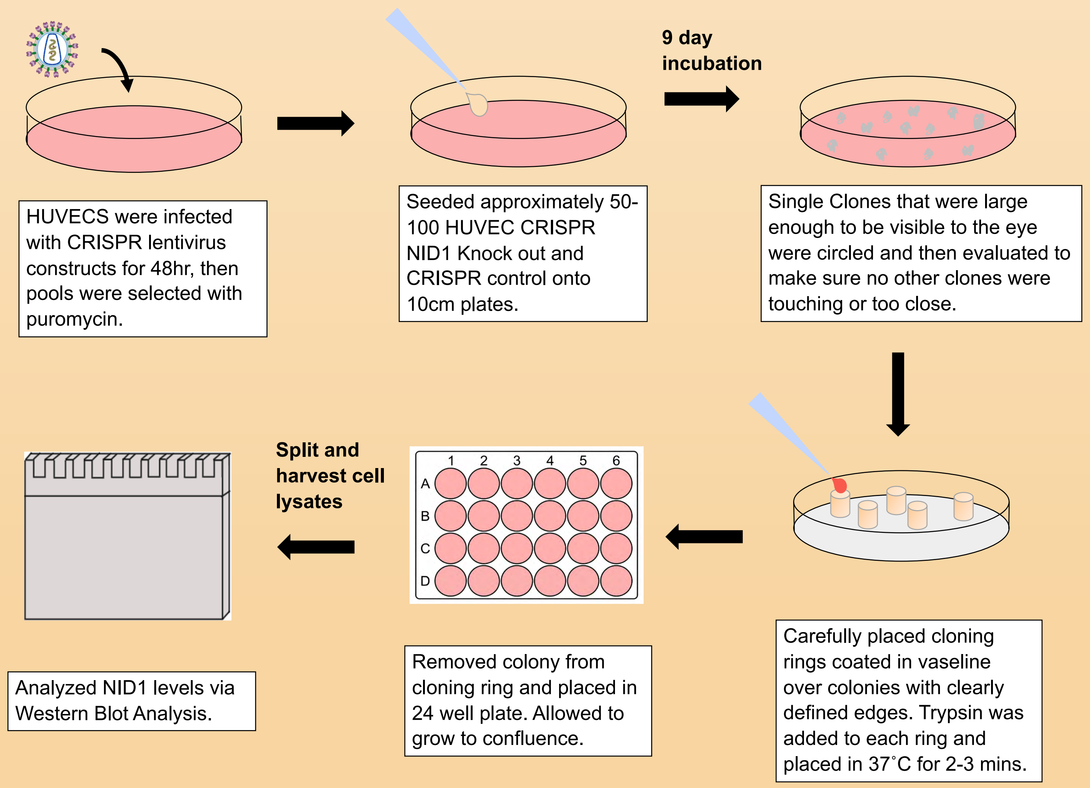

Figure 3. Schematic Diagram of Single cloning technique. HUVECs were infected with either a NID1 knock down or an off target CRISPR construct that does not affect any basement membrane proteins. Single cloning was performed and then colonies were analyzed for NID1 levels.

HCMV/ADpp71 Infections of HUVEC Monolayers

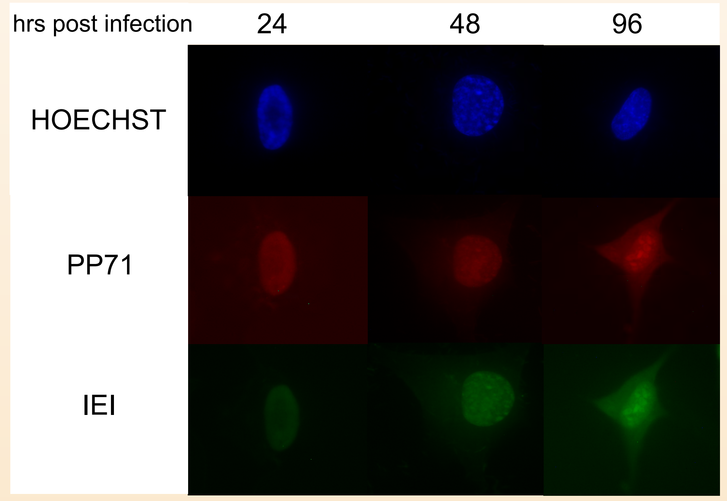

Figure 4. Images of PP71 and IE1 staining of infected HUVECs. Once each monolayer had formed HCMV was added at a MOI of 15 and equivalent DMEM F12 was added for mock infection. The media was changed after four hours and THP-1s were added after 24 hours for the migration assay. For the adenovirus infection (not shown), again monolayers were grown to confluence and infected with AD_{pp71} or AD_{ic} at RT for 30 mins. Media was then added onto of virus before adding THP1s 24 hours later.

Results

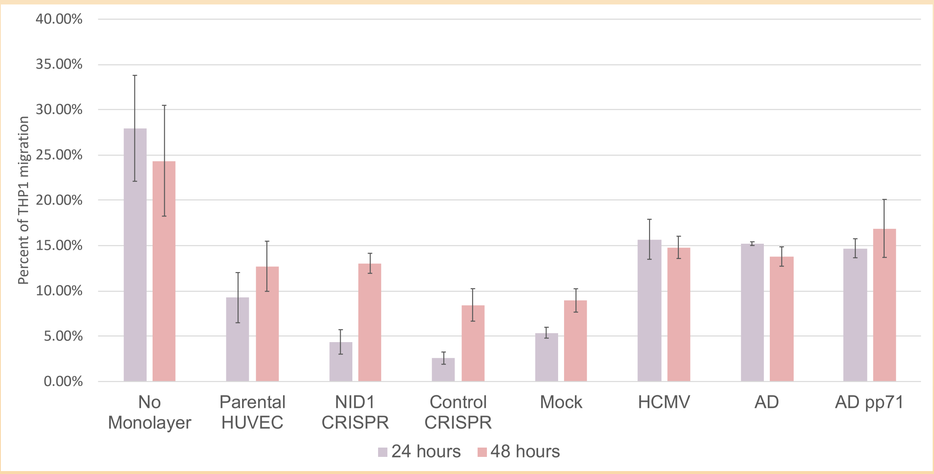

Figure 5. Preliminary data of transwell assay. 12 different transwells covering five different experiments for both the parental HUVECs and no monolayer present, 4 transwells in one experiment for both CRISPR constructs, and 2 transwells in one experiment for the HCMV infections and AD infections were tested.

Conclusion and Future directions

Multiple resources are used by the virus to downregulate NID1 indicating some benefit is derived. We know through these preliminary results that the presence of low amounts of NID1 in the CRIPRS pools had similar migration rates as the parental strand, indicating that even a small amount of NID1 helps to uphold the integrity of the monolayer. We also confirmed that a full infection increases migration compared to the mock without decreasing monolayer integrity. Decreased monolayer integrity in the adenovirus infections indicates troubleshooting for future experiments.

References

1. **G.L. Bentz, M. Jarquin-Pardo, G. Chan, M.S. Smith, C. Sinzger, A.D. Yurochko**, Human cytomegalovirus (HCMV) infection of endothelial cells promotes naive monocyte extravasation and transfer of productive virus to enhance hematogenous dissemination of HCMV, J. Virol. 80 (2006) 11539–11555.
2. **Dellacasagrande, J., P. A. Moulin, C. Guilianelli, C. Capo, D. Raoult, G. E. Grau, and J. L. Mege.** 2000. Reduced transendothelial migration of monocytes infected by Coxiella burnetti. Infect Immun 68:3784-3786.
3. **Dong, L., Y. Chen, M. Lewis, J. C. Hsieh, J. R. Chaillet, C. Y. Howell, M. Melhem, S. Inoue, J. R. Kuszak, K. DeGeest, and A. E. Chung.** 2002 Neurologica defects and selective disruption of basement membranes in mice lacking entactin-1/nidogen-1. Laboratory investigation; a journal of technical methods and pathology 82:1617-1630.

Acknowledgements

This work was supported by NIH grants RO1 AIO51563, INBRE program P20 GM103408 and COBRE program P20 RR015587 and the University of Idaho Summer Undergraduate Research Fellowship made possible by a 2017-2018 Undergraduate Research Grant from the Higher Education Research Council/Idaho State Board of Education. Thanks go to: Dr. Rob Kalejta for pp71 adenoviruses; Dr. Vic DeFelippis for HPV Huvecs and THP1s and Dr. Lisa Shaffer for initial FISH mapping help.

Live Imaging to Probe the Role of Microglia in Developmental Apoptosis in the Zebrafish Retina

University of Idaho

Jared Lambert, Anna Lovel, and Diana Mitchell

Department of Biological Sciences, University of Idaho, Moscow, ID

Abstract

During mammalian retinal development, programmed cell death (apoptosis) occurs in large waves in a spatio-temporal fashion to generate functional retinas. In zebrafish comparably smaller waves have been observed and are thought to represent fine-tuning of developing retinal tissue (Biehlmaier 2001). It is appreciated that tissue resident macrophages clear apoptotic cells (Hochreiter-Hufford 2013), however, specific roles for microglia in cell survival/death and clearance during retinal development in zebrafish have not been documented. We used an inducible system to specifically deplete macrophages/microglia during retinal development (Petrie 2015) and found an increased number of apoptotic cells in the retina compared to controls. This finding suggests that microglia clear larger numbers of apoptotic cells than is currently appreciated, or alternatively, that microglia provide survival signals to developing retinal cells. To address clearance of apoptotic cells during zebrafish retinal development in real-time, we live imaged fluorescently labeled retinal microglia together with apoptotic cells using acridine orange (AO). We observed that microglia sense and engulf cells prior to AO incorporation, and that engulfed apoptotic cells undergo dynamic movements as microglia continue active migration. This suggests that apoptotic cells visualized in fixed tissues using AO may not represent true levels of apoptosis and their retinal locations may differ from where apoptosis was initiated.

Background

Figure 1. Increase in Apoptotic Cells When Micrgolia are Depleted from the Developing Zebrafish Retina

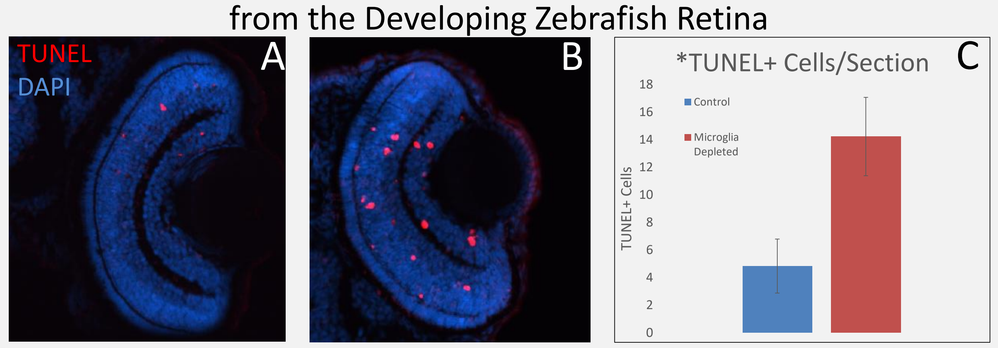

Cryosections from control (A) zebrafish retinas (10 µm thickness) or those depleted of microglia (B) were stained for TUNEL* (red) and DAPI (blue). Retinas with depleted microglia show an increased number of TUNEL+ cells than that of control eyes (C).

*TUNEL stands for Tdt-mediated dUTP Nick End Labeling, and is used to label apoptotic cells undergoing DNA fragmentation.

Methods

- The zebrafish line Tg(*mpeg1*:mCherry) was used to visualize microglia through fluorescent microscopy, as it expresses a red fluorescent marker in macrophages.
- Embryos were soaked in Acridine Orange (AO) prior to imaging, which binds to fragmented DNA in late stage apoptotic cells and is visualized through fluorescent microscopy.
- Embryos were immobilized with tricaine then embedded in 2% agarose overlayed with 1% agarose. The agarose was then covered with an AO/tricaine/water solution, allowing us to visualize apoptotic cells appearing during imaging, as well as keeping the fish immobilized and alive.
- Embryo Eyes were imaged on a Nikon Spinning Disk Confocal Microscope every 5 min. for a duration of 8 hours, starting at 52 hours post fertilization (hpf) or ~2 ½ Days Post Fertilization (dpf).
- Z-stacks were obtained at each timepoint, with each stack measuring 5 microns in order to follow microglia and AO+ cells in 4 dimensions.

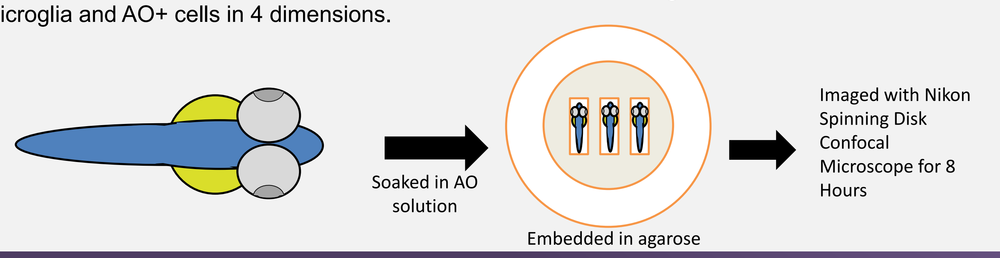

Results

Figure 2. Microglia Phagocytize Apoptotic Cells before and after DNA Fragmentation

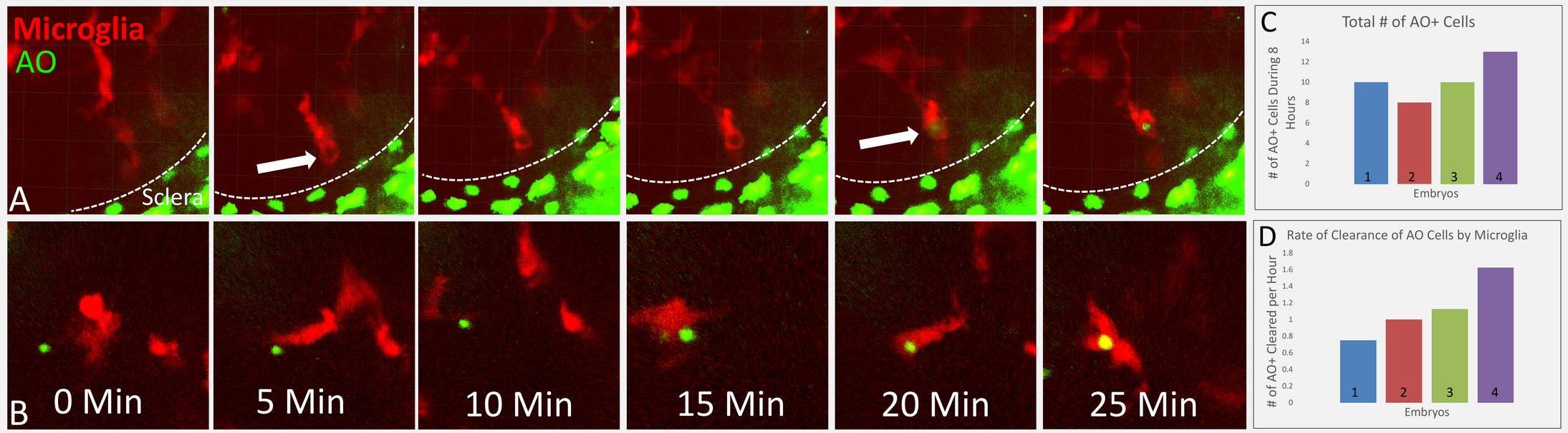

Apoptotic cells are cleared by microglial phagocytosis, which can occur before (A) or after (B) DNA fragmentation. Most of the time, AO+ signal appears after phagosome formation (shown by arrows) as shown in A. The total # of AO+ cells over 8 hours (C). Clearance rate of AO cells over the 8 hour imaging period (D).

Figure 3. Displacement of AO+ Cells

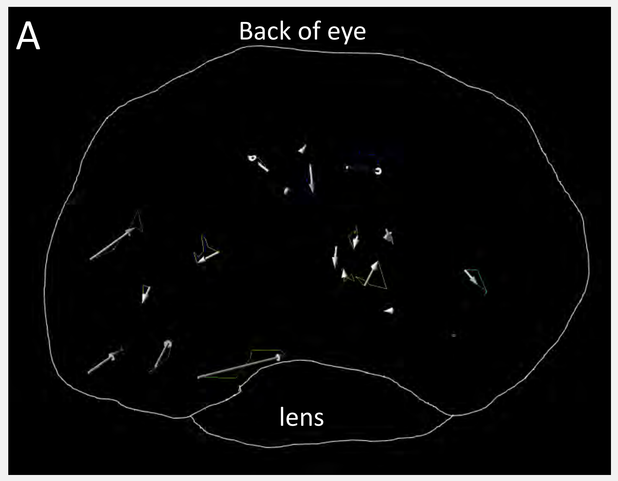

AO+ apoptotic cells were displaced from their original position after being engulfed by microglia, and disappear in different positions than when they were first phagocytized (A). AO+ cells moved around at a speed consistent with documented microglial speeds (Morsch 2015) (B). AO+ Cells are displaced from their original position as microglia continue to move about the retina (C). The AO+ cells remain visible for ~20-80 minutes, until they are broken down inside of microglia, likely in the lysozomes (D).

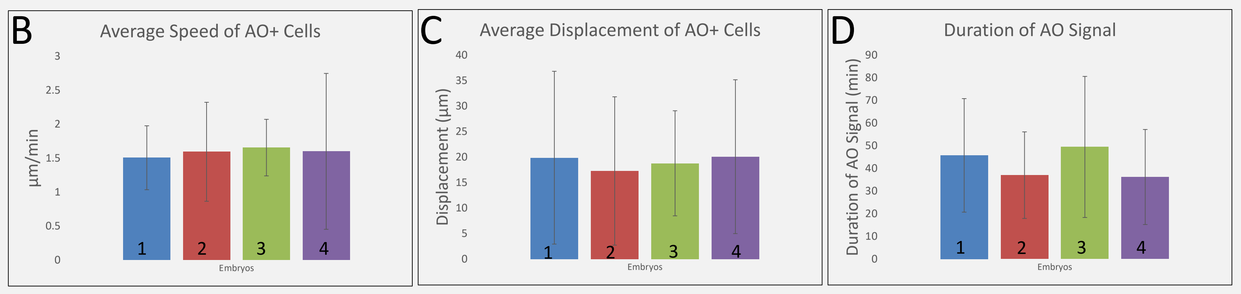

Conclusions and Future Directions

Microglia are actively involved in clearing apoptotic cells from developing zebrafish retinas. Most of the time, microglia sense and engulf apoptotic cells prior to DNA fragmentation.

After engulfing AO+ cells, microglia continue to move about the retina, carrying the apoptotic cells with them. Apoptotic cells are digested by microglia as they move about, and completely degenerate in a location different than their generation.

Our next steps will be to (i) inhibit phagocytosis and (ii) inhibit cell death to see if there is an equivalent increase in apoptotic cells. We will also image with early apoptotic markers to visualize engulfment of cells in earlier stages of apoptosis.

The combined results of these studies will allow us to determine more accurate rates of programmed cell death during retinal development in zebrafish and also determine if microglia may provide survival signals to developing retinal neurons.

Acknowledgements

Funding: Summer Undergraduate Research Fellowship (SURF), Mitchell lab startup funds.
Ann Norton and Onesmo Balemba, University of Idaho IBEST OIC;
Ruth Frey, (Stenkamp lab) for technical assistance and zebrafish care;
and Dr. Deborah Stenkamp for helpful review of our data.
The Tg(*mpeg1*:mCherry) line was obtains from ZIRC.

References

1. Biehlmaier, Oliver; et al. 2001. Onset and time course of apoptosis in the developing zebrafish retina. Cell Tissue Res, vol 306(2):199–207.
2. Hochreiter-Hufford, A., and K. S. Ravichandran. “Clearing the Dead: Apoptotic Cell Sensing, Recognition, Engulfment, and Digestion.” Cold Spring Harbor Perspectives in Biology, vol. 5, no. 1, Jan. 2013, doi:10.1101/cshperspect.a008748.
3. Petrie, Timothy A; et al. 2015. Macrophages modulate adult zebrafish tail fin regeneration. Dev, vol 142
4. Morsch, Marco et al. 2015. “In Vivo Characterization of Microglial Engulfment of Dying Neurons in the Zebrafish Spinal Cord.” Frontiers in Cellular Neuroscience 9 (2015): 321. PMC.

Ionic and Biomolecular Movement Through Functionalized Thin Filmed Polymers

Garrett E. Larson and Kristopher V. Waynant*
Dept. of Chemistry, University of Idaho, Moscow, Idaho, 83844

Abstract

Ions and biomolecules are essential for many functions of the human body such as bone strength and development, muscle contractions, and cell functions like membrane transport and membrane potentials. This experiment will use post-polymerization functionalization to bind to Calcium ions (Ca^{2+}), using ion selective electrode polymers, this binding could be a way of monitoring calcium levels in the body. The polymer scaffolding will be made from Poly-(3-sulfopropyl methacrylate). This sulfonic acid polymer will capture Ca^{2+} through negatively charged terminal ends, in acidic environments, that can ionically bond to the Ca^{2+}. These polymers will be grown on carbon nanotubes. We will characterize these polymers with transmission electron microscopy (TEM) and RAMEN spectroscopy. The transport of Ca^{2+} through the polymer surfaces will be monitored by measuring the voltage change on the polymer electrode as a Calcium solution is passed over it. A device was engineered to hold the polymer in a closed system to allow the solution to pass over it and out, which allows us to monitor the concentration of the calcium solution after polymer interaction.

Background

Carbon nanotubes (CNTs) are conductive and can be printed onto surfaces to serve as a reliable sensor. They can also serve as a surface for polymerization to directly sense Ca^{2+} ions.

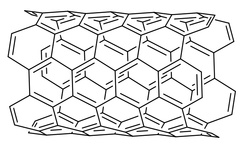

MW-CNT

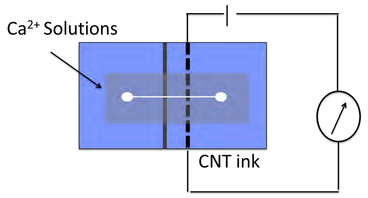

Nanotube inks can be mixed with calcium ionophore to have reliable calcium sensing. Monomers can also be synthesized to act as the ionophore in the solution when they are polymerized onto the carbon nanotubes. The inks cocktails are drop casted onto the device with a reference electrode to make an ion selective electrode. Where the voltage can be measured while running a calcium solution through the device.

Nink 1000

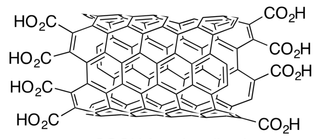

COOH functionalized MWCNTs plus SDS in Water

Calcium Ionophore Cocktails

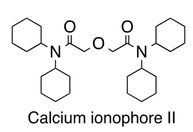

Calcium ionophore II

plus Sodium tetraphenylborate o-Nitrophenyl octyl ether in THF solution

Polymerization

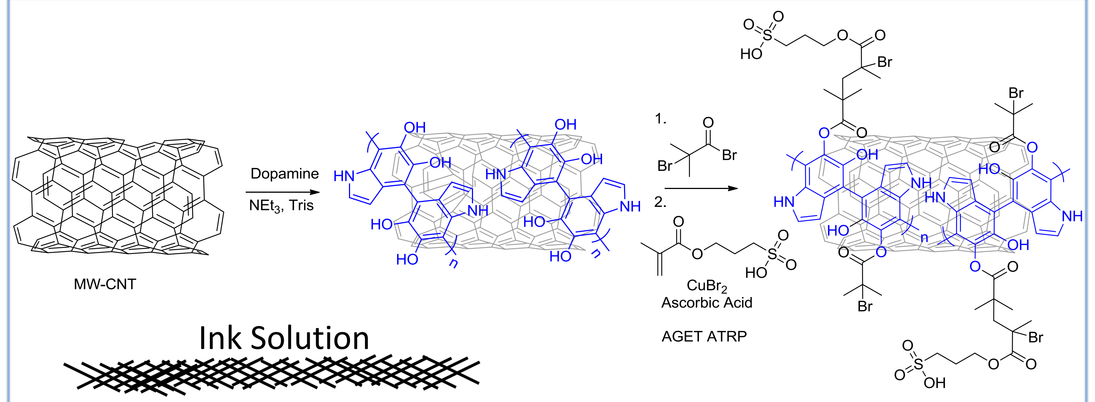

Multi-walled Carbon nanotubes are reacted with dopamine to coat the nanotubes in polydopamine (PDA). Then they are reacted with BIBB which acts as the initiator for the polymerization to add 3-sulfopropyl methacrylate to the end of the CNT. These nanotubes were added to an ink solution and drop casted onto a glass slide to make an ion selective electrode.

Transmission Electron Microscopy

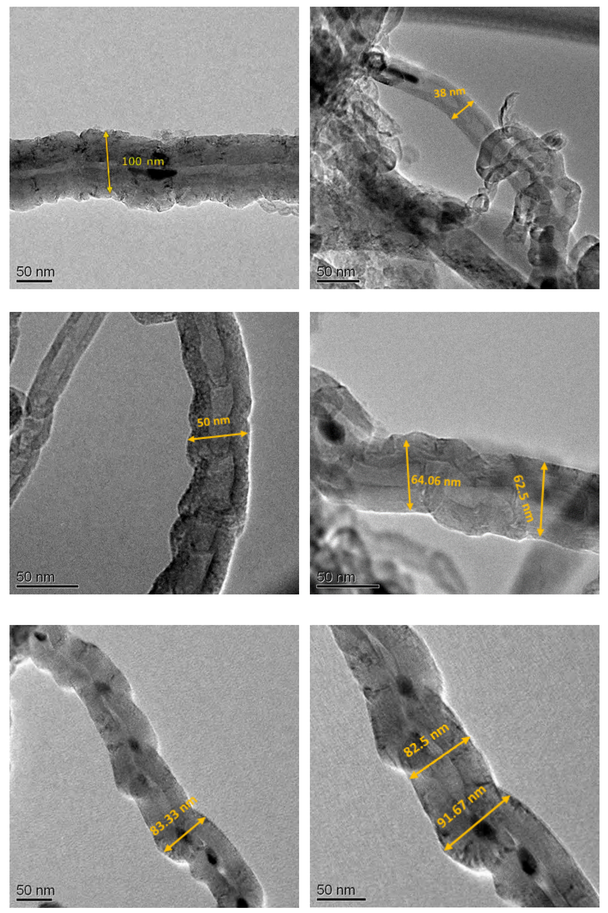

CNT (Starting Material)
Average Diameter ~40 nm

CNT-PDA
Average Diameter ~55 nm

CNT-PDA-BIBB
Average Diameter ~80 nm

Devices

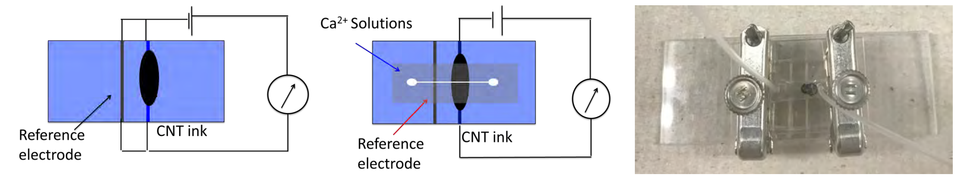

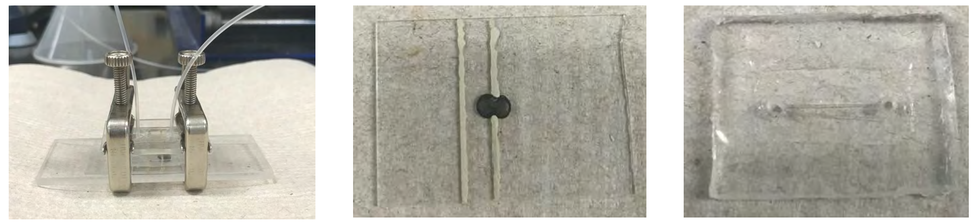

Future Work

- Different Monomers
  - Iminodiacetic acid
  - Malonic Acid

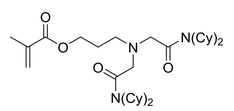

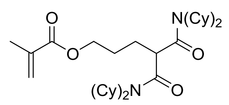

- Printing inks onto devices with a printer
- Determining if the inks are ion selective

References

1. Matyjaszewski K., et al. *Progress in Polymer Science* **2012**, 37, 18–37
2. Wang, Li-Ping, et al. *Reactive and Functional Polymers* ***2016****, 59-64.*
3. Koo, H. J.; Waynant, K. V.; Zhang, C. J.; Braun, P. V., Acs Applied Material Inter 2014, 6 (16), 14320-14326

Acknowledgements

Thanks to Dr. Kristopher Waynant and the University of Idaho Summer Undergraduate Research Fellowship for the funding and opportunity.

Air-Brushed Nonfouling Drug Delivery Microfiber Mats

Jacquelin Martinez and Dr. Matthew Bernards

Chemical & Materials Engineering, University of Idaho, Moscow, ID

Introduction

A significant challenge in the field of biomaterials is the nonspecific adsorption of proteins to implants. Upon implantation, this nonspecific protein adsorption triggers the natural foreign body response leading to encapsulation and failure of the device. Zwitterionic materials are excellent at resisting protein adsorption. For this reason, we are investigating the zwitterionic polymer poly(sulfobetaine methacrylate) (polySBMA). Using polySBMA, our goal is to produce nonfouling-polymer-microfibers by airbrush-spraying. To date we have explored the influence of spraying pressure, nozzle diameter, distance to collector, polymer molecular weight, and solvent. We have also optimized the use of a photo-polymerization reaction to reduce the water solubility of the resulting microfibers. The long term goal is to use these microfibers to create a high-surface-area drug delivery platform.

Approach

Polymerize

In round-bottom flask add:
- Potassium persulfate ($K_2S_2O_8$) initiator
- KCl to control molecular weight (M.W.)
- Pure water (H_2O)

Let this purge in nitrogen gas (N_2)
Introduce SBMA monomer

Dialysize

In 4 L beaker add:
- DI H_2O
- Prepared dialysis membrane filled with polySBMA solution
- Stir bar

Place on stir plate
Dialysize for over 24 hours

Prepare

Recover the polymer
Make a 1:1 solution of PolySBMA to solvent
- Add cross-linker triethylene glycol dimethacrylate (TEGDMA)
- Add photo-initiator 2-Hydroxy -4'-(2-hydroxyethoxy)-2-methylpropiophenone

Load into spraying reservoir

Spray

Spray polymer onto petri dish
While spraying, expose to UV-light
After spraying, soak the fibers to H_2O
Place the soaked fibers in a desiccator

System

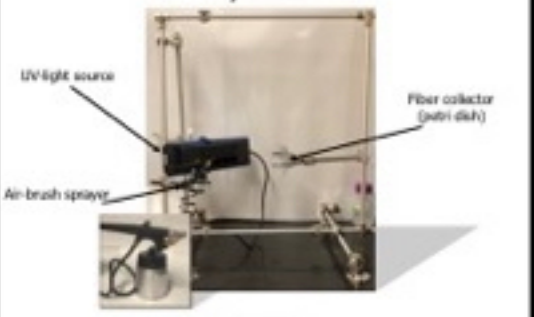

Results

✓ Varying KCl concentration

0 M KCl | 2.5 M KCl | 3.5 M KCl

At 0 M KCl, the polymer solution is extremely viscous and large fibers are produced. When the KCl concentration exceeds 2.5 M, fibers are not uniform and they begin to have a "melting" effect.

✓ Solvent

polySBMA in 0.25 M NaCl(aq) 1:1 | polySBMA in 0.25 M NaCl(aq) 1:1 | polySBMA in 0.30 M NaCl(aq) 1:1

Solvents tested: Ethanol, Acetone, NaCl(aq)

Results: When using ethanol or acetone, polySBMA would not dissolve and instead dehydrate and form into a hard polymer ball.

Optimal solvent conditions: NaCl(aq) proves to dissolve polySBMA. At concentration below 0.25 M NaCl, beading occurs at the intersections; above 0.25M, fibers are uniform.

✓ Spraying Pressure

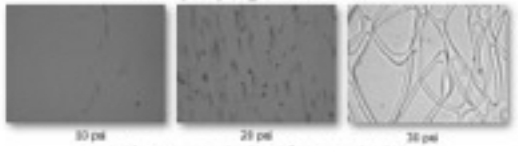

10 psi | 20 psi | 30 psi

When pressure reaches 30 psi, fibers are produced.

✓ Spraying nozzle diameter

Set at large diameter, or approximately 5 rotations wide.

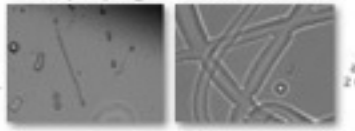

Set at small diameter, or approximately 2 rotations wide.

✓ Varying photo-initiator concentration

0.089 M $C_{13}H_{18}O_5$ | 0.022 M $C_{13}H_{18}O_5$ | 0.009 M $C_{13}H_{18}O_5$

The concentration of photo-initiator is calculated on a basis of 10 mL of a 1:1 polySBMA to solvent solution with 200 µL of TEGDMA.

✓ Water solubility

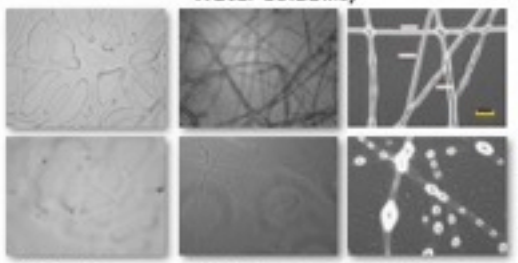

No photo-initiator, cross-links, or UV exposure | 0.022 M photo-initiator 4 minute UV exposure | 0.009 M photo-initiator 8 minute UV exposure

Conclusions

- Increasing KCl concentration decreases M.W. and produces uniform fibers
- Increasing NaCl concentration allows for spraying and produces uniform fibers
- Optimal spraying occurs at 30 psi and "2-rotation" nozzle diameter
- Optimal photo-initiator concentration is 0.009 M $C_{13}H_{18}O_5$
- Photo-polymerization reduces water solubility

Future Work

1. Characterize the base case microfiber dimensions
2. Demonstrate nonfouling properties
3. Quantify polySBMA M.W. by gel permeation chromatography
4. Characterize the release of two pseudo-drug species

Acknowledgements

- National Grand Challenge Scholars Program
- Office of Undergraduate Research

University of Idaho
Office of Undergraduate Research

Effects of pre-transport administration of Meloxicam on indicators of protein metabolism in transported 4-day old Jersey calves

Myers C. A., Z. Carlson, G. Murdoch, and G. E. Chibisa
University of Idaho, Moscow, ID

TAP TO GO BACK TO KIOSK MENU

Introduction

- Currently, 1 in 10 heifers and most bull-calves are transported to calf-rearing facilities within the first 48 h of birth in the U.S.
- Transport at this vulnerable stage causes stress-related changes in protein metabolism that could restrict growth, since an increase in blood cortisol was shown (Gore et al., 1993; Paddon-Jones et al., 2006) to cause muscle wasting in humans by increasing the rate of protein breakdown relative to synthesis.
- However, there is no information on the impact of transport-related stress on protein metabolism in calves, and the strategies that could potentially be used to mitigate the negative outcomes.
- Our objective was to investigate the effects of transport stress and pre-transport administration of an analgesic in calves (< 1 week old) on blood metabolites, and the gene expression profiles for markers of protein breakdown and synthesis in muscle.

Methods

- A total of 20 calves (age ±SD; 4 ± 0.5 day) were randomly administered either a placebo (CON; n = 10) or meloxicam (MEL; n = 10) orally (1 mg/kg) right before a 8-h road trip.
- Blood samples were collected before departure (0 h), on arrival (8 h) and 96 h post-arrival and analyzed for cortisol and haptoglobin (0 & 8 h samples), and 3-methylhistidine (3-MH), plasma urea-N (PUN) and amino acids (AA; 96 h samples).
- After collection of the last blood sample (96 h), calves were slaughtered by captive bolt and exsanguination.
- Skeletal muscle tissue samples were collected and used to determine transcript abundance of 3 markers of protein synthesis and breakdown using qPCR.

Results

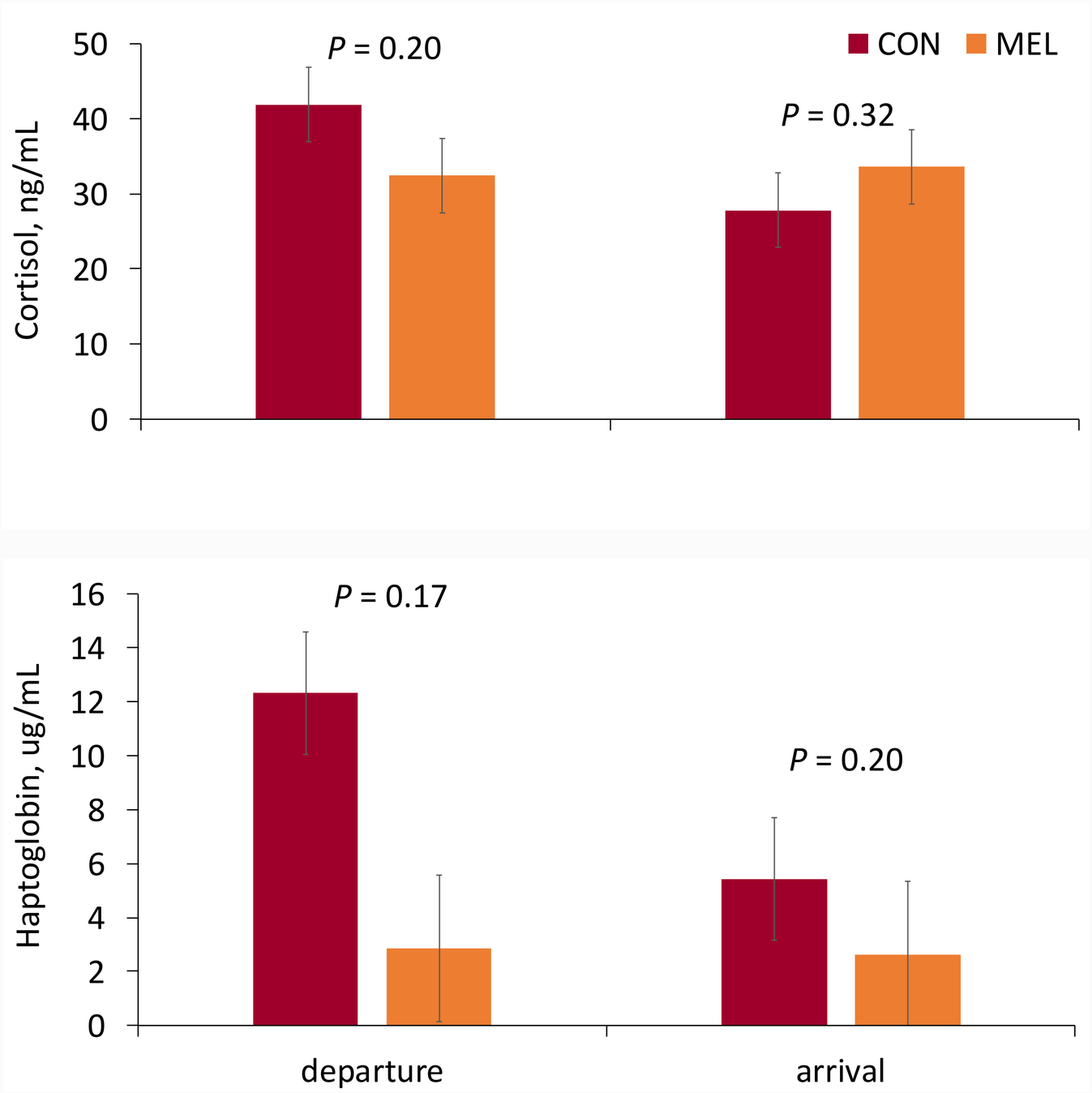

Figure 1. Blood cortisol and haptoglobin concentration at departure and arrival in calves administered either a placebo (CON) or meloxicam (MEL) prior to road transport (8 h trip).

Table 1. Plasma AA, 3-methylhistidine and urea-N concentration 96-h post-arrival in calves administered either a placebo (CON) or meloxicam (MEL) prior to road transport (8 h trip).

	Treatment			
Variable	CON	MEL	SEM	*P*-Value
Alanine	133	119	11.7	0.41
Arginine	2.96	4.78	0.89	0.17
Asparagine	31.8	31.9	1.70	0.99
Aspartic acid	15.7	14.7	0.83	0.41
Citrulline	7.87	5.47	0.87	0.07
Glutamic acid	34. 4	31.3	2.95	0.47
Glutamine	16.6	14.6	0.99	0.18
Glycine	32. 8	33.8	2.30	0.75
Histidine	31.6	29.0	2.01	0.36
Isoleucine	19.2	15.2	1.25	0.04
Leucine	33.2	29.8	1.77	0.19
Lysine	11.3	10.6	0.68	0.48
Methionine	5.50	5.43	0.261	0.84
Phenylalanine	31.0	28.4	2.47	0.46
Proline	11.2	9.6	0.81	0.19
Serine	9.218	8.632	0.63	0.52
Threonine	10.2	9.3	0.49	0.21
Tryptophan	46.5	41.2	3.554	0.30
Tyrosine	38.9	34.7	3.044	0.33
Valine	7.91	6.73	0.526	0.13
3-methylhistidine	0.380	0.368	0.036	0.82
Urea-N	12.3	11.5	0.799	0.46

Effects of pre-transport administration of Meloxicam on indicators of protein metabolism in transported 4-day old Jersey calves

Myers C. A., Z. Carlson, G. Murdoch, and G. E. Chibisa

University of Idaho, Moscow, ID

TAP TO GO BACK TO KIOSK MENU

Results (cont.)

Table 2. Transcript abundance of genes related to mammalian target of rapamycin (mTOR) and ubiquitin-proteasome system (UPS) in calves administered either a placebo (CON) or meloxicam (MEL) prior to road transport (8 h trip).

	Treatment			
Variable[1]	CON	MEL	SEM	*P*-Value
mTOR (protein synthesis)[2]				
mTOR	-4.17	-4.15	0.054	0.848
S6K1	-3.96	-4.02	0.039	0.319
4E-BP1	-4.33	-4.33	0.041	0.100
EIFK3	-3.44	-3.44	0.036	0.932
UPS (protein breakdown)[3]				
UBA	-4.70	-4.70	0.058	0.871
UBE2G1	-3.50	-3.44	0.055	0.421
UBE2G2	-5.93	-5.91	0.060	0.823
Atrogin-1	-5.73	-5.75	0.057	0.832
TRIM-63	-3.34	-3.31	0.056	0.672

[1]copies/copy 18S

[2]S6k1 = ribosomal protein S6 kinase, 4E-BP1 = eukaryotic translation initiation factor 4E binding protein, EIFK3 = eukaryotic translation initiation factor 3

[3]UBA = ubiquitin-like modifier activating enzyme, UBE2G1 and UBE2G2 = ubiquitin conjugating enzymes, TRIM63 = E3 ubiquitin-protein ligase

Table 3. Production performance in calves administered either a placebo (CON) or meloxicam (MEL) prior to road transport (8 h trip).

	Treatment			
Variable	CON	MEL	SEM	*P*-Value
Transportation shrink, kg	1.68	1.75	0.374	0.896
ADG for 4 d, kg/d	1.95	1.983	0.096	0.814
Milk replacer intake, kg/d	1.067	1.129	0.021	0.05
Feed efficiency	1.841	1.761	0.102	0.584

Summary

- There was no treatment effect on blood cortisol and haptoglobin concentrations, whereas isoleucine was higher and citrulline concentration tended to be higher for MEL than CON calves.
- Although milk replacer intake tended to be higher for MEL compared to CON calves, there was no treatment effect on transportation shrink, ADG and feed efficiency
- Pre-transport administration of MEL had no effect on blood cortisol concentration, and this possibly accounts for the lack of a treatment effect on most measures of protein metabolism including blood urea-N, 3-MH, and mRNA abundance for components of the mTOR or UPS pathways.

References

1) Gore et al., 1993. Ann. Surg. 218:679-684.
2) Paddon-Jones et al. J. Clin. Endocrinol. Metab. 91:4836-4841.doi:10.1210/jc.2006-0651

Why your gut may be working against you: gut derived molecules cause dysmotility and neuropathy in high fat fed mice

Jessica Nicholson[1], Sydney Kuther[1], Yvonne Nyavor[1], Heino Heyman[2] , Thomas Metz[2], Onesmo Balemba[1]
[1]Department of Biological Sciences, University of Idaho, Moscow, Idaho 83843, USA
[2]Pacific Northwest National Laboratory, Richland, Washington 99354

INTRODUCTION

Type 2 Diabetes (T2D) is the seventh leading cause of death in the United States. Along with this disease comes several neurological effects like enteric neuropathy and even blindness. Previous studies using mice fed a high fat (HF) diet suggest that symptoms of gastrointestinal (GI) dysmotility and neuropathy develop before diabetes. In addition, ileocecal supernatants from HF mice cause GI muscle contractions to slow down, and also causes a decrease in inhibitory myenteric neurons[1]. *However, substances from GI content that disrupt bowel motility and damage GI neurons are not known*.

HYPOTHESIS

Ileocecal supernatants from HF diet mice separated into fractions will cause gastrointestinal dysmotility and neuropathy.

GOAL

Identify gut derived molecules that may cause diabetic dysmotility and/or neuropathy.

MATERIALS/METHODS

- Ileocecal supernatants from mice were fractionated using high performance liquid chromatography (HPLC)
- Intestinal tissues were dissected from C57BL/6J mice down to the longitudinal muscle myenteric plexus, cultured with ileocecal supernatant fractions for 48 hours, and fixed with 4% Paraformaldehyde
- Contractions were counted at 0, 24, and 48 hours
- Tissues were stained for neuronal nitric oxide synthase (nNOS) and anti-neuronal nuclear autoantibody-1 (ANNA-1) using immunohistochemistry
- Samples were imaged using a Nikon Spinning Disk microscope and analyzed with Nikon's NIS Elements software

HF diet causes production of substances that disrupt intestinal muscle contractions

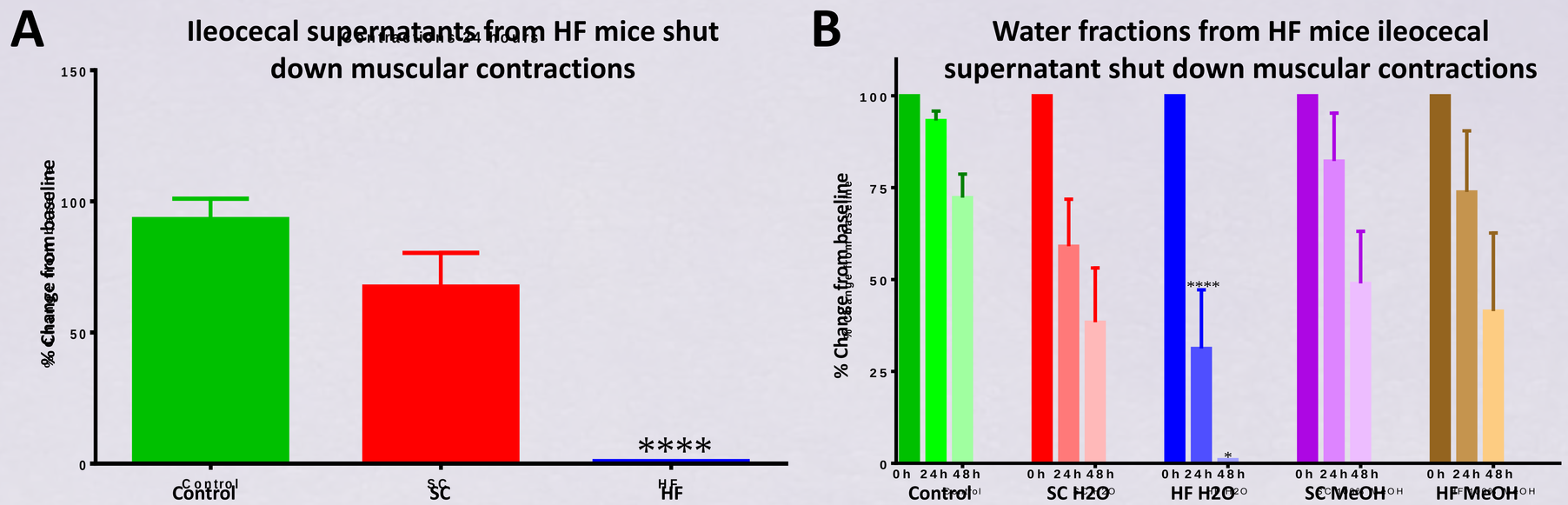

Figure 1. A) Preliminary data showing a significant reduction in smooth muscle contractions of samples exposed to HF mice ileocecal supernatant. B) HF water fractions decreased smooth muscle contraction suggesting they contain active molecules. *p ≤ 0.05, **p ≤ 0.01, ***p ≤ 0.001, ****p ≤ 0.0001; n= 2-9

Fractions from ileocecal supernatant cause reduction in nNOS neurons

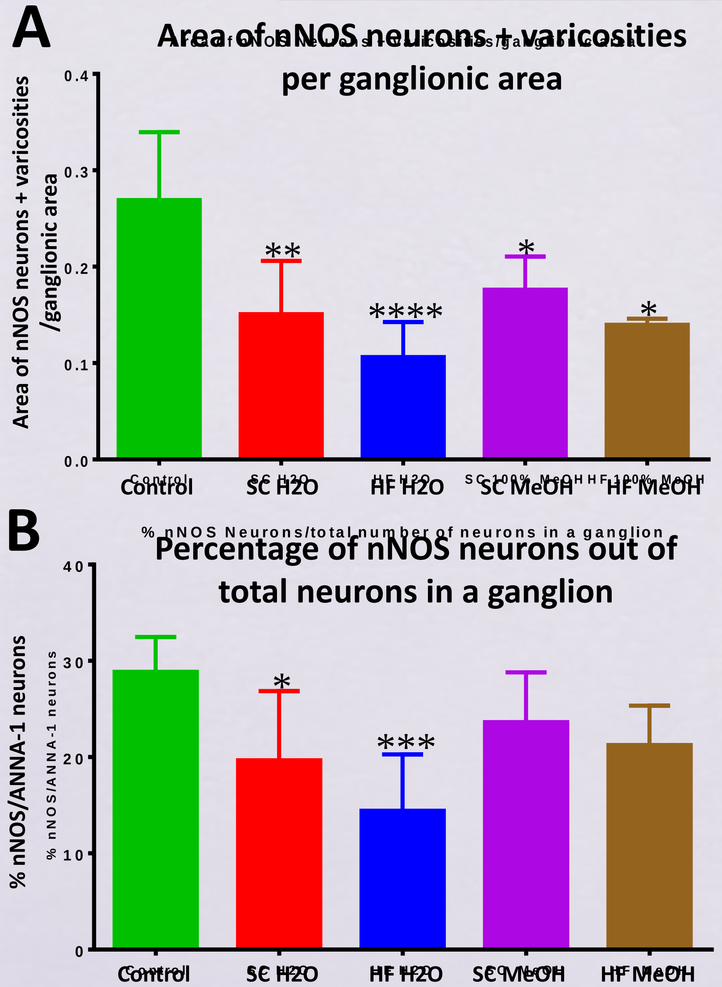

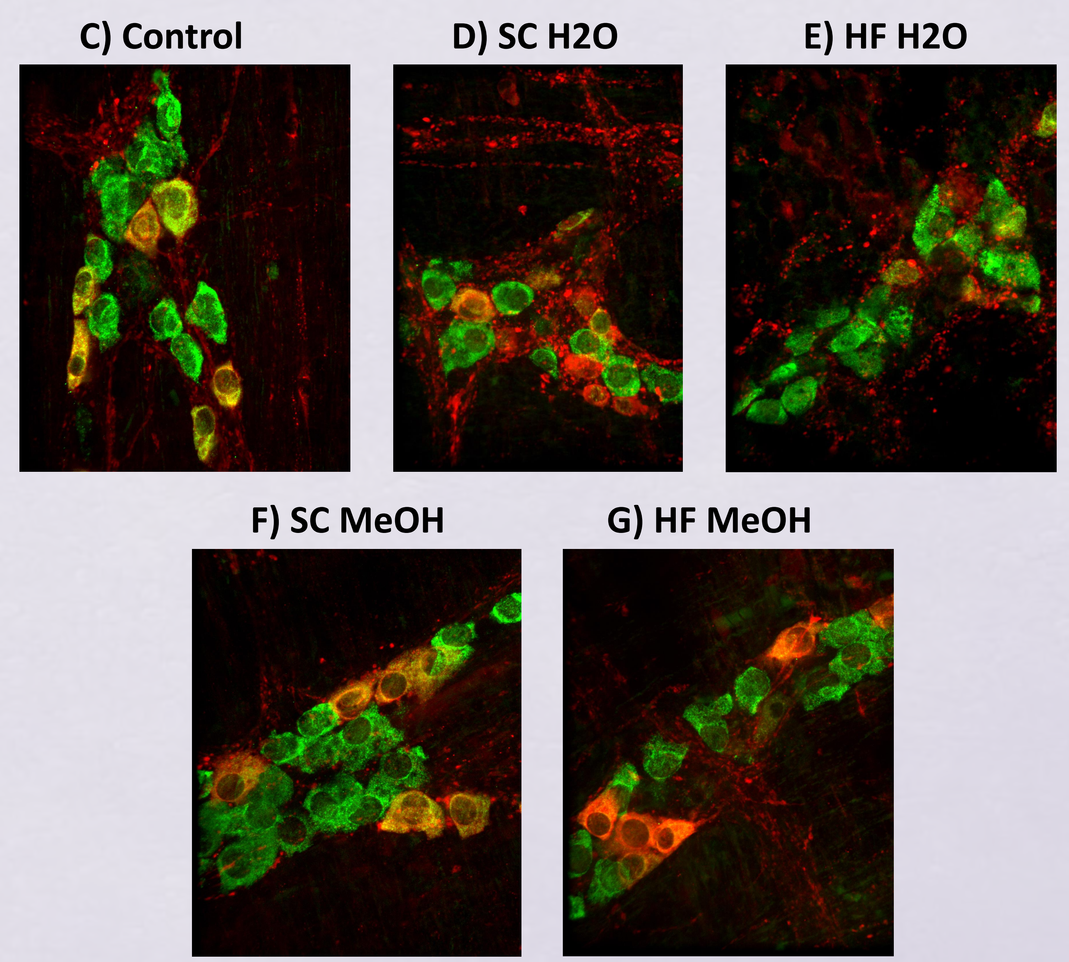

Figure 2. A-B) Summary data showing a significant decrease in nNOS neurons (inhibitory motor neurons) and varicosities in tissues treated with ileocecal fractions from both SC and HF mice (A) and a decline of nNOS neurons in tissues treated with the HF water fractions (B). C) Representative image of nNOS (in red) and ANNA-1 (in green) stained neurons and varicosities from an untreated cultured sample. D) Representative image of sample treated with SC H2O fraction. E) Representative image of sample treated with HF H2O Fraction, showing poor condition of ANNA-1 neurons and no nNOS neurons. F) Representative image of sample treated with SC MeOH fraction. G) Representative image of sample treated with HF MeOH fraction. n= 3-9

DISCUSSION

High fat ingestion causes enteric neuropathy in mice by eliciting oxidative stress and inflammation in inhibitory motor (nNOS) neurons. This is though to be due to dietary factors – mainly palmitate and bacterial lipopolysaccharide[2]. What causes dysmotility is unknown. Our results suggest that HF water fractions contain molecules that block muscle contractions and damage inhibitory motor neurons.

CONCLUSION

These results suggest that molecules present in supernatant of HF diet mice ileocecal content causes dysmotility and neuropathy in mice. Further sub-fractionation and analysis of chemical composition could help broaden knowledge about causes of dysmotility and neuropathy in obese and diabetic patients.

FUTURE WORK

HF water fractions causing dysmotilty and neuropathy will be further fractionated down to sub-fractions so that the molecules causing dysmotility and neuropathy can be identified.

REFERENCES

1. Reichardt, F., Chassaing, B., Nezami, B. G., Li, G., Tabatabavakili, S., Mwangi, S., . . . Srinivasan, S. (2017, February 08). Western diet induces colonic nitrergic myenteric neuropathy and dysmotility in mice via saturated fatty acid- and lipopolysaccharide-induced TLR4 signalling. Retrieved from https://physoc.onlinelibrary.wiley.com/doi/abs/10.1113/JP273269
2. Cani, P. D., Amar, J., Iglesias, M. A., Poggi, M., Knauf, C., Bastelica, D., . . . Burcelin, R. (2007, July 01). Metabolic Endotoxemia Initiates Obesity and Insulin Resistance. Retrieved from http://diabetes.diabetesjournals.org/content/56/7/1761.short

ACKNOWLEDGEMENTS

This project was supported by the Office of Undergraduate Research through a Research Fellowship made possible by a 2017-2018 grant from the Higher Education Research Council/Idaho State Board of Education. I would like to also thank Ann Norton and Michael Camerino for help with imaging and analysis!

Antibody Escape Mutations in Respiratory Syncytial Virus

Frankie Scholz, Sierra Beach, Ashley DeAguero, Craig Miller, Tanya Miura

Department of Biological Sciences, University of Idaho, Moscow, ID

Abstract:

Respiratory Syncytial Virus (RSV) is a small intracellular pathogen that infects people of all ages. RSV is responsible for many deaths each year and currently, there is no licensed vaccine. In an alternate form of therapy, monoclonal antibodies can be used to treat infection, however, the monoclonal antibody, Palivizumab, is only administered to high risk infants. In this study, we are investigating the ability of RSV to mutate under stress of a human monoclonal antibody, D25. Under stress, RSV is pressured to evolve resistance against antibodies, known as antibody escape mutations. We introduced RSV to rounds of selection in the presence of D25 and allowed time for mutations to arise. After ten rounds of selection in HEp-2 cells, viral mutants required significantly more antibody for neutralization. The mutants were sequenced for specific amino acid changes and compared to the modeled predictions. These results will help us better understand how RSV evolves to escape neutralization.

Background:

Respiratory Syncytial Virus

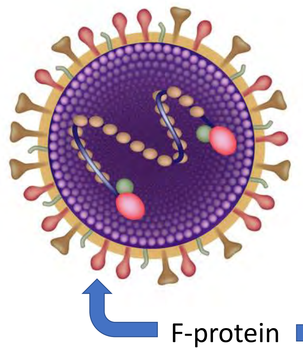

Monoclonal Antibody D25

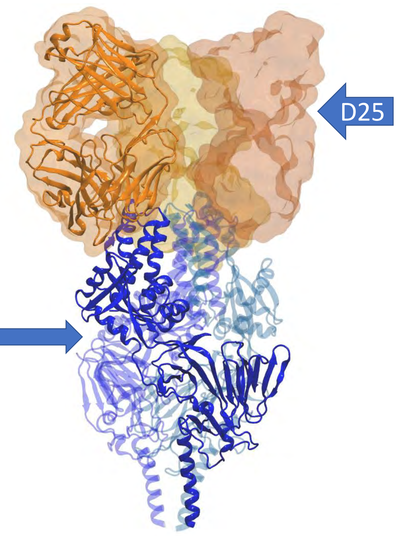

- RSV has a single-stranded, negative sense RNA genome
- It's a significant pathogen among young children, the elderly, and the immunocompromised
- The Fusion (F) protein fuses the viral membrane with the host cell membrane for viral entry into host cells
- F protein is the main target of neutralizing antibodies
- F is also the target for vaccine strategies that are currently in development and the target of monoclonal antibody therapy by Palivizumab

- D25 is a human monoclonal antibody that has potent neutralizing activity against RSV
- D25 is in clinical trials as an RSV therapeutic
- D25 binds to the pre-fusion form of F and inhibits fusion and viral entry
- It is important to understand how RSV can evolve to avoid neutralization by D25

Hypothesis:

- We hypothesize that RSV will mutate under stress of a sub-inhibitory dose of antibodies (D25) resulting in escape from neutralization.
- We also predict that molecular modeling done by our collaborators, Drs. Marty Ytreberg and Jagdish Patel, will be able to accurately predict these mutations.

Methods:

Generating RSV that Expresses a Red Fluorescent Protein

A plasmid with the RSV genome and helper plasmids were transfected into BHK-BSR/T7 cells. The RSV genome plasmid was engineered to incorporate the red fluorescent protein, mKate2, as an indicator of viral replication.

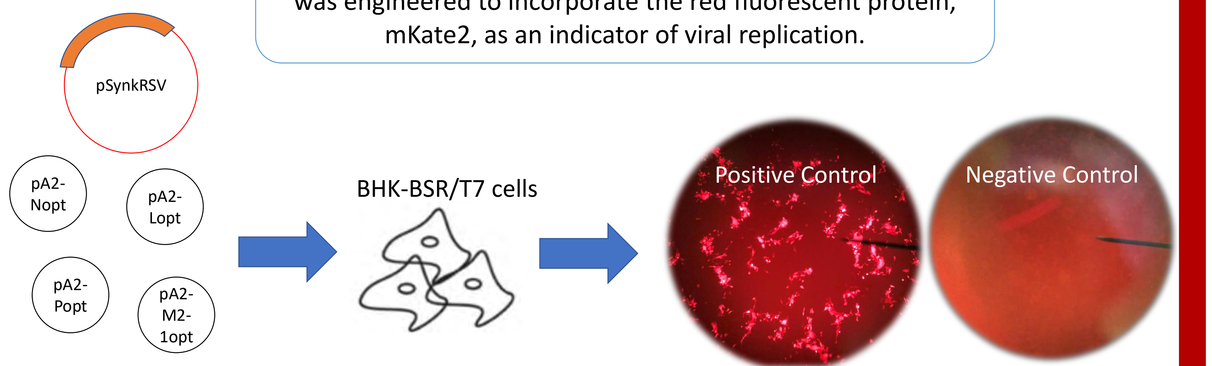

Experimental Evolution of RSV to Select Antibody Escape Mutations

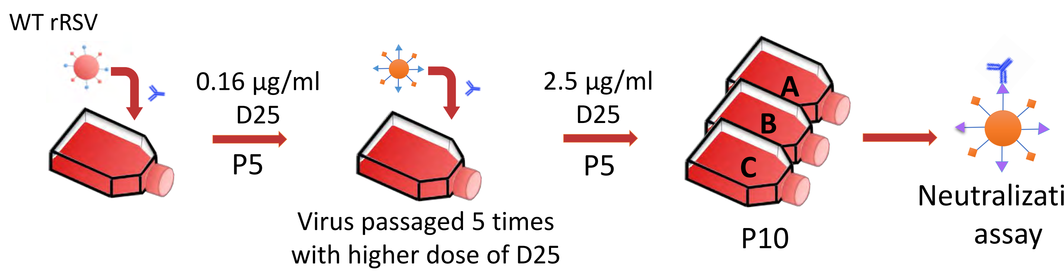

Quantifying RSV by $TCID_{50}$ Assay

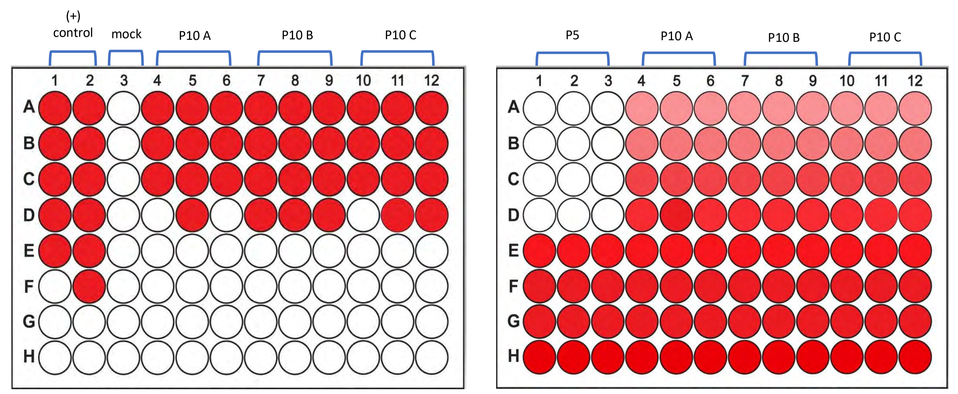

Determining Neutralizing Concentration of Antibody

Isolating Mutant RNA to be Reverse Transcribed to DNA for Sequencing

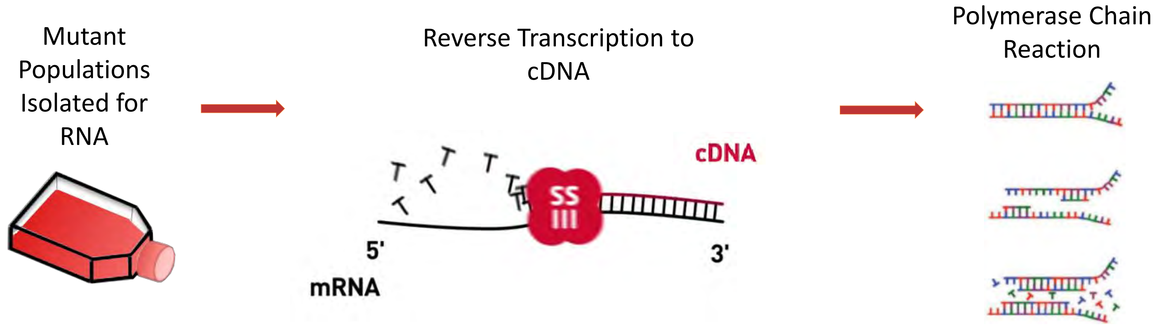

Results:

Passage of Virus in the Presence of Antibodies Results in Increased Resistance to Neutralization

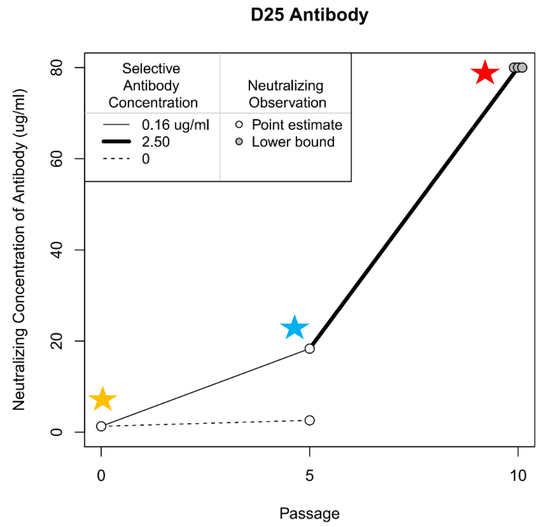

Passaged Viruses Acquired Two Point Mutations Sequentially

★ Wild-type F Amino Acid Sequence	QLLPIVN
★ P5-low [Ab]	QLLPIVY
★ P5-low [Ab]/P5-no [Ab]	QLLPIVY
★ P5-low [Ab]/P5-high [Ab] A	RLLPIVY
★ P5-low [Ab]/P5-high [Ab] B	RLLPIVY
★ P5-low [Ab]/P5-high [Ab] C	RLLPIVY

The Mutations are Predicted to Disrupt the Interaction Between D25 and F

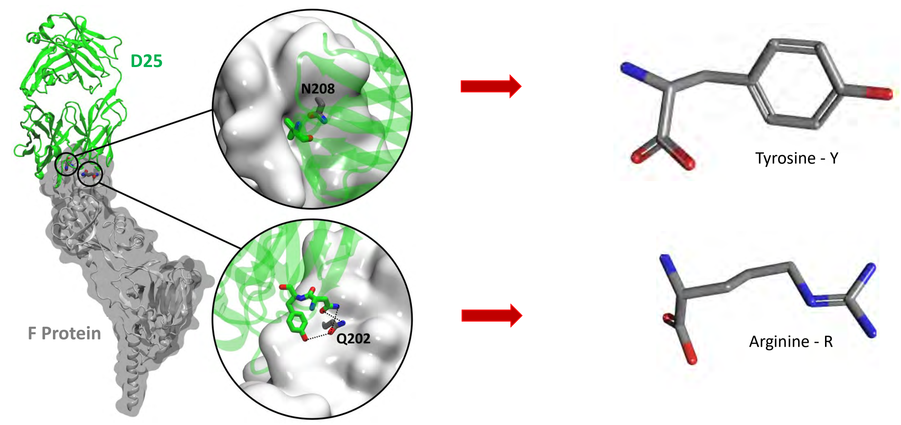

Conclusion and Future Directions:

- After ten rounds of selection in HEp-2 cells, viral mutants required significantly more antibody for neutralization.
- The F protein has mutated that allows it to escape neutralization and the amino acid residues that mutated are predicted to disrupt the interaction between D25 and F.
- Later, we will engineer the predicted D25 mutants into the infectious clone to validate their resistance to D25 and compare their fitness to the wild-type virus.

Acknowledgements and References:

- *Research reported in this poster was supported by the National Science Foundation EPSCoR Research Infrastructure Improvement Program: Track-2, award number OIA-1736253.*
- We gratefully acknowledge Dr. and Mrs. Hill for their support with the Hill Fellowship Grant and the Office of Undergraduate Research for the SURF Fellowship and OUR Grant.
- An additional thank you to Bhim Thapa and Andres Gonzalez for their support and advice as well as Dr. Marty Ytreberg and Dr. Jagdish Patel for the modeling.

- 1. Meng J, Stobart CC, Hotard AL, Moore ML (2014) An Overview of Respiratory Syncytial Virus. PLoS Pathog 10(4): e1004016. doi:10.1371/journal.ppat1004016

Non-Thermal Liquid Plasma Treatment for Removal of Antibiotics in Wastewater

McKenzie Walquist and Dr. Sarah Wu, Department of Biological Engineering

University of Idaho College of Engineering

This project was supported by the University of Idaho through the State Board of Education

Traditional wastewater treatment processes are not able to degrade pharmaceuticals which find their way into the water system. As a result, many bacterial strains have become antibiotic resistant, which is a significant medical concern. One solution currently being explored to prevent these emerging contaminants from being released into the environment is advanced oxidation processes (AOPs), including non-thermal liquid plasma (NTLP) treatment. This process produces high energy mobile electrons and oxidizing radicals which degrade large organic molecules.

Sources and cycles of antibiotics

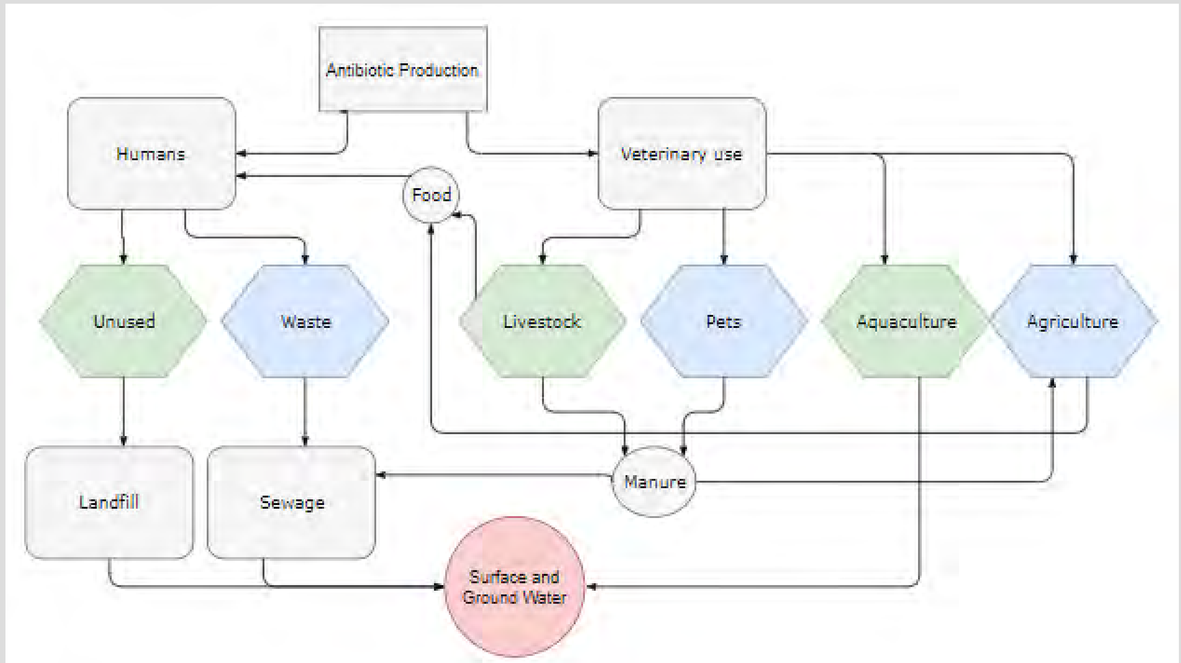

A circulating treatment of tap water to simulate a wastewater stream, was used to remove three types of beta-lactam penicillins (ampicillin, oxacillin sodium salt, and amoxicillin trihydrate).

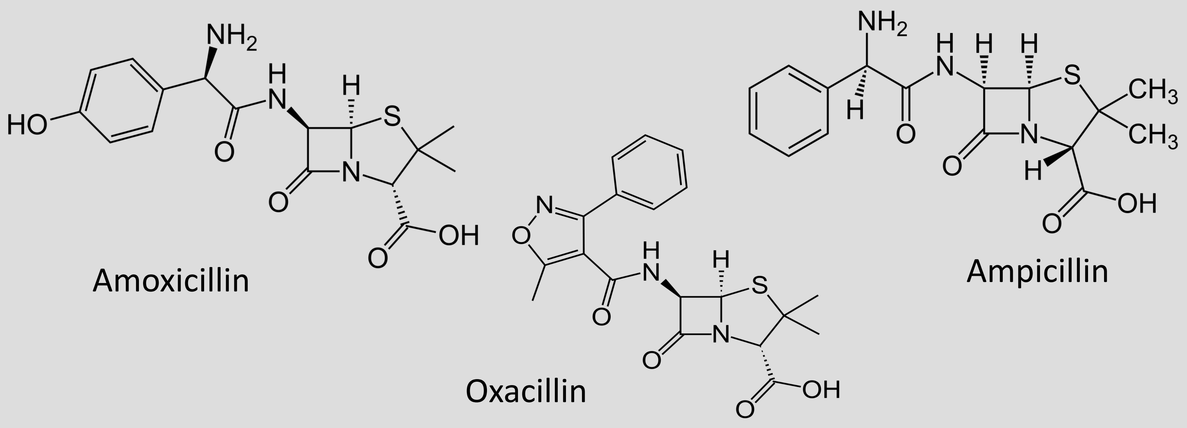

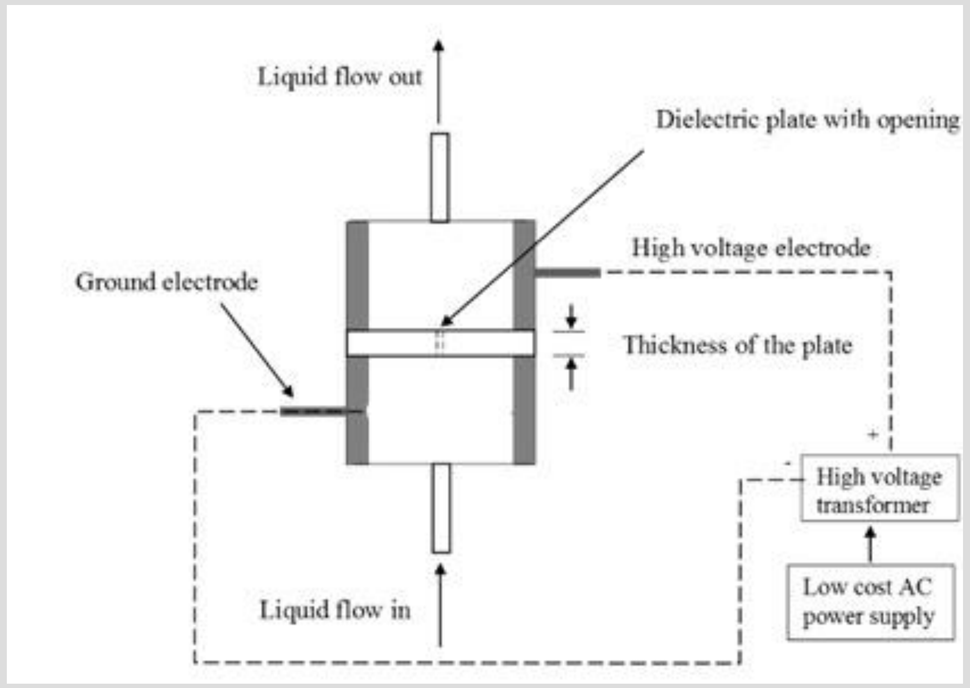

Fig. 1 Circulating non-thermal liquid plasma reactor

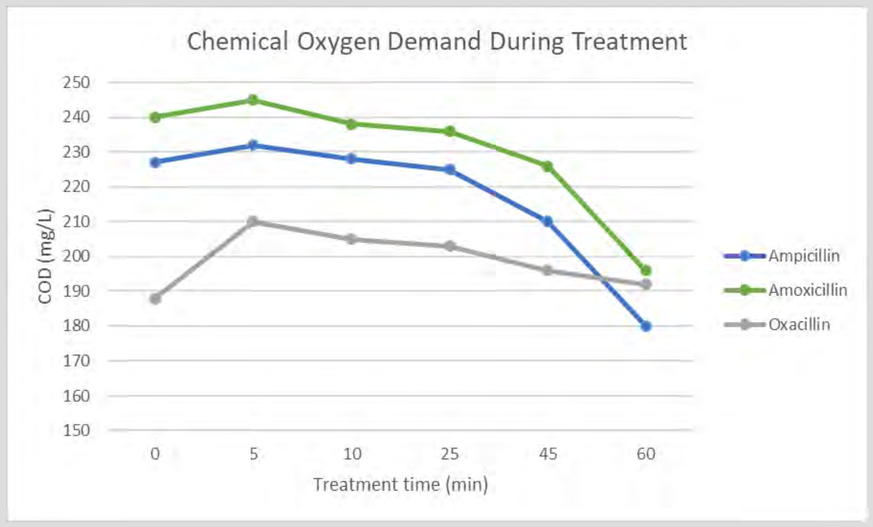

Oxidation

The high voltage between the NTLP reactor electrodes physically breaks the large molecules, and also creates hydrogen peroxide, ozone, and hydroxyl ions. These radicals assist in further oxidizing organic molecules.

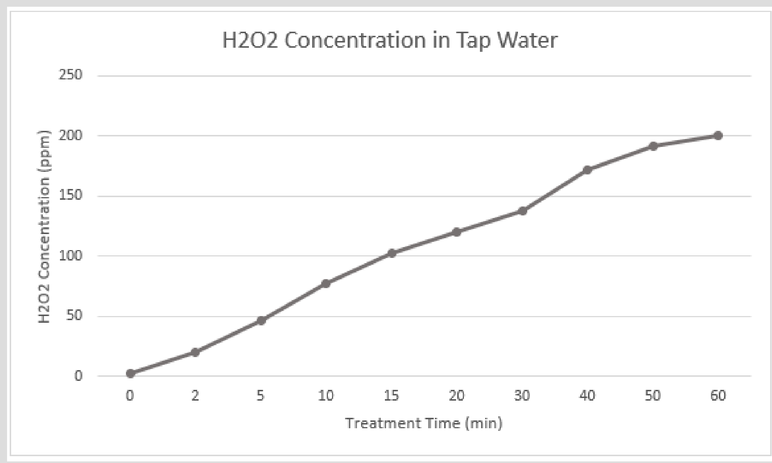

H_2O_2 increases with treatment time. The pH of the solution also increases, suggesting the production of –OH radicals. The decrease in COD suggests the molecules are degraded and oxidized.

Toxicity

In each replicated experiment, using E. coli K12, the bacteria did not grow when plated with either Ampicillin or Amoxicillin. However, when plated with the 1-hour treated solutions, the bacteria were able to grow to the similar colony counts as treated tap water without antibiotics. This suggests the antibiotics were degraded to a point that could no longer affect bacteria at this concentration. This strain of bacteria was not inhibited by the Oxacillin, but the treated solution was shown to also be non toxic.

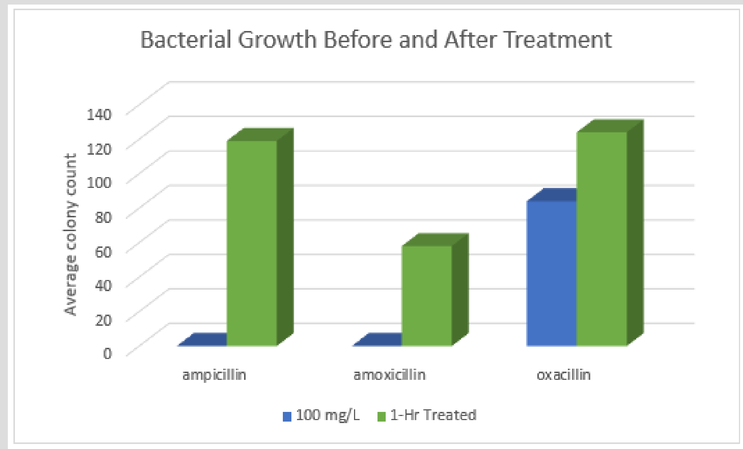

What's Next?

- ❑ LC/MS analysis to identify intermediates and final degradation products
- ❑ Reactor optimization and commercialization